



universität
wien

DISSERTATION / DOCTORAL THESIS

Titel der Dissertation / Title of the Doctoral Thesis

„Seismological contributions on the crustal structure and stress field in
the wider Vienna Basin region from AlpArray“

verfasst von / submitted by

Sven Schippkus, B.Sc., M.Sc.

angestrebter akademischer Grad / in partial fulfilment of the requirements for the degree of

Doktor der Naturwissenschaften (Dr. rer. nat.)

Wien, 2019 / Vienna, 2019

Studienkennzahl lt. Studienblatt /
degree programme code as it appears on
the student record sheet:

A 796 605 416

Studienrichtung lt. Studienblatt /
degree programme as it appears on
the student record sheet:

Geophysik

Betreut von / Supervisor:

Univ.-Prof. Dr. Götz Bokelmann

Acknowledgements

This thesis would not have been possible without the support of my advisor, colleagues, friends, and family. I would like to take this opportunity to express my sincere appreciation and gratitude to them.

My advisor, Professor Götz Bokelmann, provided me with the freedom, support, and trust I needed to grow as an independent researcher, as well as a person. His commitment of time and ideas throughout the years has been invaluable to me and I thank him for that. I further thank the Austrian Science Fund (FWF), the COST action "TIme-DEpendent Seismology" (TIDES), and the Scientific & Technological Cooperation program by OeAD for funding received towards my PhD.

Special thanks to Dimitri Zigone, who has advised and supported me throughout my doctoral studies. He has encouraged me to pursue my own ideas and his constructive and precise criticism has helped my work tremendously.

I would like to thank my colleagues (present and former; local and abroad) for many discussions and collaborations over the years. Some of them I have the pleasure of calling my friends. Thank you Petr, Sofi, Florian, Dimitri, Ehsan, Felix, Gidera, Irene, Eric, Andrew, Katalin, Enrico, Maria-Theresa, Zacharie, Helmut, Herta, and Peter.

My close friends outside of work have kept me grounded throughout these years, continuously reminding me of the more important things in life. Thank you Alice, Constanze, Nils, Anna-Nina, Florian, Ludwig, Simon, Joe, Sarah, André and James.

Finally, I would like to express my appreciation to my family, especially my parents and my brother, for their everlasting support to find my own way. Words cannot express how grateful I am.

Abstract

The Earth's outmost layer, the crust, is the medium in which many of the geological processes that are most impactful on society occur, such as damaging earthquakes or the accumulation of natural resources. In the wider Vienna Basin region, crustal structure and present-day stress field are complex due to its tectonic history and have been subject to several studies. Most published tomographic models of the crustal structure provide only rough insight into the distribution of velocities and are often inconsistent with other observables or have low resolution. Our understanding of the regional stress-field is based on either pointwise measurements or modelling and they do not seem to form a clear and consistent picture of the distribution of stresses in the region.

This thesis uses data of the international AlpArray project to shed additional light on these aspects. The seismic network of AlpArray covers the entire Alps with a dense distribution of broadband seismometers over several years and enables new studies that provide new and detailed insights into the geophysical properties of the Earth. The three topics of this thesis aim to improve our understanding of the crustal structure and present-day orientation of the stress field in the wider Vienna Basin region.

First, seismic tomography based on surface waves, which are retrieved from cross correlations of the ambient seismic field, provides a new and detailed image of the shear-velocity structure of the crust. It reveals a deep-seated low-velocity anomaly underneath the Northeastern Vienna Basin, provides new constraints on the deeper crustal structure of the Vienna Basin, and sheds light on the geometry of the European-Adriatic plate interface in the region. It matches well with other observables, such as crystalline basement depths from boreholes, surface geology, and gravity anomaly.

Second, the Alland earthquake sequence of 2016-2017 occurred in the study region in an area that has been seismically quiet over historical times. It occurred \sim 30km North of the main active fault systems in the region and near the location of the damaging $M \sim 6$ Neulengbach/Ried am Riederberg earthquake of 1590. The sequence ruptured a NE-dipping fault in the crystalline basement of the Bohemian massif underneath the Eastern Alps. In this region of moderate seismicity, the $M_L = 4.2$ main shock is a significant event and its thrust-faulting source mechanism suggests a \sim NE/SW-orientation of maximum horizontal compressive stress σ_H .

Third, to provide an independent and spatially broad measurement of the present-day stress-field orientation, the azimuthal anisotropy of Rayleigh waves is studied as a proxy. Azimuthal anisotropy in the shallow crust provides insight into the stress-field-orientation due to the sensitivity of seismic waves to fluid-filled cracks. In the West, and North of the Mur-Mürz-Line, \sim N/S-orientations of σ_H are observed that rotate towards \sim NE/SW-orientations in the East. These stress-field orientations are consistent with the source mechanism of the Alland sequence and the observed seismic activity in the region in general. In the deeper crust, azimuthal anisotropy may be caused by the alignment of crystals due to crustal deformation and the measured orientations are consistent with the lateral extrusion of blocks of the Eastern Alps.

This thesis provides a detailed image of the crust, the source properties of the Alland earthquake sequence, and a new and independent measurement of the stress-field orientation in the wider Vienna Basin region. These results help to better understand the structure and tectonic processes in region.

Zusammenfassung

Die äußerste Schicht der Erde, die Kruste, ist das Medium in dem viele der für den Menschen bedeutsamsten geologischen Prozesse stattfinden, z.B. aktive Deformation, die Erdbeben auslösen kann, und auch die Anhäufung natürlicher Ressourcen. Im Wiener Becken und seiner Umgebung sind die Struktur der Kruste und das Spannungsfeld aufgrund der vielfältigen tektonischen Geschichte komplex. Die meisten veröffentlichten tomographischen Modelle gewähren lediglich grobe Einblicke in die Verteilung von Geschwindigkeiten der Kruste und sind häufig inkonsistent mit anderen Beobachtungen oder haben geringe Auflösung. Das derzeitige Wissen über das regionale Spannungsfeld basiert auf punktweisen Messungen oder Modellierungen, und sie formen kein klares und konsistentes Bild.

Diese Arbeit verwendet Daten des internationalen AlpArray-Projekts, um diese Aspekte genauer zu beleuchten. Im Rahmen von AlpArray wurde der gesamte Alpenraum über mehrere Jahre mit einem dichten Netzwerk von Breitbandseismometern abgedeckt. Dies ermöglicht neue Studien sowie detaillierte Einblicke in die geophysikalischen Eigenschaften der Erde. Die drei Themen dieser Arbeit zielen darauf ab, unser Verständnis über die Struktur der Kruste und die Orientierung des heutigen Spannungsfeldes in der Gegend des Wiener Becken zu erweitern.

Im ersten Teil wird ein neues und detailliertes Abbild der Schergeschwindigkeiten in der Kruste vorgestellt, das mit Hilfe seismischer Tomographie von Oberflächenwellen, die auf Kreuzkorrelationen des Umgebungsrauschens basieren, hergeleitet wurde. Dieses Modell zeigt eine tief-sitzende Niedrig-geschwindigkeitsanomalie unter dem nordöstlichen Wiener Becken; es gewährt neue Einblicke in die tiefere Struktur der Kruste und wirft Licht auf die Geometrie des Übergangs zwischen Europäischer und Adriatischer Platte. Das Modell stimmt mit anderen Beobachtungen, wie etwa der Tiefe des Kristallin aus Bohrlöchern, der Verteilung von Gesteinen an der Oberfläche, und Schwereanomalien überein.

Als zweiter Teil folgt eine Untersuchung der Erdbebenserie von Alland, die in einer zuvor seismisch ruhigen Gegend stattgefunden hat. Sie liegt ~30km nördlich der aktiven Störungszonen der Region und damit nahe des $M \sim 6$ Erdbebens von Neulengbach/Ried am Riederberg aus dem Jahr 1590. Die Serie fand auf einer nach Nordosten einfallenden Störung im Kristallin der Böhmisches Masse, unterhalb der Ostalpen, statt. In dieser Region moderater Seismizität ist das Hauptbeben mit $M_L = 4.2$ ein bedeutsames, und sein Aufschreibungsmechanismus deutet auf eine ~NE/SW-Orientierung der maximalen horizontalen Kompressionsspannung σ_H hin.

Im dritten Teil wird die azimuthale Anisotropie von Rayleigh-Wellen untersucht, um die Orientierung des Spannungsfeldes räumlich umfassend und unabhängig zu messen. Azimuthale Anisotropie in der Oberkruste gewährt Einblick in die Spannungsfeldorientierung, da sie stark von der Orientierung fluid-gefüllter Risse in der Kruste abhängt, und daher als Proxy für das Spannungsfeld dienen kann. Westlich und nördlich der Mur-Mürz-Linie werden ~N/S-Orientierungen von σ_H beobachtet, die gen Osten in ~NE/SW-Orientierungen rotieren. Diese Orientierungen des Spannungsfeldes sind konsistent mit dem Herdmechanismus des Alland-Bebens sowie der seismischen Aktivität in der Region im Allgemeinen. In der Unterkruste ist die beobachtete azimuthale Anisotropie vermutlich durch die Einreihung von Kristallen im Laufe krustaler Deformation bedingt, entsprechend der lateralen Extrusion von Blöcken der Ostalpen.

Diese Arbeit präsentiert ein neues Abbild der Kruste, die Herdeigenschaften der Alland-Erdbeben-serie und eine neue und unabhängige Messung der Orientierung des Spannungsfelds in der Gegend des Wiener Beckens. Diese Ergebnisse helfen ein besseres Verständnis der Struktur und der tektonischen Prozesse der Region zu gewinnen.

Contents

Abstract	vi
Zusammenfassung	viii
Contents	x
List of Figures	xiii
List of Tables	xiv
1 Introduction	1
1.1 Tectonics and Geology of the wider Vienna Basin region	1
1.2 Previous geophysical studies	5
1.2.1 Seismicity	5
1.2.2 Velocity models	7
1.2.3 Seismic and interpreted profiles	10
1.2.4 Gravimetry	11
1.2.5 Stress Field	12
1.3 Seismological station and data coverage	16
1.3.1 Permanent national networks	16
1.3.2 Previous temporary seismological installations	16
1.3.3 AlpArray	18
1.4 Scientific questions and thesis outline	20
2 Ambient-noise tomography of the wider Vienna Basin region	23
2.1 Introduction	23
2.2 Data	26
2.3 Ambient-noise cross-correlations	27
2.3.1 Pre-processing	27
2.3.2 Green's Function retrieval	28
2.4 Rayleigh-wave group velocities	31
2.5 Group-velocity inversion	33
2.5.1 Determination of regularization parameters	34
2.5.2 Group-velocity resolution analysis	35
2.5.3 Group-velocity maps	37
2.6 Shear-velocity inversion	38
2.6.1 Shear-velocity depth resolution	39

2.6.2	3D shear-velocity model	40
2.6.2.1	Shear-velocity maps	40
2.6.2.2	Shear-velocity profiles	43
2.7	Discussion	45
2.7.1	Vienna Basin	45
2.7.2	Little Hungarian Plain and Bohemian Massif	48
2.8	Conclusions	50
3	The Alland earthquake sequence in Eastern Austria	53
3.1	Introduction	53
3.2	Data	56
3.3	Earthquake Series Characterization	56
3.3.1	Locations	57
3.3.2	Source Mechanism	61
3.4	Discussion	66
3.5	Conclusions	72
4	Azimuthal anisotropy as a proxy for the stress-field	75
4.1	Introduction	75
4.2	Data and Method	79
4.3	Results	80
4.3.1	Measured Group Velocities	80
4.3.2	Modelled Group Velocities	81
4.3.3	Group Velocity Residuals	83
4.3.4	Impact of smoothing constraint	83
4.4	Discussion	85
4.4.1	Methodology	85
4.4.2	Geological and Tectonic Context	87
4.5	Conclusions	92
5	Summary and Conclusions	97
5.1	Crustal structure	97
5.2	Stress field	98
Appendices		100
A	Appendix to Section 2	100
A.1	Determination of Pre-Processing Parameters	100
A.2	Inter-station group velocities	101

A.3	Regularization parameters λ and β	101
A.4	Group-velocity misfit	101
A.5	Figures	103
B	Appendix to Section 3	106
B.1	Estimation of Waveform Misfit	106
B.2	Moment Tensor Inversion Iterations	107
B.3	Figures	108
C	Appendix to Section 4	113
C.1	Figures	113
	References	117

List of Figures

1.1	Topographic map of the wider Vienna Basin region	2
1.2	Geological map of the wider Vienna Basin region	3
1.3	Map of the crystalline basement of the European plate	4
1.4	Historical seismicity in the wider Vienna Basin region	6
1.5	Comparison of recent regional shear-velocity models	8
1.6	Seismic profile CEL09 crossing the Vienna Basin	10
1.7	Seismic profile 7R crossing the Vienna Basin	11
1.8	Map of Bouguer gravity anomaly in the wider Vienna Basin region	13
1.9	Map of present-day stress-field in the wider Vienna Basin region from Reinecker & Lenhardt (1999)	14
1.10	Map of present-day stress-field in the wider Vienna Basin region from Bada et al. (2007)	15
1.11	Map of seismic stations in the wider Vienna Basin region	17
1.12	Map of AlpArray	19
2.1	Topographic map of the study region	24
2.2	Example correlograms for two station pairs	29
2.3	Full cross-correlation tensor	30
2.4	Histogram of measured group velocities	32
2.5	Regularization parameters σ and α	35
2.6	Path density maps	36
2.7	Resolution length maps	36
2.8	Group-velocity maps	37
2.9	Shear-velocity inversion initial models and results	39
2.10	Resolution matrix	40
2.11	Shear-velocity maps	42
2.12	Shear-velocity profiles	44
2.13	Surface geology and Bouguer gravity anomaly	46
3.1	Map of historical seismicity in the study region	55
3.2	Time-history and Gutenberg-Richter plot of the Alland sequence	57
3.3	Comparison of locations (AEC, NonLinLoc, HypoDD)	58
3.4	Relative locations and their geometry	60
3.5	Depth- and frequency-dependence of moment tensor	62

3.6	Double-couple solution space	63
3.7	Waveform fit with synthetics	64
3.8	Waveforms of six largest events	65
3.9	Fault plane solutions of ZAMG, SLU, this study	67
3.10	Alland earthquake near the edge of the Bohemian Spur	68
3.11	Classification of shear-velocity profile at Alland	69
3.12	Seismic profile C 8503 near Alland	70
4.1	Tectonic sketch map of study region	76
4.2	Inter-station geometry	78
4.3	Directional dependence of 2Θ -terms	81
4.4	Regionalized fast orientations	82
4.5	Impact of smoothing constraint	84
4.6	Interpretation of regionalized fast orientations	88
4.7	Rayleigh wave sensitivity kernel	90
4.8	Stress- vs. texture-related anisotropy	91
4.9	Schematic Mohr's circle	91
A.1	Pre-processing parameters	103
A.2	Inter-station group velocities	104
A.3	Regularization parameters λ and β	105
A.4	Group-velocity misfit	105
B.1	Waveforms of Alland mainshock	108
B.2	Histogram of Cross-correlation coefficients between waveforms of the sequence	109
C.1	Measurement of anisotropic terms	113
C.2	Directional dependence of 4Θ -terms	114
C.3	Numerical simulations of 2Θ -parameter-retrieval	115
C.4	Regionalized azimuthal anisotropy (5s-20s)	116

List of Tables

B.1	Locations of the Alland earthquake series	110
-----	---	-----

1 Introduction

The wider Vienna Basin region (WVBR) is located in the Alpine-Carpathian-Pannonian junction at the eastern edge of the Alps (Fig. 1.1), a region characterized by geological and tectonic complexity. Several major geological and tectonic features are located in close proximity of a few hundred kilometers (see Figs. 1.1, 1.2). These include the pull-apart Vienna Basin, other foreland (Molasse) and back-arc basins (Pannonian Basin), the Eastern Alps, the Bohemian Massif, and the Western Carpathians, as well as major fault systems such as the Alpine Thrust Front (AF), the sinistral strike-slip Mur-Mürz-Line (MML) and Salzach-Ennstal-Mariazell-Puchberg (SEMP) faults, and the strike-slip and normal-faulting Vienna Basin Transfer Fault System (VBTFS). Due to its unique tectonic position and economical importance — the Vienna Basin is the largest petroleum basin in Austria — the WVBR has been studied extensively in the past, especially through seismological methods (e.g., Hrubcová et al., 2005; Behm et al., 2007; Ren et al., 2013; Brückl et al., 2014; Behm et al., 2016). In recent years, new opportunities have arisen through the ever-increasing availability of seismic data, particularly proliferated by international efforts (e.g., Brückl et al., 2003; Dando, 2011; Hetényi et al., 2018a), to answer open questions and improve our understanding of the region.

This thesis takes advantage of these new opportunities with the aim to improve our understanding of the geological and tectonic setting of the WVBR, focusing on crustal structure, recent seismicity, and the present-day stress field. This introduction will give an overview of the tectonics and geology (Section 1.1), previously conducted geophysical studies that form our current understanding (Section 1.2), and the available seismological data in the region (Section 1.3). These sections will give rise to many open scientific questions, some of which this thesis aims to address (Section 1.4).

1.1 Tectonics and Geology of the wider Vienna Basin region

The present-day geological structure of the WVBR is the result of a complex history of tectonic deformation that can be roughly divided into three main parts: The orogeny of the Alps, followed by eastwards lateral extrusion of crustal blocks, and the consequential formation of the Vienna Basin.

The Alps are a mountain chain that is a small part of the Gibraltar-Himalayan orogenic belt. The convergence of Africa and Eurasia led to the closing of the Penninic ocean through subduction and subsequent collision in late Cretaceous (Suess, 1901; Schmid et al., 2004; Pfiffner, 2014). The polarity of subduction is southwards, i.e., the European plate subducts underneath the Adriatic plate. However, some authors have reported a more complex subduction geometry, especially

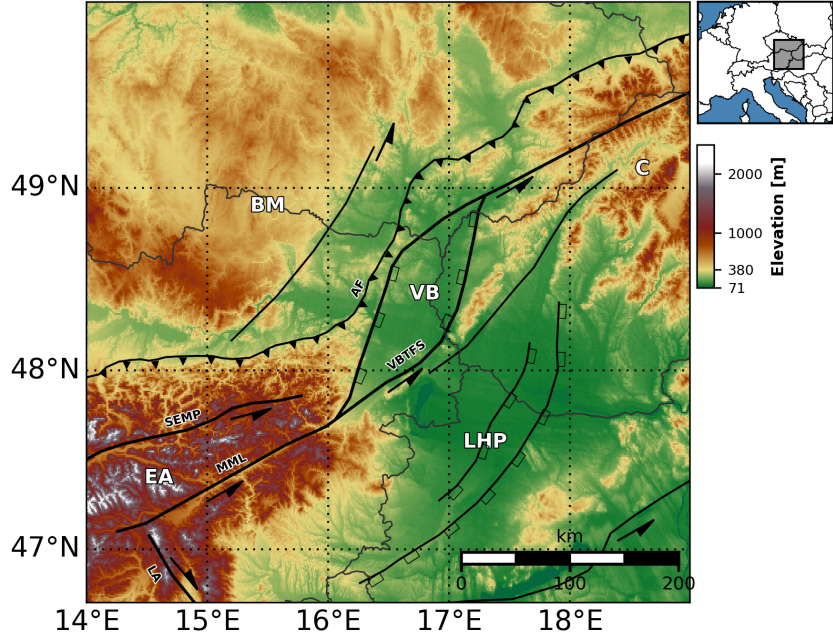


Figure 1.1: Topographic map of the wider Vienna Basin region depicting the major tectonic and geomorphological features. Labelled faults: Alpine Front (AF), Salzach-Ennstal-Mariazell-Puchberg fault (SEMP), Mur-Mürz-Line (MML), Vienna Basin Transfer Fault System (VBTFs), Lavanttal fault (LA). Labelled regions: Eastern Alps (EA), Bohemian Massif (BM), Vienna Basin (VB), Little Hungarian Plain (LHP), Carpathians (C). Faults redrawn after Peresson & Decker (1997).

in the Eastern Alps, where models such as slab detachment (Mitterbauer et al., 2011; Qorbani, 2015) and reversal of subduction-polarity (Lippitsch et al., 2003) have been proposed. The two major plates involved in these processes — the European and Adriatic plates — make up the geological structure of the crust in the WVBR as we see it today (Figs. 1.2, 1.3).

North of the Alpine Thrust Front (AF in Fig. 1.1), the subduction interface between the two plates, the European plate is exposed at the surface. Most prominently, one finds magmatic and metamorphic rocks of the Precambrian and Permian in the Bohemian massif (Fig. 1.2), an old geological structure that was also involved in the Variscan orogeny (e.g., Wessely, 2006). In the wider Vienna Basin region, the crystalline basement of the European plate subducting below the Adriatic plate is separated into two major parts: The magmatic and metamorphic basement of the Bohemian massif to the West, and further to the East — below the Vienna Basin — the Austroalpine basement, consisting of sedimentary rocks from the Paleozoic (see Fig. 1.3). To the South, sedimentary rocks of the Mesozoic are present. The extent of the basement of the

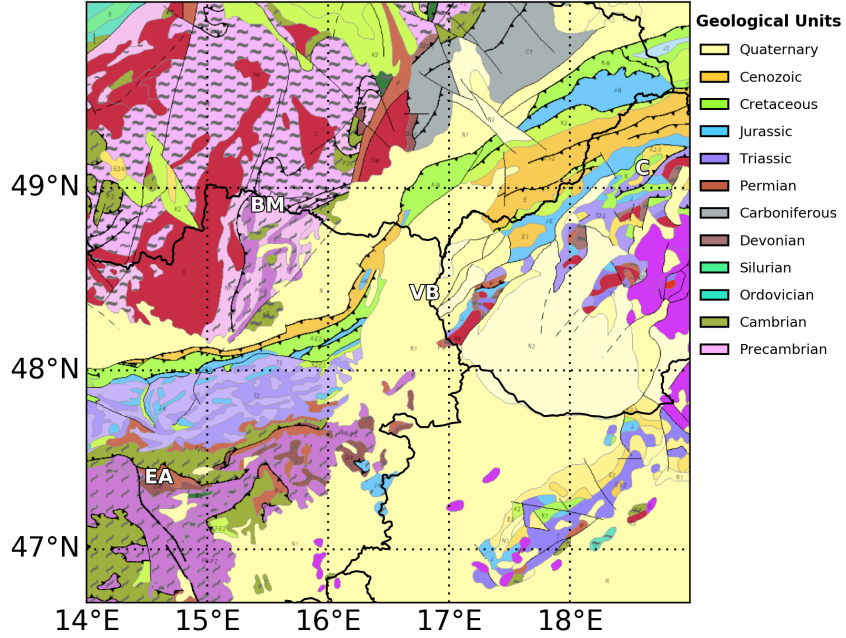


Figure 1.2: Geological map of the wider Vienna Basin region, extracted from the 1:5 Million International Geological Map of Europe and Adjacent Areas (IGME5000, Aschk, 2005). It showcases the complex distribution of rocks from several geological periods. To the North of the Alpine Front, the European plate is exposed at the surface. The Eastern Alps and Carpathians, which are overthrust sheets of the Adriatic plate, are found to the South of the Alpine Front.

Bohemian massif towards South is sometimes referred to as the so-called "Bohemian Spur" (BS) (e.g., Malzer et al., 1993; Wessely, 2006), and there are indications that it may have played an important role in geomorphology and the distribution of tectonic stresses in the region (Malzer et al., 1993; Reinecker & Lenhardt, 1999; Wessely, 2000). It appears that the shape of the Alpine-Carpathian arc is controlled by the Bohemian Spur with a turn of the strike of the arc near the Southeastern edge of the BS from W/E-striking (in the West) to NE/SW-striking (in the East) (Fig. 1.2, Brix & Schultz, 1993; Wessely, 2000, 2006). Just North of the Alpine Front, the European plate and Bohemian Spur are covered by Quaternary sediments of the Molasse basin, a classical foreland basin (Fig. 1.2).

To the South of the AF and ontop of the European Plate lies the Adriatic plate. It is mostly comprised of sedimentary rocks, arranged as overthrust SW-dipping nappes due to the Alpine N/S-convergence (Pfiffner, 2014). The nappes are the defining geological structures in the Eastern Alps, Western Carpathians, as well as the rocks below the Quaternary fill of the sedimentary basins

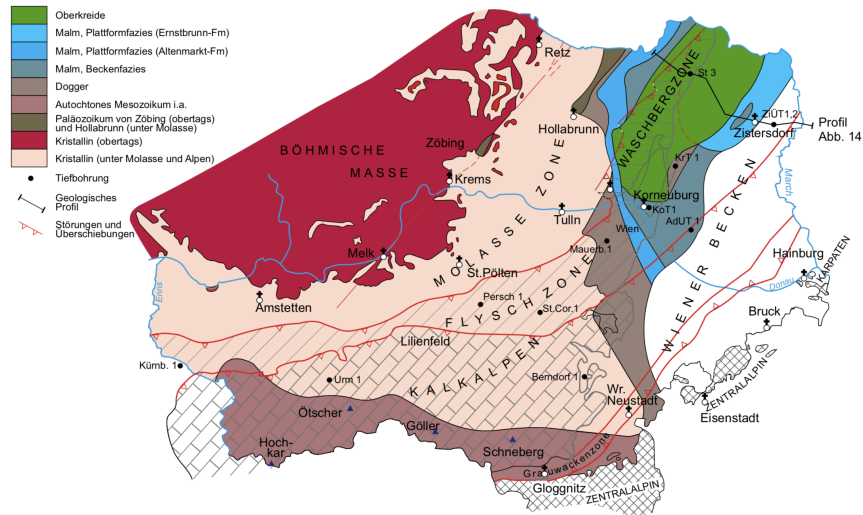


Figure 1.3: Map of the crystalline basement of the European plate in lower Austria, from Wessely (2006). The extent of the magmatic and metamorphic rocks of the "Bohemian Spur" (red and beige colors) underneath the overthrust nappes of the Adriatic plate is shown. Sedimentary rocks of the Austroalpine basement are found to the East of it. To the South, sedimentary rocks of the Mesozoic are present.

(Fig. 1.2, Wessely, 2006). Some smaller mountain ranges, e.g., the Leitha mountains and Little Carpathians, however, are excavated Penninic units, indicating the complex tectonic interaction at the Alpine-Carpathian-Pannonian junction (Pfiffner, 2014).

Starting in late Oligocene and early Miocene, after collision in the Eastern Alps came to a halt, crustal blocks of the Eastern Alps — referred to as the Alpine-Carpathian-Pannonian (AL-CAPA) and Tisza blocks — began extruding laterally towards East (Gute deutsch & Aric, 1988; Ratschbacher et al., 1991a; Wölfle et al., 2011). The forces controlling this movement were a combination of potential energy of the lifted Alps and lateral escape due to continued East- and Northwards movement of the Carpathian front (Ratschbacher et al., 1991a). The major strike-slip fault systems in the region formed to accommodate this extrusion. These include the sinistral MML, SEMP, and VBTFS that mark the Northern edge of extrusion, as well as the dextral Periadriatic Line, and Lavanttal Fault (LA), that mark the Southwestern edge (see Fig. 1.1). The continued movement of the Carpathians led to the formation of several back-arc basins in the Pannonian basin system, e.g., the Little Hungarian Plain (LHP, sometimes called "Danube Basin") within the study region (Fig. 1.1, Wessely, 2006; Berka, 2015).

Finally, the Vienna Basin formed as a pull-apart basin on top of thrust sheets due to the lateral extrusion of blocks (Royden, 1985; Wessely, 2006; Hözel et al., 2010; Berka, 2015). The VBTFS

encompasses the extent of the Vienna Basin, with normal-faulting sides at the Eastern and Western ends, and sinistral strike-slip faulting at the Southern and Northern edge of the basin (see Figs. 1.1, 1.2). It is an economically and socially important basin for the region as the largest oil & gas reservoir in Austria and housing a population of \sim 2 million people.

1.2 Previous geophysical studies

1.2.1 Seismicity

Earthquakes are the prime natural phenomenon that allows insight into the interior of the Earth. Seismic waves, such as those emitted by earthquakes, are generally utilized to study two different aspects of the Earth: the physical properties of the source, e.g., earthquake strength and rupture geometry, or the medium the waves travel through, i.e., the structure of the Earth. Both of these approaches have provided tremendous insight and largely shape our understanding of the structure and dynamics of the Earth. This includes e.g., the existence of the Earth's layers or the geometry and dynamics of major fault systems (e.g., Stein & Wysession, 2003; Shearer, 2009, and references therein). The geometry of active fault systems is often illuminated by the distribution of earthquake hypocenters aligned along those faults, giving a detailed view into the Earth, unrivalled by other methods (Stein & Wysession, 2003).

In the WVBR, some of the major fault systems show moderate seismic activity, namely the MML and Southern VBTFS (Fig. 1.4). The MML directly transitions northwards into the VBTFS. Defining a clear border between the two seems inappropriate. This fault system is one of the most active fault systems in Austria and has repeatedly exhibited earthquakes of local magnitude $M_L > 4$ according to the Austrian Earthquake Catalogue (AEC, 2016). The $M_L = 4.2$ and $M_L = 4.3$ Ebreichsdorf earthquakes of 2013 have shown sinistral strike-slip faulting, matching well with the fault geometry of previous events in the area, e.g., the $M_L = 4.8$ earthquake in 2000 (see Fig. 1.4, Apoloner et al., 2015). Other faulting types are also well documented along this fault system, e.g., the $M_L = 3.6$ Seebenstein of 2013 (AEC, 2016) with a thrust-faulting mechanism, and the $M_W = 4.2$ event of 2009 near Semmering with oblique normal-faulting (see Fig. 1.4, Lentas et al., 2019). Brückl et al. (2014) further confirm that all faulting types are represented along the MML.

There is geological and paleoseismological evidence for earlier seismic activity on the normal faults of the VBTFS. Hintersberger et al. (2018) suggest that several earthquakes of magnitude ~ 6.5 have occurred within the Vienna Basin on the Markgrafneusiedl fault, based on offset geological units observed at three trenches across the fault. They report a recurrence interval of $\sim 20\text{-}25$ thousand years. Archaeological excavations in Carnuntum, 25km East of Vienna, have revealed structurally damaged buildings that Decker et al. (2006) interpret to be caused by one

major earthquake of magnitude ~ 6 in 350 A.D. along the Lassee segment of the VBTFS. The Lassee segment, located near the Austrian-Slovakian border, shows a lack of seismic activity in the catalogue (see Fig. 1.4 Decker et al., 2006).

There is a high-density cluster of seismic events at the Northeastern corner of the study region (Fig. 1.4), but these are man-made explosions related to mining activity (e.g., Zedník & Pazdírková, 2010) and thus not relevant for tectonic considerations.

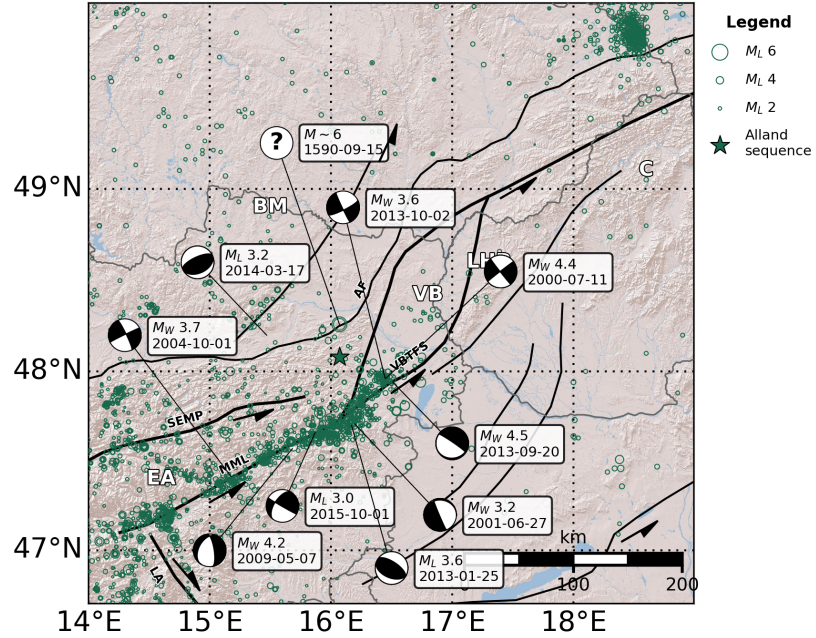


Figure 1.4: Historical seismicity from 1200 to 2018 in the wider Vienna Basin region, compiled from the Austrian Earthquake Catalogue (AEC, 2016) and the catalogue of the European-Mediterranean Seismological Centre (Godey et al., 2006). A selection of source mechanisms is shown, compiled from the ISC Bulletin (Lentas et al., 2019, given in moment magnitude M_w) and from the Central Institute for Meteorology and Geodynamics in Vienna (ZAMG, C. Freudenthaler, pers. comm., given in local magnitude M_L). Seismic activity along the MML and VBTFS shows a combination of strike-slip-, normal- and thrust-faulting. To the North of these faults, low activity is observed except for the seismic events associated with mining blasts in the Northeastern corner of the study region (Zedník & Pazdírková, 2010). The $M \sim 6$ earthquake of 1590 occurred near the surface trace of the AF, but not much is known about this event (Hammerl & Lenhardt, 2013). The Alland earthquake sequence of 2016-2017 occurred in a previously seismically quiet area (marked as \star) near the event of 1590. Labels of geographical regions and faults follow Figure 1.1

The AF and to some degree the SEMP, on the other hand, appear to be seismically largely

inactive in the study region today. Still, the Neulengbach/Ried am Riederberg earthquake of 1590 with a macroseismic magnitude of ~ 6 occurred close to the surface expression of the AF (see Fig. 1.4, Hammerl & Lenhardt, 2013; Hammerl, 2017). It caused considerable damage to surrounding villages and cities, including Vienna. Several properties of this earthquake remain unclear, e.g., its source mechanism. Recently, this previously seismically quiet area North of the MML (near the 1590 event) has seen increased seismic activity with the 2016-2017 Alland earthquake sequence with a $M_L = 4.2$ main shock (Fig. 1.4, Section 3) and the $M_L = 3.1$ 2019 Tulln earthquake (April 2019 ZAMG Seismicity Report, 2019). Questions remain about the potential for severely damaging earthquakes in the WVBR in the future.

1.2.2 Velocity models

Seismic waves that propagate through the Earth allow to image its velocity structure. In classical applications, seismic waves emitted by earthquakes are utilized for tomography. They are often used to image the deeper structure of the Earth using teleseismic events (e.g., Lippitsch et al., 2003; Mitterbauer et al., 2011; Hua et al., 2017; Sun et al., 2019), or to study the crustal structure using local earthquakes (e.g., Kissling, 1988; Paul et al., 2001; Diehl et al., 2009; Wagner et al., 2012). The increased availability of continuous broadband seismic records and methodological development has recently allowed the use of "ambient seismic noise" (Aki, 1957; Campillo & Paul, 2003; Roux et al., 2005; Nakata et al., 2019), which has revolutionized seismologist's capabilities to image the crustal structure of the Earth (e.g., Shapiro et al., 2005; Yang et al., 2007; Stehly et al., 2009; Verbeke et al., 2012; Ren et al., 2013; Molinari et al., 2015; Lu et al., 2018). Surface-wave-based velocity models, such as the ones based on ambient noise, allow vertically granular insight into the structure of Earth, because the depth-sensitivity of surface waves depends on their period (e.g., Shearer, 2009). Several velocity models have been published that aim to describe the crustal structure in the WVBR.

Yang et al. (2007) present the first seismic tomography of Europe that is based on ambient noise with a resolution of $\sim 75\text{km}$ in the WVBR. They use data recorded at 125 broadband stations over 12 months to compute Rayleigh-wave group-velocity maps. At 16s period (sensitive to mid-crustal depths), their model shows a low-velocity anomaly at the border triangle of Austria, Czech Republic, and Slovakia.

The crustal model EuCRUST-07 (Tesauro et al., 2008) is a compilation of the results of previous studies, which are based on the analysis of reflection and refraction profiles, as well as receiver functions across Europe. The model represents the crust as a three-layer model (sediments, upper crust, lower crust). In the upper crust, the model shows no strong velocity contrasts in the WVBR.

Stehly et al. (2009) use data from 150 broadband stations distributed across Europe to compute

an updated velocity model of Europe with a reported lateral resolution of \sim 50km in the WVBR. They find a low-velocity anomaly at mid-crustal depths at the Slovakian-Hungarian border that does not appear to reach far into Austria.

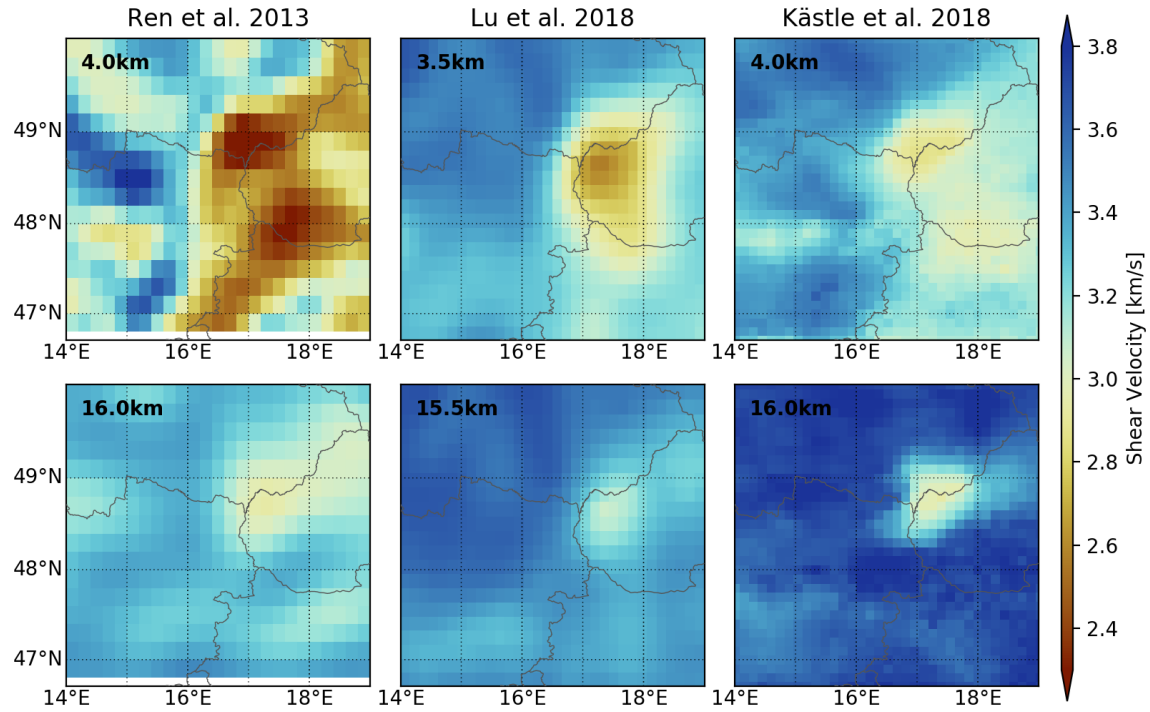


Figure 1.5: Comparison of recent regional shear-velocity models by Ren et al. (2013), Lu et al. (2018), and Kästle et al. (2018) at shallow crustal (4km, top row) and mid-crustal depths (16km, bottom row). They exhibit only rudimentary agreement about the magnitude and extent of low-velocity anomalies in the region. Especially at shallow crustal depths (4km) strong differences between the models are apparent.

The crustal model of the European plate EPcrust (Molinari & Morelli, 2011) is another compilation of previous literature, and gives broad regional insight into the crustal structure. It represents the crust as three layers, similar to Tesauro et al. (2008). The model shows no significant velocity variations in the WVBR, although the authors claim to achieve a lateral resolution of 0.5° by 0.5° .

Ren et al. (2013) use data of the Carpathian Basin Project (CBP, Dando, 2011), a temporary network with 56 broadband stations, in addition to permanent seismic stations to compute a shear-velocity model of the Pannonian region, based on ambient noise (Fig. 1.5). They report to "adequately resolve structures as small as 60km" (Ren et al., 2013) and find significant low-velocity anomalies in the WVBR (see Fig. 1.5) that are correlated with the location of sedimentary basins in the region (Vienna Basin, Little Hungarian Plain).

Kästle et al. (2018) combine surface waves from both ambient noise and earthquake records to provide a velocity model with an estimated lateral resolution of \sim 25km, improving upon previously published models and providing a more detailed view of the crust in Europe (see Fig. 1.5).

Similarly, Lu et al. (2018) provide an image of the crust and mantle using early data of the AlpArray project (Hetényi et al., 2018a) and permanent national networks, in total of 1,293 broadband seismic stations. They claim to achieve lateral resolution of down to 0.3° (see Fig. 1.5).

Velocity models that are more focused on the WVBR include the studies by Behm et al. (2007), Brückl et al. (2010), and Behm et al. (2016). Behm et al. (2007) present a crustal 3D P-wave velocity model based on wide-angle reflection and refraction data. Brückl et al. (2010) studied depths of the Mohorovičić discontinuity ("Moho"), the crust-mantle interface, using controlled source seismic experiments and elastic plate modeling. They report Moho depths of \sim 30-40km in the WVBR. Both of these studies are limited by relying on measurements along only a few profiles (Behm et al., 2007; Brückl et al., 2010). Behm et al. (2016) computed a 3D shear-velocity model based on ambient-noise recorded during the ALPASS (see Fig. 1.11, Mitterbauer et al., 2011) and CBP (see Fig. 1.11, Dando, 2011) projects, but this model is still limited in resolution and coverage by the previously sparse station distribution in the region.

The comparison of a selection of the recent velocity models that have good coverage in the WVBR (Fig. 1.5) demonstrates considerable disagreement between them. In the shallow crust (4km, top row in Fig. 1.5), the model of Ren et al. (2013) shows two separate low-velocity anomalies with shear velocities as low as \sim 2.3km/s, whereas the models of Lu et al. (2018) and Kästle et al. (2018) show higher velocities around \sim 2.9km/s. Lu et al. (2018) show only one low-velocity feature located "in-between" the two of Ren et al. (2013), while these two low-velocity anomalies are present in Kästle et al. (2018), but have low magnitude compared to the surrounding. At mid-crustal depths (16km, bottom row in Fig. 1.5), all models show a single low-velocity anomaly at the border triangle of Austria, Czech Republic and Slovakia, located below the Northeastern Vienna Basin. The magnitudes of this anomaly differ considerably, though. There, the model of Kästle et al. (2018) shows the highest contrast. Note that in the models of Lu et al. (2018) and Kästle et al. (2018) the center of this deeper anomaly is located directly underneath a shallow low-velocity anomaly, raising questions about whether the deep anomaly is an artifact of the inversion process or indeed a physical structure. The model of (Ren et al., 2013), however, shows a slight shift of

this anomaly towards East compared to the low velocities at shallow depth.

1.2.3 Seismic and interpreted profiles

Several published interpreted seismic profiles cross the WVBR, giving detailed but laterally limited insight into the structure of the crust. Notable profiles include the ones published by Tomek & Hall (1993), Hrbcová et al. (2005), Hrbcová & Šroda (2015) and Wessely (2006), as well as an unpublished one by Dvorak et al. (1990).

The reflection profile 8HR, presented in Tomek & Hall (1993) crosses the Carpathian Flysch near the Southern border of the Czech republic (see Fig. 1.11). It images the SE-dipping Bohemian massif, revealing the overthrusting of the Adriatic plate ontop of the European plate. The profile shows no clear seismic reflectors in the deeper crustal structure beneath the Northern Vienna Basin.

The NW/SE-oriented seismic refraction profile CEL09 (Figs. 1.6, 1.11, Hrbcová et al., 2005; Hrbcová & Šroda, 2015) of the CELEBRATION2000 project (Guterch et al., 2003) crosses the entire Bohemian massif, Vienna Basin, and continues further into the Pannonian Basin. The profile shows the Bohemian massif dipping below the Vienna Basin until ~ 10 km depth. The interpretation of this profile is focused on the depth of the Moho (Fig. 1.6) and the authors do not interpret the upper crustal structure in detail.

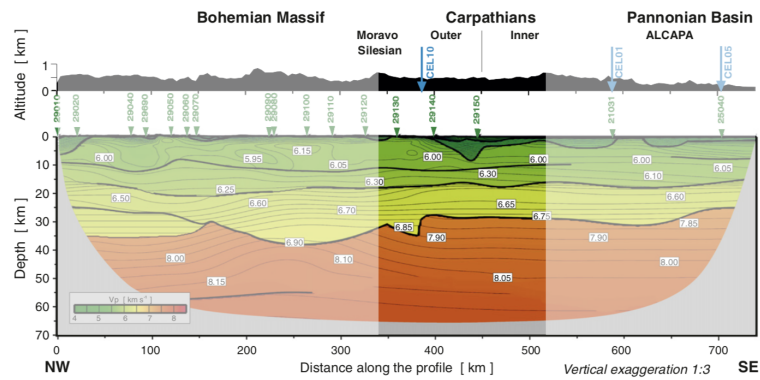


Figure 1.6: Interpreted seismic profile CEL09 crossing the central Vienna Basin (at ~ 450 km distance) modified after Hrbcová & Šroda (2015). The profile provides evidence for the SE-dipping Bohemian massif until depths of ~ 10 km. Below that, no notable velocity-contrasts are visible in the crust. The highlighted area marks the section of this profile within the WVBR. For the location of the profile, see Fig. 1.11

Wessely (2006) presents several interpreted geological profiles that are also oriented NE/SW, crossing the Eastern Alps and Vienna Basin every \sim 10-20km. They show interpretations of the detailed structure of the overthrust nappes of the Adriatic plate and structures that formed within them (e.g., the Vienna Basin), not of the crystalline basement of the Bohemian massif in the West or the Austroalpine basement in the East.

The refraction profile 7R described in an internal report (Fig. 1.7, Dvorak et al., 1990), provided by the colleagues from the Institute of Physics of the Earth in Brno (Petr Špaček, pers. comm.), crosses the Northeastern edge of the Vienna Basin (Fig. 1.11). It reveals a deep geological structure, down to depths of \sim 12km that the velocity models of Ren et al. (2013), Lu et al. (2018), and Kästle et al. (2018) also possibly image (Fig. 1.5).

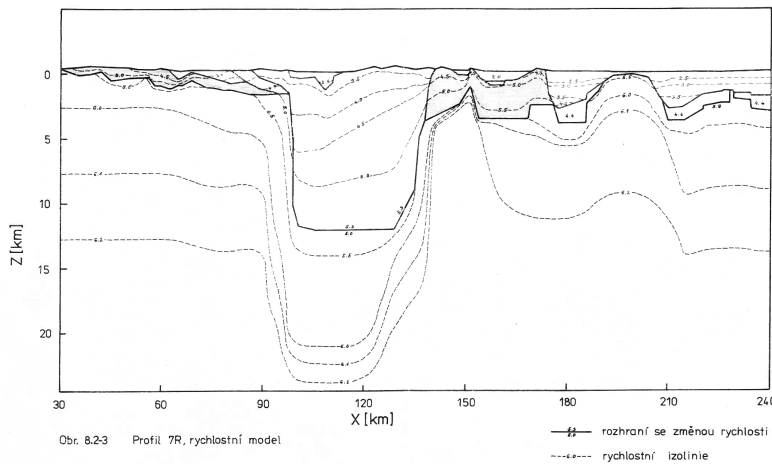


Figure 1.7: Seismic profile 7R crossing the NE edge of the Vienna Basin from Dvorak et al. (1990). The profile shows a deep-reaching geological structure underneath the Vienna Basin that some of the velocity models in the region may have been able to image (see Fig. 1.5). For the location of the profile, see Figure 1.11.

1.2.4 Gravimetry

While seismology is the most commonly applied geophysical discipline to gain knowledge about the structure of the Earth, other disciplines, such as gravimetry provide independent and complementary data and insight on crustal scale. Meurers & Ruess (2009) present a detailed Bouguer gravity map of Austria, based on gravity data recorded since the 1960s. It shows high values of gravity anomaly coinciding with the crystalline basement of the Bohemian massif and a distinct trough in the Vienna Basin. The lowest values in Eastern Austria are found at the Northeastern

Vienna Basin near the border triangle of Austria, Czech Republic, and Slovakia. These values point to an increased presence of low-density sedimentary rocks, which seismic techniques image as low-velocity anomalies (see Fig. 1.5). A broader view of the distribution of gravity anomaly in the WVBR that goes beyond the borders of Austria is given by the World Gravity Map 2012 (Fig. 1.8, Bonvalot et al., 2012). It is based on measurements of surface gravity, as well as satellite altimetry and gravimetry. In this map, the trough associated with the Vienna Basin (a in Fig. 1.8) extends further towards Northeast and appears to follow the shape of the Carpathian arc. The Little Hungarian Plain is marked by a lower-magnitude trough (b in Fig. 1.8). The two basins are separated by the Little Carpathians, which are marked by an increase in gravity anomaly. The Bohemian massif (c in Fig. 1.8) also shows high values that somewhat follow the shape of the Bohemian Spur in Figure 1.3. The deep crustal roots of the Alps are imaged with decreased values of gravity anomaly due to the high-density rocks of the mantle being located in greater depths.

1.2.5 Stress Field

The stress-field controls tectonic deformation and seismic activity. To understand the potential for future large earthquakes it is crucial to gain insight into the regional stress-field acting today. However, gaining this insight is not trivial.

All measurements of the stress-field are proxy-based, where a physical process is interpreted to be a proxy of the acting stress-field. Common techniques include borehole breakouts, where the orientation of a collapsing borehole wall is interpreted to be indicative of the orientation of maximum horizontal compressive stress σ_H (Zoback, 2010), or focal mechanisms of earthquakes, where the orientation of the ruptured fault of larger earthquakes is similarly interpreted to follow the stress-field (Stein & Wysession, 2003; Shearer, 2009). The broad regional stress-field controlling crustal movement on larger scales, however, may be different from the locally measured stress-field at a given point, e.g., by borehole breakouts (e.g., Brudy et al., 1997). The interpretation of the stress-field based on focal mechanisms relies on a catalogue of fault plane solutions that properly represents the entirety of seismic activity. To account for the fact that individual focal mechanisms give only an approximate (and biased) measurement of the stress-field orientation, collections of focal mechanisms are sometimes inverted for the stress-field orientation to gain more robust insight (Gephart & Forsyth, 1984; Angelier, 2002).

In some areas in the Alps, measurements have been performed with great effort, e.g., in the Molasse basin in Southern Germany (e.g., Reinecker et al., 2010), or along the Western Alps (e.g., Heidbach et al., 2018). Reinecker et al. (2010) show highly consistent N/S-orientations of σ_H in the Molasse, mainly based on borehole breakouts, that complements earlier measurements in the Western Alps, mainly based on focal mechanisms (see e.g., Heidbach et al., 2018). They

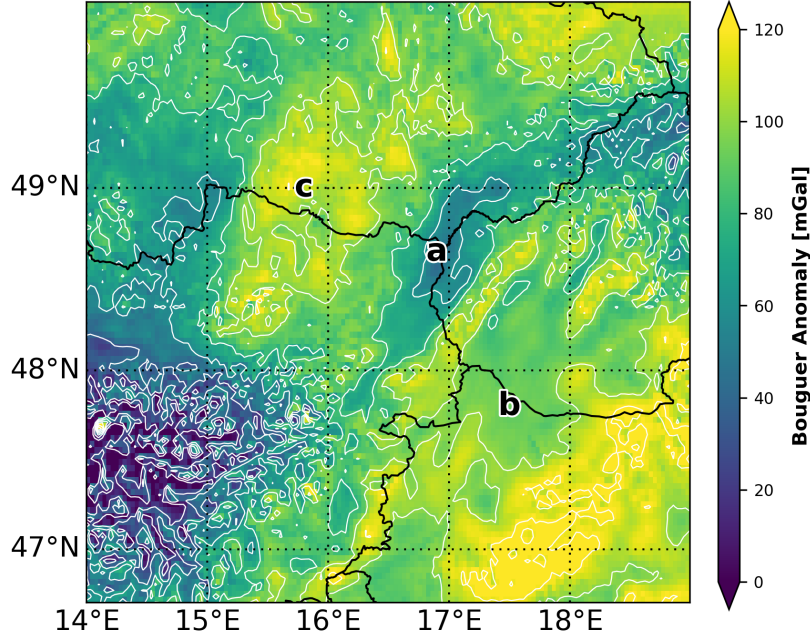


Figure 1.8: Map of Bouguer gravity anomaly in the wider Vienna Basin region extracted from Bonvalot et al. (2012). In the Vienna Basin (a), a trough in the anomaly represents the presence of low-density sedimentary rocks. The Little Hungarian Plain (b) is mapped with a trough of lower magnitude and the two basins (a and b) are separated by increased values of Bouguer anomaly, collocated with the Little Carpathians. The crystalline basement of the Bohemian massif (c) appears with high values of Bouguer anomaly, consistent with high-density rocks of the basement. The lowest values, apart from the Eastern Alps, appear at the Northeastern edge of the Vienna Basin.

argue that the stress-field may be dominated by the gravitational potential of the Alps, leading to orientations of σ_H nearly perpendicular to them.

In the Eastern Alps and WVBR, however, the stress-field is sometimes interpreted differently. Here, Reinecker & Lenhardt (1999) report σ_H -orientations normal to the Bohemian Spur, based on focal mechanisms and borehole breakouts, and argue that the Eastern Alps are subject to a heterogeneous stress field, where the Bohemian Spur acts as an indenter that dominates the stress field (Fig. 1.9).

Similarly, Bada et al. (1998) and Gerner et al. (1999) show a distribution of σ_H -orientations in the WVBR normal to the Bohemian massif from focal mechanisms and borehole breakouts. They perform finite-element-modelling, which assumes the Bohemian massif as an indenter, to find

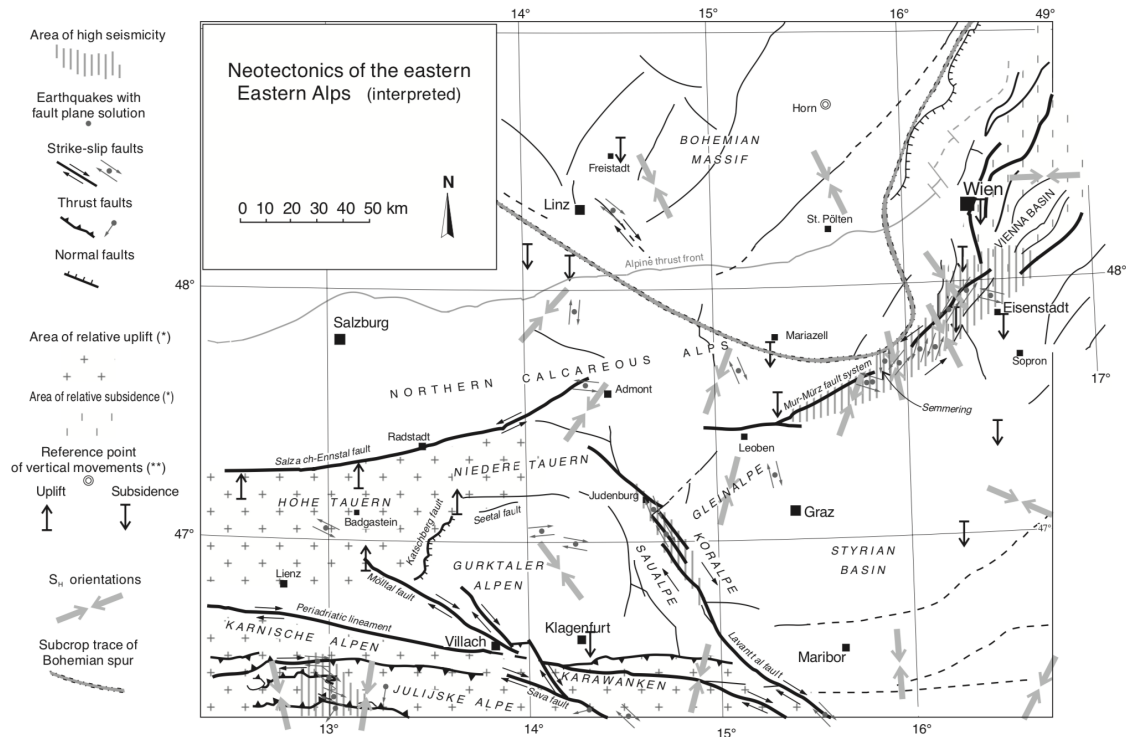


Figure 1.9: Map of present-day stress-field in the wider Vienna Basin region, from Reinecker & Lenhardt (1999). Grey arrows mark the orientation of the maximum horizontal compressive stress σ_H (here S_H), approximately normal to the Bohemian Spur.

these orientations. When considering only horizontal slip vectors, however, they report consistent NE/SW-orientations of σ_H in the WVBR. The authors note that their stress map "does not reflect the local stress" in the Little Hungarian Plain (Bada et al., 1998), and thus by extension the WVBR.

These studies (Reinecker & Lenhardt, 1999; Bada et al., 1998; Gerner et al., 1999) raise questions about why the MML and VBTFS are seismically active today, if a principal stress axis was oriented nearly perpendicular to those faults.

Bada et al. (2007) present a map of the present-day stress field in the Pannonian region, including the WVBR, based on an updated compilation of focal mechanisms, borehole breakout analyses and in situ stress measurements (Fig. 1.10). They do not model the stress-field and rely exclusively on measurements, smoothed over the study region. The authors find a change from ~N/S-orientations of σ_H in the West and North of the study region to ~NE/SW-orientations

approximately South of the MML and VBTFS. They conclude that the "Mur–Mürz–Žilina fault zone" (roughly equivalent to the WVBR), is subject to a NNE/SSW-oriented strike-slip stress regime, which is consistent with seismic activity observed today along the MML, although in disagreement with earlier studies (Reinecker & Lenhardt, 1999; Bada et al., 1998; Gerner et al., 1999).

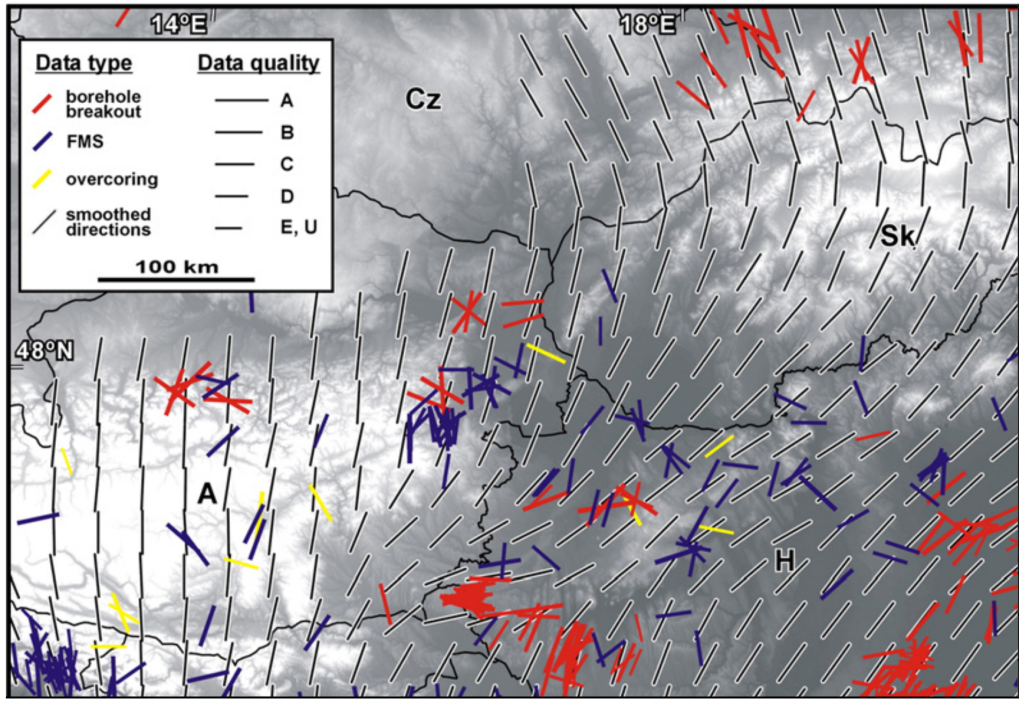


Figure 1.10: Map of present-day stress-field in the wider Vienna Basin region, modified from Bada et al. (2007). N/S-orientations of σ_H in the Western and Northern parts of the WVBR. Rotation towards NE/SW-orientations South of the MML and VBTFS.

The Stress Map of the Mediterranean and Central Europe 2016 (Heidbach et al., 2018) is extracted from a regularly updated compilation of stress-field measurements all over the world, the World Gravity Map (Bonvalot et al., 2012). It provides pointwise measurements of stress-field orientations that allow insight into the regional consistency of these measurements. In some regions they are highly consistent (e.g., Western and Central Alpine foreland), while the measurements in the WVBR vary considerably and are relatively sparse (some measurements depicted in Fig. 1.10). These measurements are the data for previously mentioned studies (e.g., Reinecker & Lenhardt, 1999; Bada et al., 1998, 2007). As the compilation is updated with new measurements, more detailed insight becomes possible, and their interpretation may change (see e.g., Bada et al. (1998) and Bada et al. (2007)). Since the study of Bada et al. (2007), new focal-mechanism-derived stress field orientations have been added to the database that also show consistent ~NNE/SSW-

orientations in Western Slovakia (Heidbach et al., 2018). In that area, Fojtíková et al. (2010) determined and inverted focal mechanisms of micro-earthquakes in the Little Carpathians for the regional stress-field and report a ~NE/SW-orientation of compression.

In the Vienna Basin, the stress-field orientation and regime has apparently changed in the last 17Ma (see, Decker et al., 2005, and references therein). The formation of the pull-apart basin is interpreted to be caused by NNE/SSW-oriented compression from the Karpatian to early Pannonian as part of lateral extrusion (Frank et al., 1997), followed by fault reactivation due to E-W-oriented compression in the late Pannonian (Peresson & Decker, 1997). Decker et al. (2005) argue that in the early Pleistocene NE/SW-extension has caused graben formation in the Vienna Basin and subsequent ~N/S-compression in late Pleistocene caused normal faulting and rollover. Marsch et al. (1990) report that vertical stress-decoupling across the Steinberg fault (at the Western edge of the Vienna Basin) leads to ~N/S-orientations of σ_H above and ~NNE/SSW-orientations below the fault today.

1.3 Seismological station and data coverage

1.3.1 Permanent national networks

The backbone of continuous, high-quality, and broadband seismological observations are the national seismic networks. The operators of the national networks of Austria (Austrian Seismic Network, 1987), Czech Republic (Czech Regional Seismic Network, 1973), Hungary (Hungarian National Seismological Network, 1992), Slovakia (National Network of Seismic Stations of Slovakia, 2004), and Slovenia (Seismic Network of the Republic of Slovenia, 2004) provide their data to the public and they are available, e.g., through ORFEUS web services.

In the wider Vienna Basin region, permanent stations are relatively sparse (see Fig. 1.11) and several temporary seismological experiments have been performed in the past years to complement these data and gain more detailed insight into the structure and processes within the Earth.

1.3.2 Previous temporary seismological installations

The Central European Lithospheric Experiment Based on Refraction 2000 (CELEBRATION2000, Guterch et al., 2003) consisted of 14 refraction profiles on continental scale (in total 8900km profile length). Of these profiles, the profile CEL09 crosses the WVBR (see Fig. 1.11). Hrubcová et al. (2005) and Hrubcová & Šroda (2015) intrepret this profile in terms of lithospheric structure (see Fig. 1.6).

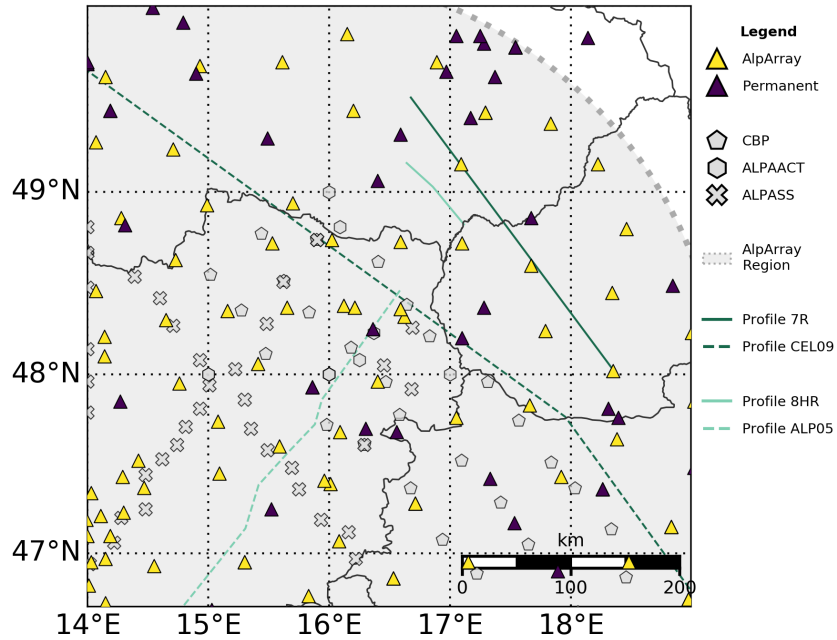


Figure 1.11: Map of seismic stations in the wider Vienna Basin region and several profiles crossing the region (dark green ones shown in Figs. 1.6, 1.7). This thesis uses data of the permanent stations of the national networks (Austrian Seismic Network, 1987; Czech Regional Seismic Network, 1973; Hungarian National Seismological Network, 1992; National Network of Seismic Stations of Slovakia, 2004; Seismic Network of the Republic of Slovenia, 2004) and the temporary AlpArray stations (Hetényi et al., 2018a). The study region is located at the Northeastern edge of the AlpArray project (shaded background, see Fig. 1.12). Previous seismic installations include the Carpathian Basin Project (CBP, Dando, 2011), the Alpine-Pannonian Active Tectonics project (ALPAACT, Brückl et al., 2014), and the Alpine Lithosphere and Upper Mantle Passive Seismic Monitoring project (ALPASS, Brückl et al., 2011). The marked profiles are: 7R (Fig. 1.7, Dvorak et al., 1990), CEL09 (Fig. 1.6, Hrubcová et al., 2005), 8HR (Tomek & Hall, 1993), and ALP05 (Brückl et al., 2003).

During the ALP 2002 experiment (Brückl et al., 2003), 14 profiles with a total length of 4300km were installed across the Eastern Alps. While some profiles of this experiment have been investigated to retrieve lithospheric structure (e.g., Bleibinhaus & Brückl, 2006), no studies have been published discussing the crustal structure along profile ALP05, which reaches into the Vienna Basin (see Fig. 1.11).

As part of the Alpine Lithosphere and Upper Mantle Passive Seismic Monitoring project (AL-PASS, Brückl et al., 2011), 89 temporary stations were installed along three profiles crossing the Eastern Alps and in one cluster in the Vienna Basin (\times in Fig. 1.11). The stations that were deployed in the WVBR consisted mainly of short-period sensors. Mitterbauer et al. (2011) used these data to retrieve a velocity model of the mantle that aims at imaging the East-Alpine slab.

The High-resolution Seismic Tomography (HST) network of the Carpathian Basin Project (CBP, Dando, 2011) consisted of three NE/SW-oriented lines, spaced \sim 40km, with \sim 15 stations in each line every \sim 30km. The network reached into the WVBR (\blacklozenge in Fig. 1.11) and data were recorded for 16 months in 2006 and 2007. While the focus of the project was on the structure of the Pannonian basin, the shear-velocity model of Ren et al. (2013) (Fig. 1.5) provides insight into the crustal structure of the WVBR with previously unachieved resolution.

The Alpine-Pannonian Active Tectonics project (ALPAACT, Brückl et al., 2014) was a local installation of 9 broadband and short-period stations in the WVBR, later complemented by a one-year installation of an additional 10 stations provided by GeoForschungsZentrum, Potsdam (GFZ) (\bullet in Fig. 1.11). The aim of the project was to study the seismicity along the MML in detail to gain insight into the tectonic processes and implications for seismic hazard in the WVBR. Brückl et al. (2014) report that the earthquakes along the MML include strike-slip-, normal- as well as reverse-faulting mechanisms. The initial 9 stations are now part of TUSeisNet (<http://gp.geo.tuwien.ac.at/gp/tuseisnet>).

1.3.3 AlpArray

While a number of large-scale seismic experiments have been conducted in the WVBR, a dense installation of seismic broadband sensors to record data over several years across the entire region has only been realized in recent years: the AlpArray project (Hetényi et al., 2018a).

AlpArray is an international project of 24 institutions across Europe (www.alparray.ethz.ch, Hetényi et al., 2018a). It aims at advancing our understanding of the Alpine Orogen and surrounding regions with a previously unachieved dense coverage of the entire Alps with broadband seismometers. In total, the network consists of almost 700 seismic stations, comprised of \sim 240 newly installed temporary broadband stations, \sim 30 ocean bottom seismometers, as well as \sim 400

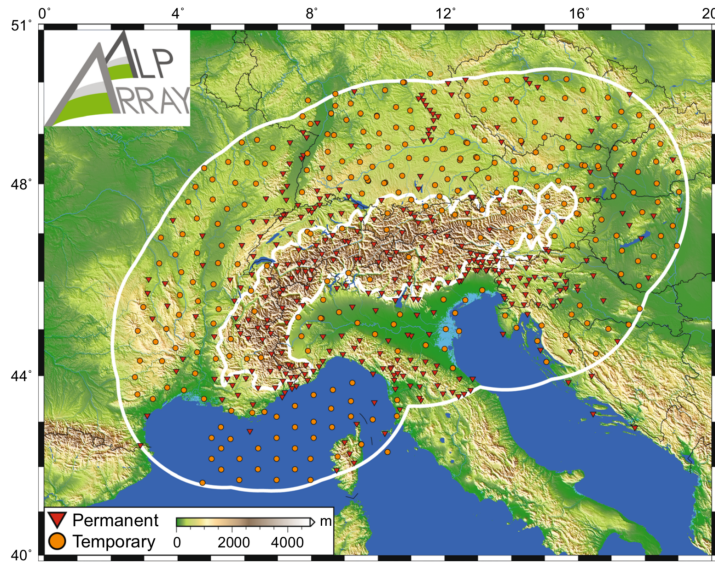


Figure 1.12: Station map of AlpArray. The permanent and temporary broadband stations (respectively red triangles and orange circles) cover the area within 250 km of the smoothed 800-m altitude line of the Alps (outer and inner thick white lines). Figure and description from Hetényi et al. (2018a).

permanent stations (Fig. 1.12). The stations are spaced \sim 40km across the entire Alps and are located within \sim 250km of the Alpine mountain chain, defined as 800m altitude (see Fig. 1.12).

AlpArray provides an unprecedented opportunity to study the Alpine region on multiple scales. While the data acquisition is still ongoing as of this thesis, some studies utilizing this data have already been published. Kalmár et al. (2018) used this data to study mantle structure and geo-dynamics on a larger regional scale. Lu et al. (2018), as described above, have computed a shear-velocity model of crust and mantle. Hetényi et al. (2018b) report on the crustal structure and Moho depths along the EASI profile, a N/S profile across the Eastern Alps complementary to AlpArray. Fuchs et al. (2018) studied the capabilities of AlpArray to detect and locate rockslides. Schneider et al. (2018) examined seismo-acoustic signals of an explosion at a gas-hub at the Austrian-Hungarian border recorded across AlpArray to infer source properties of the explosion. Kolínský et al. (2019) used data recorded on the network to study arrival angles of teleseismic waves and to gain insight into velocity anomalies perturbing the wavefield along its propagation path.

This thesis utilizes data of AlpArray and the permanent national networks to provide new insights into structure and stress in the WVBR on crustal scale. The used data are the continuous

seismic records of the years 2015 to 2017 (used in Sections 2 and 4), as well as the seismic records of the 2016 to 2017 Alland earthquake sequence (used in Section 3). For more details on these data, see the relevant sections (Sections 2.2, 3.2, 4.2).

1.4 Scientific questions and thesis outline

Our current understanding of the wider Vienna Basin region leads to a number of open scientific questions around the crustal structure and stress field in the region. This thesis aims to address some of them in the following sections:

- **Section 2:** What is the crustal structure in the wider Vienna Basin region? Recent velocity models exhibit disagreement about the distribution of shear velocities in the crust (Fig. 1.5). All of those models (Ren et al., 2013; Lu et al., 2018; Kästle et al., 2018) reveal a deep-seated low-velocity anomaly beneath the Northeastern Vienna Basin, but it remains unclear whether it is an artifact introduced during the inversion process or a physical structure. Furthermore, the lateral extent of imaged features also differs considerably between the models. What can be considered a "high-resolution" model depends on available data and context, and AlpArray (Hetényi et al., 2018a) provides a unique opportunity to compute a new velocity model of the wider Vienna Basin region with previously unachieved resolution, providing new and detailed insight into the crustal structure.
- **Section 3:** What are the source properties of the Alland earthquake sequence? What are its implications for the regional stress-field? While seismic activity along the Mur-Mürz-Line is plentiful, earthquakes are observed rarely to the North of it. Still, the most significant earthquake in the region, that of Neulengbach/Ried am Riederberg in 1590, was located at the Northern edge of the Eastern Alps (Hammerl & Lenhardt, 2013). The 2016-2017 Alland earthquake sequence, located ~20km Southwest of Vienna, occurred not far from the 1590 event, and in an area that was seismically quiet over historical times (Fig. 1.4, AEC, 2016). This sequence may provide important insight into the geometry of faults North of the Mur-Mürz-Line and give indications for the orientation of the present-day stress field in the wider Vienna Basin region.
- **Section 4:** How is the present-day stress-field in the wider Vienna Basin region oriented? While the Alland sequence may give important insight in that regard, it represents one more data point in a region where pointwise stress-field-measurements do not appear to align strictly along one orientation (measurements depicted in Fig. 1.10). Previous studies on the regional stress-field (Bada et al., 1998; Gerner et al., 1999; Reinecker & Lenhardt, 1999) have assumed the Bohemian massif as a rigid indenter that results in stress-field orientations

normal to it. These orientations, however, are almost perpendicular to fault systems in the region, specifically the MML and VBTFS, raising questions about why they are seismically active. Bada et al. (2007) report orientations that are compatible with seismic activity along these faults (see Fig. 1.10). Azimuthal anisotropy of surface waves aligns with the orientation of maximum horizontal stress (Nur, 1971) in the upper crust, if confining stress is small, so that cracks remain open and aligned with the stress field. This provides an independent proxy of the stress-field orientation in the shallow crust that allows spatially broad insight, complementary to the existing pointwise measurements. In the deeper crust, crystals may align during continued deformation, resulting in fast orientations of surface waves at longer periods.

2 Ambient-noise tomography of the wider Vienna Basin region

This section has been published in Geophysical Journal International as:

Schippkus, S., Zigone, D., Bokelmann, G., the AlpArray Working Group. (2018) Ambient-noise tomography of the wider Vienna Basin region. *Geophys. J. Int.*, **215**, 102 - 117, Oxford University Press. doi:10.1093/gji/ggy259

Abstract

We present a new 3D shear-velocity model for the top 30km of the crust in the wider Vienna Basin region based on surface waves extracted from ambient-noise cross-correlations. We use continuous seismic records of 63 broadband stations of the AlpArray project to retrieve inter-station Green's Functions from ambient-noise cross-correlations in the period range from 5s to 25s. From these Green's Functions, we measure Rayleigh group travel-times, utilizing all four components of the cross-correlation tensor, which are associated with Rayleigh waves (ZZ, RR, RZ, ZR), to exploit multiple measurements per station pair. A set of selection criteria is applied to ensure we use high-quality recordings of fundamental Rayleigh modes. We regionalize the inter-station group velocities in a 5km by 5km grid with an average path density of ~20 paths per cell. From the resulting group-velocity maps, we extract local 1D dispersion curves for each cell and invert all cells independently to retrieve the crustal shear-velocity structure of the study area. The resulting model provides a previously unachieved lateral resolution of seismic velocities in the region of ~15km. As major features, we image the Vienna Basin and Little Hungarian Plain as low-velocity anomalies, and the Bohemian Massif with high velocities. The edges of these features are marked with prominent velocity contrasts correlated with faults, such as the Alpine Front and Vienna Basin transfer fault system. The observed structures correlate well with surface geology, gravitational anomalies, and the few known crystalline basement depths from boreholes. For depths larger than those reached by boreholes, the new model allows new insight into the complex structure of the Vienna Basin and surrounding areas, including deep low-velocity zones, which we image with previously unachieved detail. This model may be used in the future to interpret the deeper structures and tectonic evolution of the wider Vienna Basin region, evaluate natural resources, model wave propagation, and improve earthquake locations, among others.

2.1 Introduction

Accurate seismic velocity models improve our understanding of structures and processes in the solid Earth. At regional scale, such models are useful for seismic hazard assessment, better location of regional and local seismic events, understanding the tectonic evolution of a region, and improving the evaluation of natural resources, among others. They provide insight into greater

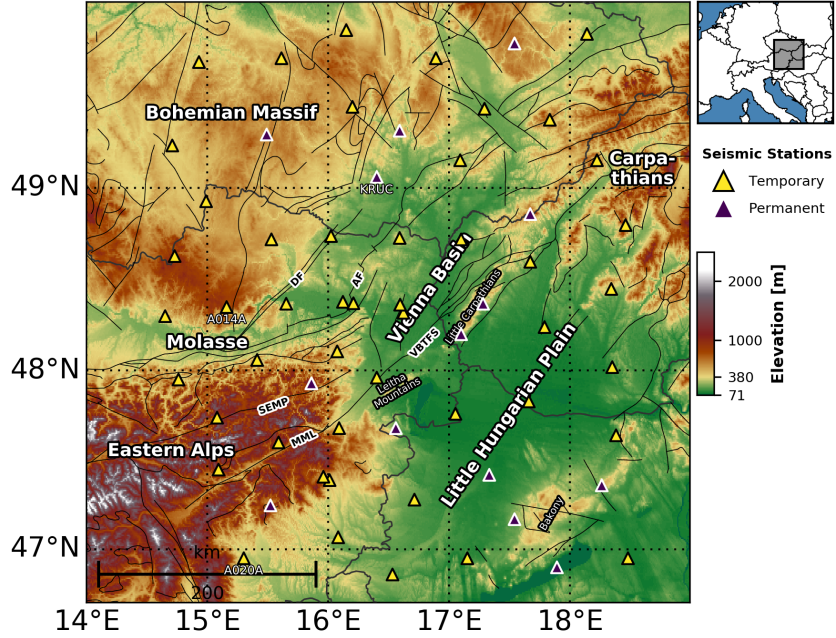


Figure 2.1: Map view of the study area. Permanent stations are marked as purple triangles, temporary stations as yellow triangles. Major structures are labelled: Bohemian Massif, Molasse, Vienna Basin, Little Hungarian Plain, Eastern Alps, Carpathians. Faults are marked as black lines, compiled from the European Database of Seismogenic Faults (EDSF, Basili et al., 2013) and International Geological Map of Europe (IGME5000, Aschk, 2005) databases. Major faults are labelled: Mur-Mürz-Line (MML), Salzach-Ennstal-Mariazell-Puchberg Fault (SEMP), Diendorf Fault (DF), Alpine Front (AF), Vienna Basin transfer fault system (VBTFS).

depth regions, which are not well-sampled by other geophysical methods, and not accessible by near-surface geology. In this study, we present a new seismic velocity model of the wider Vienna Basin region to provide new insight into its complex structure. Because of population density and sensitive infrastructure, understanding the regional processes and structures in and around the Vienna Basin - one of the seismically most active regions in Austria - is of critical importance.

The Vienna Basin is a thin-skinned pull-apart basin in the Alpine-Carpathian transition zone that spans across Eastern Austria, Southern Czech Republic, and Western Slovakia (Fig. 2.1). Due to its special location in this transition zone it has a complex tectonic history, which has been influenced by the changing tectonic regimes in the last 18Ma (see Lee & Wagreich (2016) and references therein). The Vienna Basin was formed on top of thrust sheets in the Eastern Alps (Hölzel et al., 2010), which have been caused by the convergence of the African and European

plates. Lateral extrusion to the East during the late Oligocene and early Miocene (Ratschbacher et al., 1991a; Wölfle et al., 2011) was associated with the formation of strike-slip faults such as the sinistral strike-slip Salzach-Enns-Mariazell-Puchberg (SEMP) and Mur-Mürz Line (MML) faults (Fig. 2.1). All these factors have played a role in the formation of the Vienna Basin, leading to a relatively complex tectonic structure.

Previous studies in the region have investigated the Vienna Basin and its surroundings extensively (e.g., Brix & Schultz, 1993; Wessely, 2006; Behm et al., 2007; Brückl et al., 2010; Ren et al., 2013; Behm et al., 2016). Brix & Schultz (1993) and Wessely (2006) give insight into its geological structure using surface geology classifications, borehole data, and data from non-public seismic surveys. Behm et al. (2007) present a crustal 3D P-wave velocity model based on wide-angle reflection and refraction data. They find low velocities associated with the Vienna Basin, but the data did not allow distinguishing it from the Little Hungarian Plain. Brückl et al. (2010) studied Moho depths using controlled source seismic experiments and elastic plate modeling, and report Moho depths of ~30-40km in the study area. Ren et al. (2013) and Behm et al. (2016) both present 3D shear-velocity models based on ambient-noise tomography. Ren et al. (2013) use data of the regional Carpathian Basins Project (CBP, Dando, 2011) and South Carpathian Project (SCP, Ren et al., 2012), combined with permanent station data. The authors image low-velocity zones associated with sedimentary basins - including deep low velocities beneath the Vienna Basin - with a lateral resolution of ~60km. Behm et al. (2016) use data of the ALPASS (Mitterbauer et al., 2011) and CBP (Dando, 2011) projects and measure low Rayleigh and Love group velocities in the Vienna Basin at longer periods up to 20s. The lateral resolution of these studies in and around the Vienna Basin is limited by relatively poor station coverage (Behm et al., 2016), measurements along only a few profiles (Behm et al., 2007; Brückl et al., 2010), or a broader regional focus (Ren et al., 2013). A high-resolution model of seismic velocities in the region is currently missing.

We compute a new high-resolution crustal 3D shear-velocity model of the wider Vienna Basin region using ambient-noise tomography. This method is based on the extraction of estimated Green's Functions (GFs) from inter-station cross-correlations of ambient seismic noise, which allow to create virtual sources at every passive seismic station (see Campillo & Roux (2015) for a review paper). GF retrieval from ambient-noise cross-correlations has revolutionized the use of seismic arrays for imaging and monitoring purposes at various scales and is now an established technique with many proven applications (e.g., Shapiro et al., 2005; Nishida et al., 2009; Poli et al., 2011; Lin et al., 2012; Ren et al., 2013; Brenguier et al., 2014; Molinari et al., 2015; Nakata et al., 2016; Kästle et al., 2018). It allows to gather information about the structure of the Earth between two seismic stations without using an active or earthquake source, as the retrieved GFs contain broadband information about dispersive surface waves in the microseism period band (Longuet-Higgins, 1950; Hasselmann, 1963). As the amount of available seismic records is only controlled

by the number of stations, noise-based surface-wave tomography has improved the apparent resolution of seismic velocity models by capitalizing on the recent expansion of seismological networks (e.g., Ben-Zion et al., 2015; Boue et al., 2014; Lin et al., 2009, 2013; Roux et al., 2016). In this study, we will take advantage of the recent deployment of a dense seismic network in the Alpine region as part of the AlpArray project (AlpArray Seismic Network, 2015) to image the wider Vienna Basin region with improved resolution.

In the following sections, we present the steps taken to compute the new shear-velocity model in the wider Vienna Basin region: 2.2) Data used for this study, 2.3) Retrieval of Green's Functions from ambient noise, 2.4) Measurement of Rayleigh-wave group velocities from GFs, 2.5) Inversion of group velocities to regionalize the measurements, 2.6) Inversion of group-velocity maps for shear-velocity structure. Finally, we will discuss our model with respect to previous seismological and gravitational studies, as well as insights from surface geology and borehole data.

2.2 Data

AlpArray is an international project of 24 institutions across Europe (www.alparray.ethz.ch). It aims at advancing our understanding of the Alpine Orogen and surrounding regions with a previously unachieved dense coverage of the entire Alps with broadband seismometers. This will enable new studies with improved resolution. In total, the network consists of almost 700 seismic stations, comprised of ~240 newly installed temporary broadband stations, ~30 ocean bottom seismometers, and ~400 permanent stations.

The data used in this study consists of continuous seismic records of 16 permanent stations (of the Austrian Seismic Network, 1987; Czech Regional Seismic Network, 1973; Hungarian National Seismological Network, 1992; National Network of Seismic Stations of Slovakia, 2004) and 47 temporary broadband stations of the AlpArray seismic network (AlpArray Seismic Network, 2015). Fig. 2.1 gives an overview of the study area and the locations of the permanent (purple) and temporary (yellow) stations. The inter-station distances range from 20 to 340km - with an average station spacing of ~40km - and an even distribution of inter-station azimuths. Faults in the area (black lines in Fig. 2.1) are compiled from the European Database of Seismogenic Faults (EDSF, Basili et al., 2013) and the International Geological Map of Europe (IGME5000, Aschk, 2005). The available seismic records range from 0.5yr up to 2yrs in length and have been recorded between 02/2015 and 04/2017.

2.3 Ambient-noise cross-correlations

In this study, we measure inter-station surface-wave travel times on estimated Green's Functions (GFs), extracted from inter-station cross-correlations of ambient-noise. We estimate group velocities from these travel times assuming great circle propagation. The group velocities are then used to image the crustal structure using a tomographic inversion procedure. In this section, we discuss the retrieval of GFs. The continuous seismic records are processed in two major steps to compute the estimated GFs: Pre-processing of the records and Green's Function retrieval.

2.3.1 Pre-processing

Pre-processing aims to render the resulting cross-correlation functions (CCFs) more stable and closer to the true GFs by removing transient sources (e.g., earthquakes) from the continuous seismic records. The wave field produced by a transient source is not diffuse and may introduce spurious arrivals in the estimated GFs (Bensen et al., 2007). To be able to remove these signals, we divide the continuous records into smaller time windows. These time windows need to be long enough, so that the diffuse wave field is sufficiently well-recorded on any two seismic stations. They also should be reasonably short to not remove too much data when removing transient sources (Seats et al., 2011). We tested common pre-processing methods, such as windowing, whitening (Bensen et al., 2007, and references therein), and one-bit-normalization (Cupillard et al., 2011), extensively. To determine the final pre-processing scheme, we compared the signal-to-noise ratio (SNR) of the resulting CCFs for 384 combinations of pre-processing parameters and chose the scheme that yields the highest SNR while providing stable increase in SNR with the number of stacked days (see Section A.1). We define SNR as the peak amplitude divided by the standard deviation in a noise-window, where the noise-window is the last 20% of a given CCF. We decided to pre-process the data in 7 steps:

1. Remove the instrument response for each station.
2. Remove glitches in the signal by clipping the amplitudes at 15 times the standard deviation of each daily trace.
3. Cut continuous seismic records into non-overlapping 30-minute windows, resulting in 48 sub-traces per day.
4. Remove sub-traces that contain **a)** large gaps (more than 20% of the sub-trace) or **b)** transient sources, detected by an energy threshold. The threshold is defined such that the mean energy of the 30-minute sub-trace may not exceed 2.5 times the mean energy of the original 24h trace of the same day.

5. Whiten the spectrum of the sub-traces, using a water level, to reduce the impact of amplitude variations on the measurements (Bensen et al., 2007).
6. Dampen remaining transient signals (e.g., small earthquakes that may have passed the energy threshold) by clipping the amplitudes at 4 times the standard deviation.
7. Apply a taper to the edges of the sub-traces to prevent border artifacts in the cross-correlations.
8. Downsample all records to 4Hz to reduce further computational cost.

2.3.2 Green's Function retrieval

We extract estimated GFs from the pre-processed sub-traces by cross-correlating and stacking them. For each station pair, we first cross-correlate the remaining sub-traces after pre-processing and then stack all sub-traces linearly. We compute daily stacks for quality control and to help identify corrupted data. In Fig. 2.2 (top views), we show the ZZ-component daily stacks as correlograms, bandpass-filtered between 5-25s and normalized, for two representative station pairs.

Both examples show arrivals on the causal and acausal parts of the cross-correlation that are stable in time. The station pair KRUC-A014A (Fig. 2.2a) is aligned SW-NE and shows similar energy levels in the causal and acausal parts of the cross-correlation. Additionally, we see a slight change in amplitude between days ~ 300 and ~ 400 , concurrent with the summer months. Note that day 0 is the first day of simultaneously available data and not related to days of year. In Fig. 2.2b we show the station pair A014A-A020A, which is aligned N-S and shows strong asymmetry of the causal and acausal parts. Still, this example shows stable phases in both the causal and acausal parts of the cross-correlation. We observe a change in amplitude with time for roughly 100 days (Days ~ 200 to ~ 300), much more pronounced than in the symmetric example (Fig. 2.2a). This observation, consistent throughout the whole data set, leads us to assume a strong noise source in N direction for most of the year and a relative weakening of that source during the summer months (Stehly et al., 2006; Juretzek & Hadzioannou, 2016).

One of the main assumptions in GF retrieval is a homogeneous noise-source distribution (e.g., Shapiro & Campillo, 2004), which is almost never achieved, except in designed experiments with a controlled noise-source distribution (e.g., Roux et al., 2004). As illustrated above, our study is also affected by a non-uniform noise-source distribution. Therefore, we stack the daily estimated GFs to sample the different noise-source distribution regimes of the seasons and reduce possible effects of seasonality on the travel-time measurements (Yang et al., 2007). For each station pair, we stack all available days to retrieve a final stack (Fig. 2.2, middle views). In the two shown examples (Fig. 2.2), we observe a difference in frequency content on the causal and acausal parts of the final CCF - also visible in the daily stacks - that results from the different frequency content

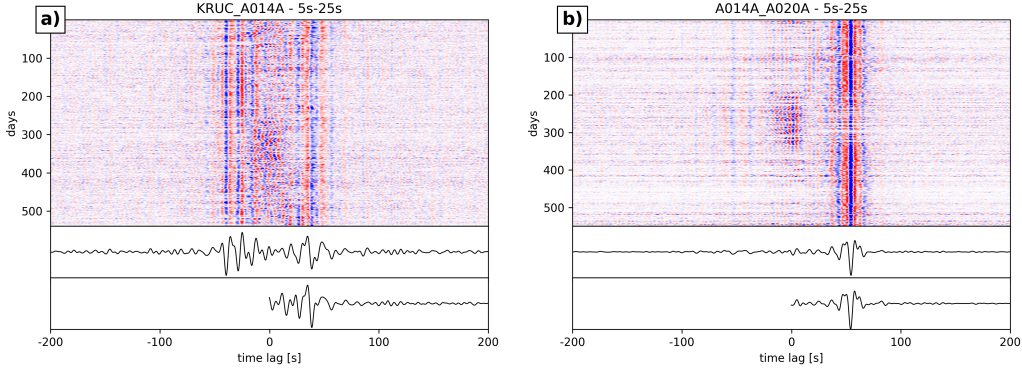


Figure 2.2: Example correlograms for two station pairs. In the top views, each line represents a daily stacked cross-correlation. The middle views show the full cross-correlation stacks. The bottom views show the final folded cross correlation, i.e. the estimated Green’s Function. All data are bandpass-filtered between 5s and 25s. **a)** Station pair KRUC - A014A shows stable symmetric cross correlations over the available days. **b)** Station pair A014A - A020A shows asymmetric cross correlations for most days, with a significant change in amplitudes during the summer months (days ~ 200 to ~ 300). For station locations see Figure 2.1.

of the noise sources in opposite propagation directions (Yang & Ritzwoller, 2008). To mitigate this effect and broaden the frequency content, we fold the cross-correlations (Fig. 2.2, bottom views) to merge low and high frequency information (Verbeke et al., 2012) for the following travel-time measurements.

We compute the full cross-correlation tensor, i.e. we cross-correlate all 9 component pairs of Z, N, E for each station pair (ZZ, NN, EE, ZN, NZ, ZE, EZ, NE, EN). Finally, we rotate the cross-correlation tensor to receive radial, transversal and vertical components (ZZ, TT, RR, ZR, RZ, ZT, TZ, RT, TR). We retrieve a total of 17,577 estimated GFs (9 component pairs times 1953 station pairs).

In Fig. 2.3 we show the combined full cross-correlation tensor for all stations. Each component is represented as a plot of all final folded cross-correlation stacks, sorted and binned by inter-station distance (1km bins). We identify clear wave trains on the components associated with Rayleigh waves (ZZ, RR, RZ, ZR) and Love waves (TT) according to their respective polarization. The observed Love waves with velocities ~ 3.7 km/s are generally faster than the Rayleigh waves at ~ 3.3 km/s, as indicated by the steeper slope of the Love wave train. The energy on the Rayleigh wave components is not uniform across components with the ZZ component showing a clearer signal than the ZR, RZ, and RR components, where the RR component has the weakest signal. This lack of energy is explained by the sensitivity of the horizontal records in this study to the limitations of temporary installations (Fuchs et al., 2015). Despite such limitations, the Rayleigh

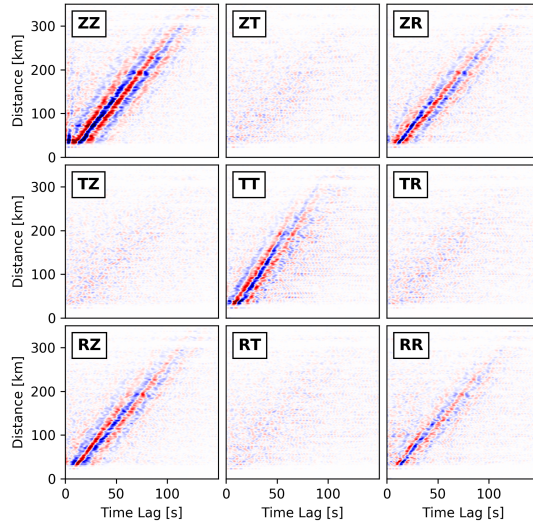


Figure 2.3: Full cross-correlation tensor, combined from all stations. Each component is represented as a subplot of cross-correlations binned by distance (1km bins). Waveforms are bandpass-filtered 5-25s. ZZ, RR, ZR, RZ components show the Rayleigh wave train, while the TT component shows the higher-velocity Love-wave train. The cross terms (ZT, TZ, TR, RT) contain little and incoherent energy.

waves are identifiable on all four components. On the ZZ component, we also see very fast arrivals near 0 seconds lag time for distances smaller than ~ 80 km. These fast arrivals are also visible, although much weaker, on the ZR and RZ components. They may be related to near-vertical incident body phases (Pedersen, 2017) and need to be taken into account to not drastically overestimate inter-station Rayleigh wave velocities. Our selection criteria presented in section 4 already remove those measurements, without specifically tuning them for this. The cross terms (TR, RT, ZT, TZ) also carry some energy, but no clear arrivals can be identified. In this study, we focus on the analysis of Rayleigh waves and measure group velocities on all four relevant cross-correlation tensor components (ZZ, RR, RZ, ZR). We do not analyse Love waves, because they would require an adapted dispersion curve measurement and selection process (see section 2.4), and should ideally be inverted jointly with Rayleigh waves to receive an anisotropic shear-velocity model (Jaxybulatov et al., 2014; Mordret & Shapiro, 2015), which is beyond the scope of this paper.

2.4 Rayleigh-wave group velocities

We use classic surface-wave tomography, which is based on the frequency-dependent wave velocity (dispersion) of surface waves (e.g., Stein & Wysession, 2003) to image seismic velocity structures in the study area. Because the estimated GFs are dominated by surface waves in the period range of 5s to 25s (Figs. 2.2 & 2.3), we can obtain seismic velocity information at crustal depths (e.g., Stein & Wysession, 2003). In this section, we describe how we measure and select the Rayleigh group dispersion curves that will be used for the inversion scheme.

We measure group velocities using the Multiple Filter Analysis (MFA), first introduced by Dziewonski et al. (1969). We isolate waves of certain periods from the Rayleigh wave train by bandpass-filtering the records with a narrow Gaussian filter around a center period. The maximum of the envelope of the resulting signal is picked as an estimate for the group arrival time of that center period. We perform these measurements on all four tensor components for 1953 station pairs, resulting in 7812 Rayleigh group-velocity dispersion curves.

To ensure that we use mainly high-quality fundamental mode measurements, we employ a set of selection criteria. This is necessary, because the picking algorithm itself does not discern between modes and does not check the quality of the measurements (see also Zigone et al., 2015). For each center period, we employ one station-based criterion and four component-based criteria:

- There must be at least two wavelengths of the measured wave between the stations ($\lambda = v_{\text{measured}} \cdot T$, with the period T). This ensures that the wave properly samples the medium.
- Measured velocities may not deviate strongly from the mean of all four components ($\pm 10\%$). We keep only components where the measured velocity does not exceed this threshold. This removes outliers and ensures that the measured velocities on the four components for a single station pair match, thereby avoiding measurements that are biased by noise sources.
- The energy of the arriving group must be greater than 1% of the maximum energy measured for that station pair for any period. We estimate the group energy as the peak amplitude of the envelope for a given center period. We set 1% of the highest measured group-energy for a given component across all center periods as the threshold. This removes poorly-constrained measurements due to very low arrival energy.
- The SNR of the filtered cross-correlation used to measure the group velocity must be greater than 4.
- Finally, the measurement on the ZZ component must be part of the final set of measurements for a given station pair. This acts as a weighting factor for vertical component measurements.

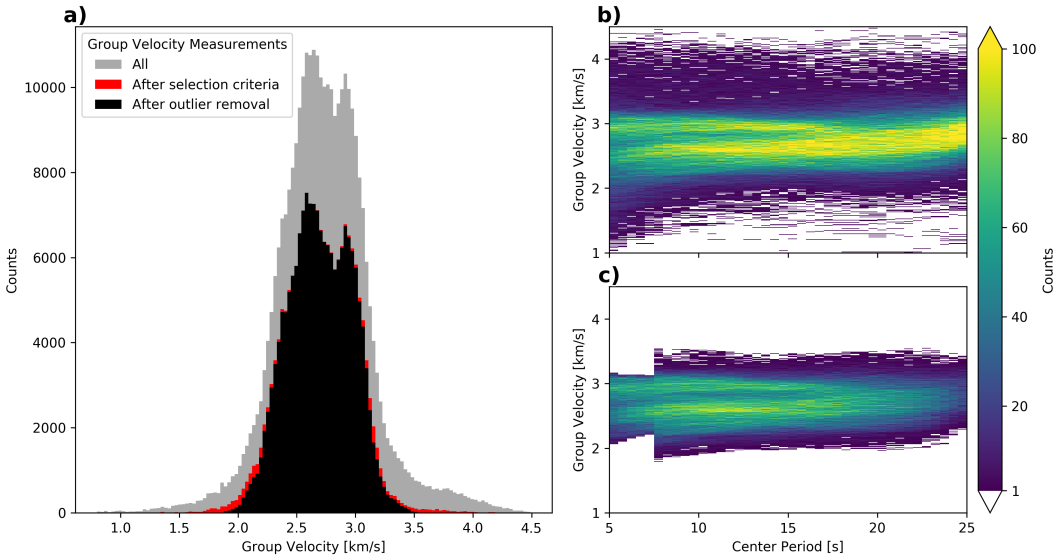


Figure 2.4: Distribution of measured group velocities and the effect of selection criteria and outlier removal. **a)** Histogram of all measured group velocities. 315,208 measurements were made in total (grey). 195,819 (62.1%) measurements remain after applying the selection criteria (red). 187,850 measurements (59.6%) remain after we remove outliers (black). **b)** Density plot of original set of group velocity measurements. **c)** Density plot of remaining group velocity measurements after selection criteria and outlier removal.

We found that the horizontal components are often less well-resolved, partly due to a large number of stations being temporary installations in sedimentary settings (see Section 2.3.2).

If at least 3 of the 4 components pass all the tests and ZZ is one of them, the mean velocity of these components for that station pair is preliminarily accepted as the inter-station group velocity of the given center period.

We limit the dispersion curves to the range of 5s to 25s. Below 5s the measurements are dominated by higher modes and we do not retain enough fundamental mode measurements. Above 25s the measurements are poorly-resolved and are mostly eliminated due to selection criteria.

The original data set consists of 315,208 group velocity-measurements (grey histogram in Fig. 2.4a and distribution in Figure 2.4b). Of those, the selection criteria remove 119,389 (37.9%) measurements leading to the red distribution in Figure 2.4a. The selection criteria successfully retain the slightly bimodal distribution characteristics, which represent the two distinct dispersion curve trends in the range of $5s \leq T \leq 17s$ (Fig. 2.4b), while eliminating most higher-mode measurements and low-velocity artifacts. We remove the remaining outliers, sometimes related

to higher modes by keeping only measurements within one standard deviation from the original set of all measurements (before selection criteria were employed) for $5\text{s} \leq T \leq 7\text{s}$, and within two standard deviations for $7.5\text{s} \leq T \leq 25\text{s}$ for each center period respectively. Lower periods are subject to a stricter threshold, because they are less reliable, more likely to be influenced by higher modes, and to stabilize the inversion results. This threshold eliminates an additional 7,969 (2.5%) measurements, mostly at the edges of the distribution. In total, we keep 187,850 (59.6%) (black histogram in Fig. 2.4a and distribution in 2.4c) of the initial 315,208 measurements.

The resulting averaged inter-station group velocities (see Section A.2) show a spatially coherent trend of faster velocities in the West and slower velocities in the East.

2.5 Group-velocity inversion

Combining all measurements of inter-station group velocities for a certain period allows to invert for the group velocities associated with regions (cells) instead of paths. We regionalize the measurements by following the inversion routine of Barmin et al. (2001) to obtain isotropic group-velocity maps.

The standard forward problem is posed in matrix notation $d = Gm$, where the data vector $d = t_m - t_{syn}$ consists of the travel-time differences between the measured travel times t_m and the synthetic travel times t_{syn} for a given initial model for each path. The matrix G contains the travel times for each path in each cell of the initial model. We choose cells that are 5km by 5km in size to balance lateral resolution with the number of measurements per cell and only invert cells with at least 3 crossing paths. This results in the group-velocity model $m = (u - u_0)/u_0$, with the initial group velocity u_0 and the group velocity after inversion u .

The inversion routine is based on the minimisation of a linear combination of data misfit, model smoothness $F(m)$, and convergence speed to the initial model for cells with few measurements $H(m)$

$$(G(m) - d)^T \cdot (G(m) - d) + \alpha^2 \|F(m)\|^2 + \beta^2 \|H(m)\|^2.$$

The model smoothness function $F(m)$ is a spatial Gaussian filter with the correlation length σ , given as

$$F(m) = m(r) - \int_S \exp\left(-\frac{|r - r'|^2}{2\sigma^2}\right) m(r') dr'.$$

The third term $H(m)$ describes a weighted norm of the model, which is effective for sparsely-sampled cells. It is given as an exponential function

$$H(m) = \exp(-\lambda\rho)m,$$

with the number of paths crossing the cell ρ and a weighting factor λ .

The inversion is controlled by a total of four regularization parameters. The factors σ and α control the model smoothness. λ and β control the weighted norm. Thanks to the favourable station distribution, path coverage is mostly even and the factors λ and β have only marginal impact on the inversion results (Fig. A.3). Therefore, we focus on determining proper model smoothness parameters.

2.5.1 Determination of regularization parameters

Usually, regularization parameters are chosen by a so-called L-curve analysis (e.g., Hansen & O'Leary, 1993; Stehly et al., 2009; Mordret et al., 2013a). In L-curve analysis, the inversion is performed for a set of chosen values for a single parameter, while the other parameters are fixed. The variance reductions (or a similar measure) for each inversion result are plotted versus that parameter and a value is picked near the maximum curvature of the resulting L-shaped curve. This analysis aims to give an objective measure of the trade-off between overfitting and under-representing the data. The choice of values for the fixed parameters is arbitrary at first. Additionally, the values of maximum curvature for each parameter are interdependent on the choice of the other parameters. An iterative process of alternating between fixed and varied parameters can help find proper values for the regularization parameters (Hansen & O'Leary, 1993).

Here, we propose a 2D L-curve analysis. Instead of fixing all parameters except one, we fix the parameters that have minimal influence on the inversion in our specific case (λ and β , see Section A.3). We vary σ and α simultaneously and retrieve a 2D surface of variance reduction in parameter space (Figure 2.5a). We plot one slice in each direction to illustrate the relationship to a standard L-curve analysis (right and bottom view of Figure 2.5a). Figure 2.5b shows the Gaussian curvature of that surface and slices at the same values for σ and α (right and bottom view). Negative values of curvature are set to 0, as they only appear as artifacts at the edges of the parameter space. This 2D L-curve analysis, similar to standard L-curve analysis, does not aim to give a final objective answer to the optimization problem at hand (over-fitting vs. under-representing data). It still requires subjective expert judgement for the final choice of regularization parameters, which is not ideal, but still widely used in seismic tomography. We pick the regularization parameters near the maximum of the surface curvature towards lower variance reduction to avoid overfitting

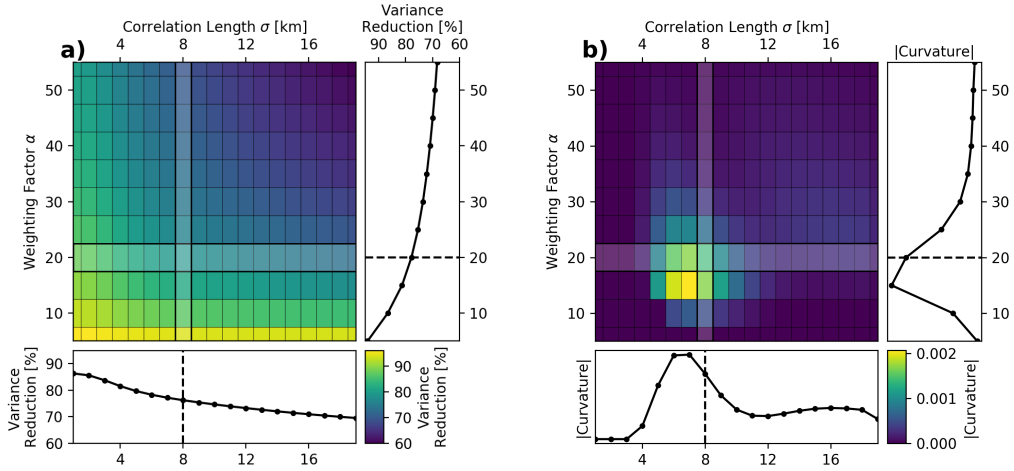


Figure 2.5: 2D L-curve analysis of the regularization parameters σ and α . **a)** The main view shows the 2D surface of variance reduction in parameter space. The right view represents the slice through that surface at $\sigma = 8\text{km}$. The bottom view represents the slice through the surface at $\alpha = 20$. **b)** The main view shows the Gaussian curvature of the 2D surface in a). The other views are slices through the curvature. The values for the regularization parameters are picked near the maximum curvature towards lower variance reduction ($\sigma = 8\text{km}$, $\alpha = 20$).

the data ($\sigma=8\text{km}$, $\alpha=20$).

2.5.2 Group-velocity resolution analysis

To interpret and further use the group-velocity maps, estimating their resolution is critical. First, we show path-density maps for selected center periods (Figure 2.6). In Figure 2.6a, we show the path density for 5s center period. We achieve an average ~ 20 paths per cell in the Western part of the study area. In the Eastern part, we lose measurements due to dispersion curve selection criteria, because higher mode measurements are more common for paths crossing sedimentary basins and the SNR of the horizontal components is lower for temporary stations in sedimentary settings. At 15s center period (Figure 2.6b), we observe an even distribution throughout the study region with around 25 paths per cell in most of the center area. We remove relatively few measurements at this period. In Figure 2.6c, we observe reduced path coverage averaging at ~ 15 paths per cell in the center region for 25s center period. Here, we mostly remove measurements due to the group-energy and inter-station distance thresholds.

Additionally, we present resolution-length maps for 15s period (Figure 2.7). We define the resolution length as the distance at which the value in the resolution matrix is decreased to half

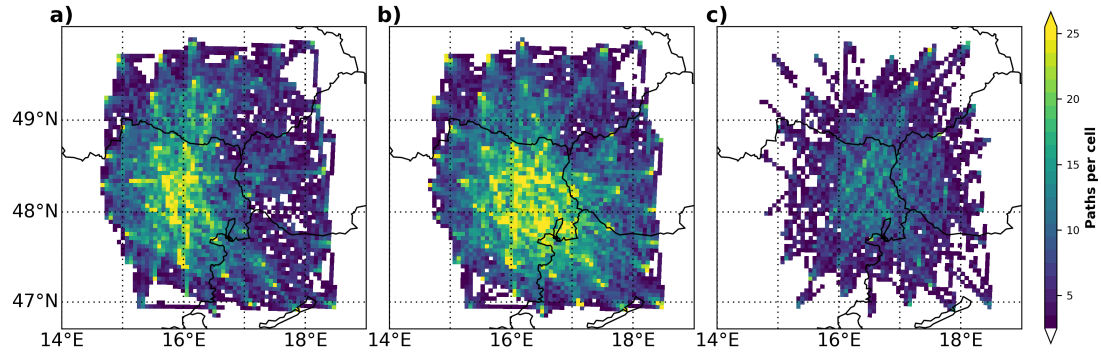


Figure 2.6: Path density for each cell for selected center periods. Cells with less than 3 crossing paths are white, because they are not inverted. **a)** At 5s center period, good path density (~ 20 paths per cell) in the Western part of the study area. Loss of density in the Eastern part of the map. **b)** At 15s center period, high density over the whole study area (~ 25 paths per cell). **c)** At 25s center period, even, although reduced, path coverage averaging around 15 paths per cell in the center region.

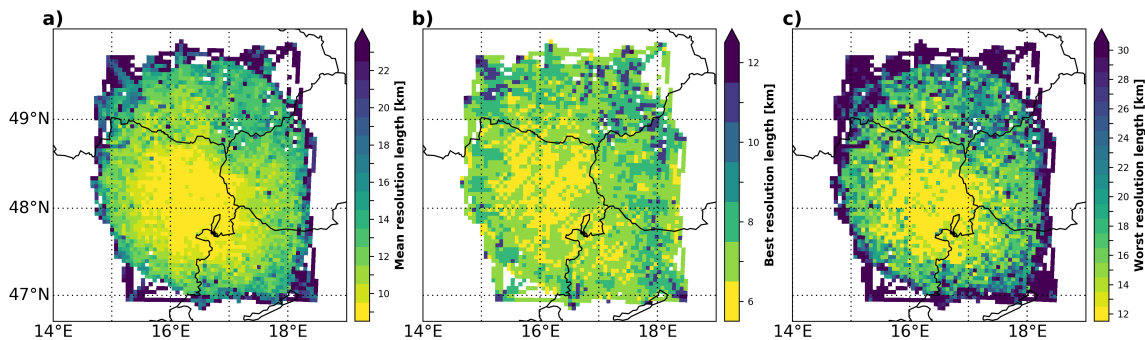


Figure 2.7: Resolution analysis of the group-velocity inversion for 15s center period. Mean resolution length (left) of the resolution matrix of each cell. Resolution length in the best direction (center), i.e. the best resolution length. Resolution length in the worst direction (right), i.e. the worst resolution length.

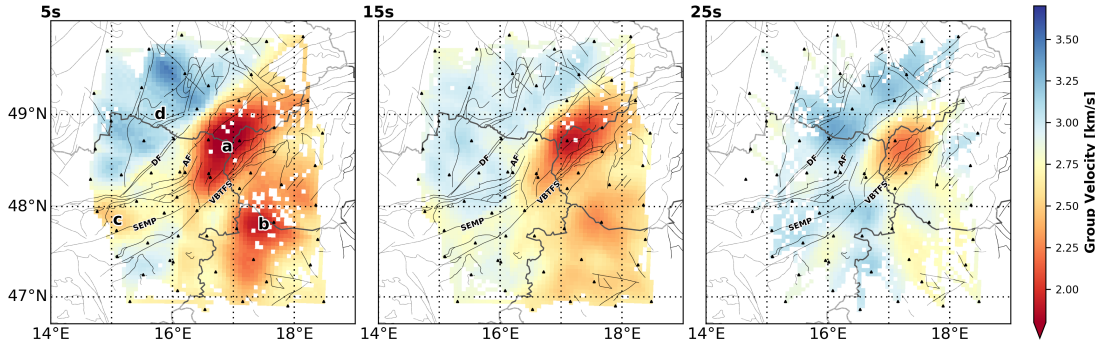


Figure 2.8: Group-velocity maps for 5s, 15s, and 25s center period. Major faults are plotted as black lines. We invert only cells with at least 3 crossing paths. Two separate major low-velocity bodies are visible from 5s to 15s: Vienna Basin (a) and Little Hungarian Plain (b). Only the Vienna Basin is clearly visible over the whole period range. At the Western edge, we image a less pronounced low-velocity feature (c). The North-Western parts of the study area show higher velocities, associated with the Bohemian Massif (d).

(Barmin et al., 2001; Stehly et al., 2009; Zgone et al., 2015). Because the spatial projection of the individual resolution matrices for each cell are not symmetric, a best and a worst direction exist. We show the mean correlation length (Figure 2.7a), the correlation length in the best direction (Figure 2.7b), and the correlation length in the worst direction (Figure 2.7c) for each cell. The mean resolution length is ~ 10 km in the center of the study area and ~ 20 km at the edges (Figure 2.7a). In the best direction (Figure 2.7b), we see correlation lengths of 6-10km for most of the study area. In the worst direction (Figure 2.7c), the correlation length still reaches 12km in the center, while dropping to 30km at the edges. Therefore, we can reliably interpret structures that span at least 3 cells (15km length) for most of the study area.

2.5.3 Group-velocity maps

We show our final group-velocity maps for 5s, 15s, and 25s center period (Figure 2.8). As major features, we observe two separate low-velocity structures in the Eastern part of the map and a more homogeneous high-velocity anomaly in the North-Western part of the map, which qualitatively match the velocity trends expected from topography (Figure 2.1). We identify the low-velocity bodies as the Vienna Basin in the center of the study area (a in Figure 2.8) and the Little Hungarian Plain in the SE (b in Figure 2.8). While the Vienna Basin is clearly visible over the whole period range from 5s to 25s, the Little Hungarian Plain fades away at 15s. The edge of the Vienna

Basin is marked well by the major known faults in the area (black lines in Figure 2.8). The Western edge of the Vienna Basin seems to move towards East with increasing center period. Additionally, we observe a smaller low-velocity anomaly at the Western edge of the study area (c in Figure 2.8), that seems to be bounded by the Alpine Front (AF) to the North and the Salzach-Ennstal-Mariazell-Puchberg fault (SEMP) to the South. The high-velocity anomaly at 5s center period in the North-Western part of the study area is identified as the Bohemian Massif (d in Figure 2.8). This anomaly is consistently observed at all available center periods.

2.6 Shear-velocity inversion

To gain insight into the depth extent of the observed velocity anomalies, we invert for shear-wave structure using the linearized inversion routine of Herrmann (2013). For each cell, we extract all available measurements from the group-velocity maps and combine them to construct new local 1D group-velocity dispersion curves. Each 1D curve is then inverted independently and recombined with the other cells to construct the 3D shear-velocity model.

Because the inversion scheme is linearized, the results may be heavily influenced by the initial model. It is therefore crucial to explore the dependence of the inversion results on the initial model and to choose a proper model. We tested several models, including global models like IASP91, models with constant velocity, and published regional models (Behm et al., 2016; Ren et al., 2013). First, we construct a mean model from Behm et al. (2016) by averaging the published 3D velocity model in the study area to retrieve a representative 1D model. From Ren et al. (2013) we extract a 1D velocity model located in the Vienna Basin (at 48.5°N, 17°E). To test these initial models (Figure 2.9a), we construct a representative dispersion curve by averaging all available 1D dispersion curves from our group-velocity maps (blue line in Figure 2.9b). In Figure 2.9 we show the results of inverting a variety of highly different initial models (blue lines in Figure 2.9a) in terms of resulting velocity models (black lines in Figure 2.9a) and their fitted dispersion curves (black lines in Figure 2.9b). We find that the velocities in the depth range of 5 - 20 km are only marginally influenced by the initial models. Therefore, the results in this depth range seem robust. We choose the mean model from Behm et al. (2016) as the initial model, because all reasonable models (i.e., not constant with depth) show similar results in this depth range and this model was derived near the study area. The model is made up of 42 layers, each 1km thick, with a half-space beneath. Shear velocities range from 3.1 km/s in the top layer to 4.2 km/s in the bottom layer, which is extended to the half-space. It does not contain discontinuities. Therefore, we can not find clear discontinuities at single layers in the final shear-velocity structure (Herrmann, 2013).

In Figure 2.9c we show the selected initial model (mean model from Behm et al. (2016)) and the resulting group-velocity depth sensitivity kernels (Figure 2.9d) for the measured period range in this

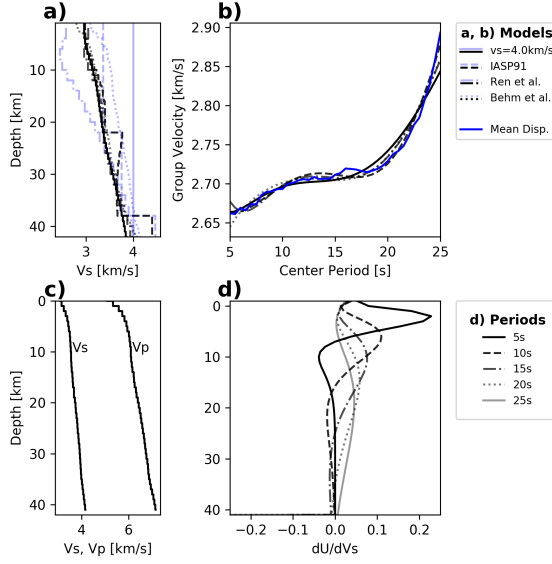


Figure 2.9: Shear-velocity inversion results for different 1D initial models **(a, b)** using the mean dispersion curve of all cells that are measured at least once, the chosen initial model **(c)**, and its group-velocity depth sensitivity kernels **(d)**. **a)** Initial models are marked as pale blue lines, inversion results as black lines. **b)** Fit of synthetic dispersion curves (black lines) to the mean dispersion curve (blue line). **c)** Chosen initial model: mean model from Behm et al. (2016). **d)** Group-velocity depth sensitivity for the range of available center periods ($5\text{s} \leq T \leq 25\text{s}$).

study. These kernels dictate the depth resolution of the shear-velocity inversion and give insight into the expected resolved depths. The period range in this study ($5\text{s} \leq T \leq 25\text{s}$) is sensitive to the top 30km (Figure 2.9d).

2.6.1 Shear-velocity depth resolution

The misfit statistics between the measured local 1D dispersion curves and synthetic dispersion curves, computed from the final inverted shear-velocity structure, are provided in Section A.4. The mean standard deviation of group-velocity misfit for all periods is 0.037 km/s with no single measurement deviating more than 0.21km/s. This illustrates a good match between synthetic and observed dispersion curves.

We normalize the resolution matrix of each individual cell and average all of them to compute the average normalized resolution matrix of all cells (Figure 2.10). This resolution matrix contains the weights of the linear relationship in which each solution parameter is derived from the weighted averages of nearby true-model parameters (e.g., An, 2012). This resolution matrix is useful to

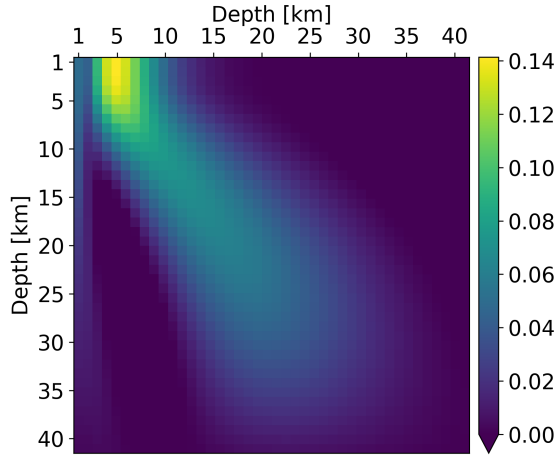


Figure 2.10: Resolution matrix of the final shear-velocity model. Resolved shear velocities at depths 1-4km are dominated by the shear velocities at depth 3-8km. Good resolution (roughly symmetric matrix) from 4km to 20km depth. Loss of proper resolution at greater depths.

measure the solution obtainability for each layer - giving insight into the resolved depths - along with the quality of the inversion based on the degree to which the matrix approximates the identity matrix. The depths in which we achieve good resolution are controlled by the available group-velocity measurements. As previously noted, they are limited mainly by higher modes at shorter periods and poor-quality measurements at longer periods. We find good resolution in depths of 4km to 20km, indicated by a roughly symmetric resolution matrix in this depth range. At shallower depths our model is likely to overestimate velocities, because they are heavily influenced by the higher velocities at depths around 5km. At greater depths our model is likely to underestimate velocities somewhat, and low-velocity zones may blur into these greater depths.

2.6.2 3D shear-velocity model

2.6.2.1 Shear-velocity maps In Figure 2.11 we show selected depth slices of our final 3D shear-velocity model. We provide the model online as electronic Supplementary Material. The maps display the same major features as the group-velocity maps (Figure 2.8): Vienna Basin (a in Figure 2.11), Little Hungarian Plain (b in Figure 2.11), and Bohemian Massif (e in Figure 2.11). These maps allow to interpret the depth extent of the observed velocity structures.

The Vienna Basin is imaged as a low velocity feature with a lateral extent of ~ 80 km across and ~ 150 km along the SW-NE-strike of the major faults in the region at 4km depth (a in Figure 2.11). The NW edge of the Vienna Basin and transition to the Bohemian Massif is well-delineated by

the Alpine Front (AF). The SE edge is marked by the Southern part of the complex Vienna Basin transfer fault system (VBTFS), which delimits the end of the Vienna Basin towards the Leitha Mountains, Little Carpathians, and Little Hungarian Plain. The lowest shear velocities we observe are located just North of the border triangle of Austria, Czech Republic, and Slovakia with 2.14km/s. At 8km depth, the SW Vienna Basin is no longer imaged, while the NE part is still clearly mapped. The NE part still shows the lowest velocities in the model at that depth, but the location of the minimum is just East of the border triangle. The NW edge of the basin is no longer delineated as clearly by the surface expression of the AF, the edge shifts ~8km towards SE. The SE edge, on the other hand, still seems to be marked quite well by the VBTFS. At 12km depth, the low-velocity body has shifted further towards East with the AF being no longer associated with the NW edge of the Vienna Basin. Still, the VBTFS delimits the SE edge of the Vienna Basin. At 16km depth, the NW edge of the Vienna Basin is still dipping further towards East, while the SE edge does not move. At 20-24km, there is a low-velocity anomaly remaining, no longer defined by the lowest velocities for these depths, but instead it shows comparable velocities to other low-velocity features in the study area.

The Little Hungarian Plain is imaged as a low-velocity feature with an extent of ~250km along SW-NE and ~120km across from the Southern edge of this model to the Eastern edge at 4km depth (b in Figure 2.11). The lowest velocity is found in the center of the Little Hungarian Plain with 2.36 km/s. To the NW, the Little Hungarian Plain is limited by the Little Carpathians and the Leitha Mountains. To the SE, the Little Hungarian Plain transitions into the Bakony mountain range, which we image with higher velocities (c in Figure 2.11). At around 12km depth, the low velocities beneath the Little Hungarian Plain seem to connect to the low velocities beneath the Bakony. At greater depths (16km - 24km), there is no clear low-velocity feature remaining that we would associate with the Little Hungarian Plain.

The Eastern edge of the Northern Calcareous Alps (d in Figure 2.11) is imaged as a shallow low-velocity feature, visible at 4-8km. It is located between the Alpine Front (AF) to the North and the Salzach-Ennstal-Mariazell-Puchberg fault (SEMP) to the South.

The Bohemian Massif in the NW is represented as widespread high-velocity feature (e in Figure 2.11). The SE edge of the Bohemian Massif is marked by the Diendorf Fault (DF) to the Molasse basin in the South at 4km depth. As the Molasse basin becomes narrower towards East, the edge of the Bohemian Massif lies closer to the AF. At shallow depths (4-8km), the Bohemian Massif is seen as a relatively homogeneous high-velocity feature, which becomes more complex towards greater depths. At 16-24km depth, an elongated, ~40km wide high velocity body is visible, which approximately follows the surface expression of the AF (f in Figure 2.11). Beneath the Bohemian Massif, slightly reduced velocities are visible at these greater depths.

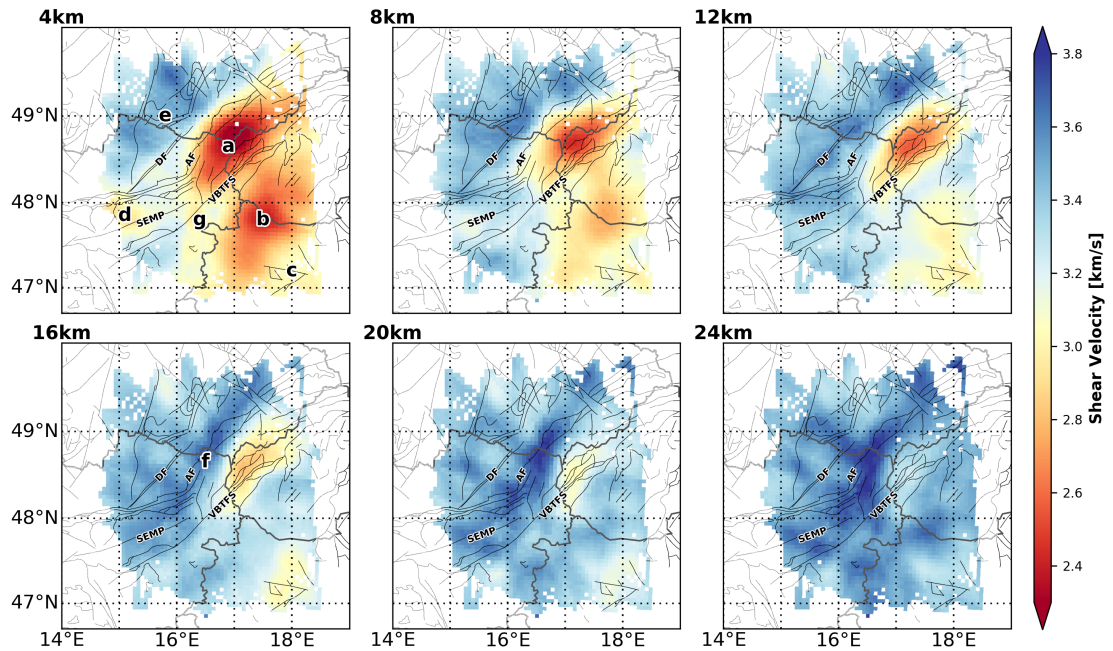


Figure 2.11: Depth slices of the final shear-velocity model at 4km, 8km, 12km, 16km, 20km, and 24km depth. Major faults are plotted as black lines. Two low-velocity bodies are observed in the Eastern part of the study area: Vienna Basin (a) and Little Hungarian Plain (b). The low-velocity signature of the Vienna Basin is well-visible up to depths of 20km, while the Little Hungarian Plain fades out at around 16km. The Little Hungarian Plain is limited towards South-East by the Bakony mountain range (c). The Northern Calcareous Alps are imaged as a shallow low-velocity anomaly (d). Higher velocities in the North-Western parts of the area are associated with the Bohemian Massif (e). At greater depths, a high-velocity feature seems to follow the surface expression of the Alpine Front (f).

2.6.2.2 Shear-velocity profiles In Figure 2.12 we show four depth profiles cutting through the final shear-velocity model. Three profiles are crossing the major structures in our study area at different latitudes (A, B, C in Figure 2.12a). Profile D is aligned SW-NE along the strike of the major faults in the region. On the map view (Figure 2.12a), we mark the locations of known boreholes (Wessely, 2006; Brix & Schultz, 1993) that have reached the crystalline basement (∇) and some that have not (\circ). Boreholes are plotted at those depths at which they reached the crystalline basement (∇) or the depth at which they were terminated (\circ), if they did not reach the basement. We will discuss the boreholes along with other additional observations in section 2.7. In the profiles (Figure 2.12), main features are labelled with abbreviations at the top, and intersection points with major faults are marked as bold vertical lines.

In profile A (Figure 2.12), we see the Bohemian Massif dipping mildly ($\sim 20^\circ$) towards SE below the Vienna Basin. The low-velocity signature of the Vienna Basin is visible up to depths of 10km in the NW (at 80km distance) and up to 20km in the SE (at 130km distance). The low-velocity anomaly under the Little Hungarian Plain (at 200km distance), on the other hand, is only visible at shallower depths up to 8km. The two sedimentary basins are separated in the profile at the Little Carpathians (at 140km distance), which aligns with the end of the SE extent of very low velocities below 2.3km/s.

In profile B (Figure 2.12), the same major structures are visible. The Bohemian Massif is dipping below the Vienna Basin with a dip angle of $\sim 20^\circ$. The deep low velocities around 15km depth beneath the Vienna Basin are generally higher than those seen in profile A ($v_s \sim 3.0\text{km/s}$ vs. $v_s \sim 2.7\text{km/s}$). The SE edge of this low-velocity anomaly aligns with the SE edge of the Little Carpathians. The Little Hungarian Plain shows low velocities ($v_s \leq 3.0\text{km/s}$) up to 12km depth.

In Profile C (Figure 2.12), the low velocities of the Vienna Basin can be seen only at shallow depths of less than 5km. No low-velocity feature at greater depths beneath the Vienna Basin is visible. Here, we image the expected lower sedimentary thickness of the SW Vienna Basin, compared to the NE Vienna Basin (Wessely, 2006). The transition from the Vienna Basin to the Little Hungarian Plain in the velocity model aligns with the Leitha Mountains. Between the Bohemian Massif and Vienna Basin, we see very shallow ($\leq 3\text{km}$) low velocities, which seem to be associated with the Molasse basin. Note that low velocities do not show up in the near-surface crystalline structure of the Bohemian Massif. The Bohemian Massif itself is harder to follow dipping towards SE and to separate from the overlying structures compared to profiles A and B (Figure 2.12).

Finally, in Profile D (Figure 2.12), we show a cross-section along the strike of the major faults from the Northern Calcareous Alps in the SW to the Western Carpathians in the NE. The Northern Calcareous Alps show very shallow low velocities, similar in depth extent and magnitude to the Molasse basin (see Profile C). The Vienna Basin, NE of the Northern Calcareous Alps, is dipping

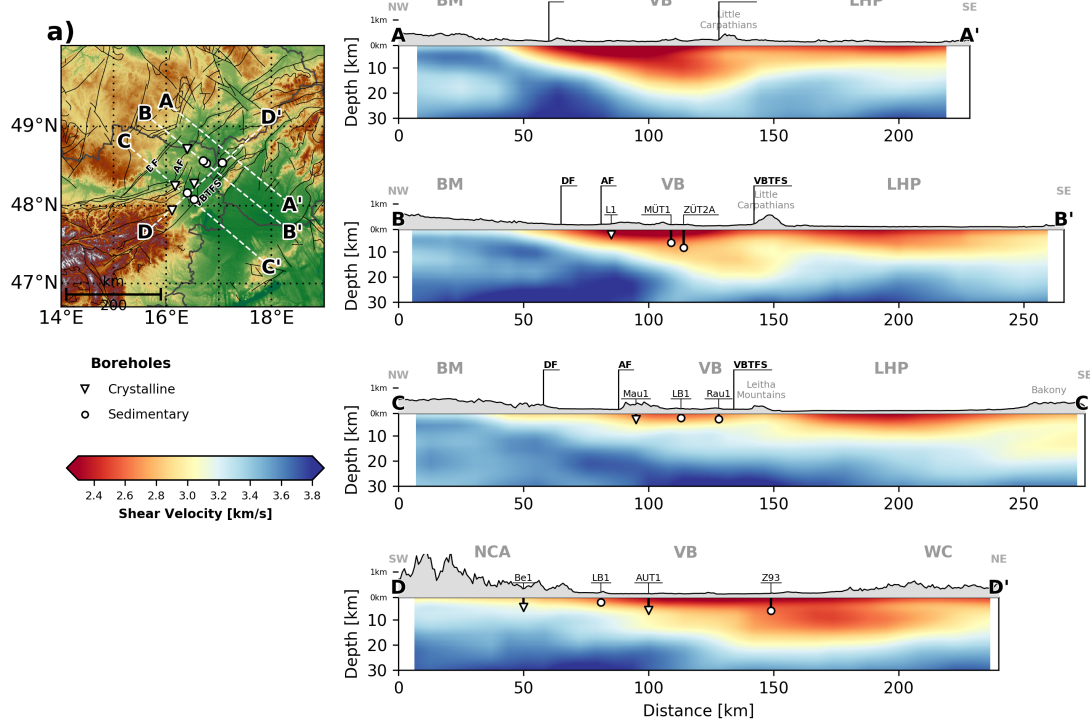


Figure 2.12: **a)** Map view of the study area with the locations of boreholes shown in the four depth profiles. ∇ marks boreholes that have reached the crystalline basement, \circ marks boreholes that have not. **Profiles A-D**) Depth profiles crossing the main geological structures in the study area (A-C) and one profile along the strike of the Vienna Basin transform fault system (D). Major geological features are labelled with abbreviations: Bohemian Massif (BM), Vienna Basin (VB), Little Hungarian Plain (LHP), Northern Calcareous Alps (NCA), Western Carpathians (WC). The sedimentary basins (VB, LHP) exhibit low velocities, while the basement rock in the BM is marked by high velocities. Boreholes are marked as vertical lines with symbols marking the crystalline basement depth (∇) or the termination depths (\circ). Intersections with major faults (DF, AF, VBTFS) are marked with bold vertical lines

very mildly ($\sim 10^\circ$) towards NE until 130km - 140km distance. There, we see a steep increase of the low-velocity feature towards greater depths ($\sim 20\text{km}$), which is prevalent towards NE into the Western Carpathians. From 200km to 230km distance, we see the velocities of this feature increase from $v_s \sim 2.7\text{km/s}$ to $v_s \sim 3.0\text{km/s}$ at $\sim 10\text{km}$ depth.

2.7 Discussion

The new 3D shear-wave velocity model we present in this study correlates with several previously-mentioned geological features. For discussion, we will compare our results with previous seismological studies (Tomek & Hall, 1993; Behm et al., 2007, 2016; Ren et al., 2013; Hrubcová & Šroda, 2015), as well as ground truth from borehole data (Wessely, 2006; Brix & Schultz, 1993, and Figure 2.12), and with gravity field measurements (Bonvalot et al., 2012). We will not try to interpret the tectonic evolution of the Vienna Basin, surrounding region, and underlying structures in detail, and wave the new insights provided by this model to be assessed by more qualified colleagues. In the following, we will interpret the bottom of the observed low-velocity features though, as the interface between sedimentary rocks and crystalline basement.

2.7.1 Vienna Basin

We map the Vienna Basin as a low-velocity feature, 80 by 150 km in size near the surface at 4km depth (a in Figure 2.11). Its lateral extent is well-delimited by known major faults in the area: Towards SE, the Southern parts of the complex Vienna Basin transfer fault system (VBTFS) mark the edge towards the Leitha Mountains and Little Carpathians, while the Alpine Front (AF) coincides with the transition between Vienna Basin and Molasse Basin to the NW (Figures 2.1a, 2.12a, 2.13a). It matches the lateral extent expected from surface geology (Figure 2.13a) and is mapped as a trough with $\sim 50\text{mGal}$ in the Bouguer anomaly (a in Figure 2.13b), which can be explained by shallow low-density rocks.

Other seismological studies also find low velocities in the area from P-wave wide-angle and refraction seismics (Behm et al., 2007; Hrubcová et al., 2005; Tomek & Hall, 1993), ambient-noise tomography using data of the Southern Carpathian Project and Carpathian Basins Project (Ren et al., 2013), and ambient-noise tomography using data of the ALPASS project (Behm et al., 2016). Behm et al. (2007) map the Vienna Basin as a (P-wave) low-velocity feature, which is not clearly separated from the Little Hungarian Plain. They use a grid spacing of 20km for the regionalization of Pg phase picks. Ren et al. (2013) also image the Vienna Basin as a low-velocity anomaly, the lateral extent roughly matching our model. They use a 0.2° by 0.2° grid to regionalize the data and properly resolve structures as small as 60km in lateral extent. The model of Behm et al. (2016) is

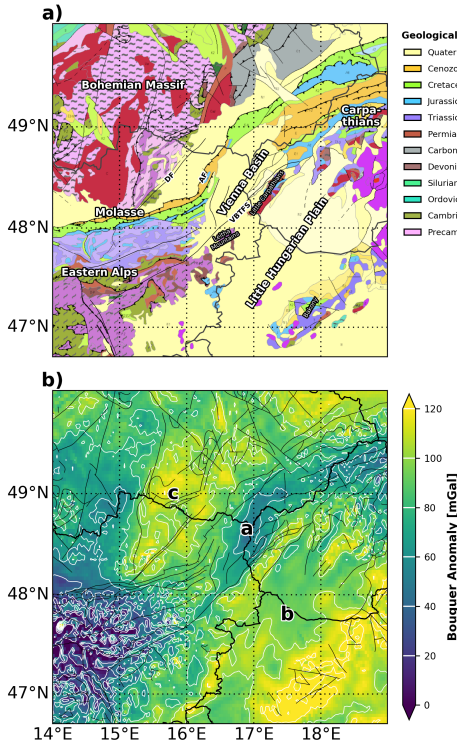


Figure 2.13: **a)** Surface geology of the study area extracted from the International Geological Map of Europe (IGME5000, Aschk, 2005). Major features are labelled. Shown faults (black lines) are combined from the IGME5000 and the EDSF (Basili et al., 2013). **b)** Bouguer gravity anomaly in the study area, extracted from the World Gravity Map 2012 (WGM2012, Bonvalot et al., 2012). Labelled features: Vienna Basin (a), Little Hungarian Plain (b), Bohemian Massif (c).

limited with respect to the station distribution, especially towards the NE parts of our study area and cannot map the lateral extent of the low velocities in the Vienna Basin.

Our model improves the lateral resolution of seismic velocities in the Vienna Basin and surrounding region greatly. The mean resolution length is \sim 15km for most of the study area in a grid with 5x5km cells, roughly increasing the resolution by a factor of 4 compared to previous studies (Behm et al., 2007; Ren et al., 2013; Behm et al., 2016). This assessment is further supported by our ability to image the Southern Vienna Basin at 4km depth (g in Figure 2.11), which we find to be a \sim 20km wide structure at this depth, matching geological interpretations (Wessely, 2006).

The improved resolution of our model also allows us to image and interpret the deeper structure (10-20km) of the Vienna Basin and surrounding region with greater precision than previously

possible. The SE Vienna Basin appears as a shallow low-velocity feature with depths of up to \sim 5km, matching ground truth from boreholes Laer Berg 1 (LB1 in Figure 2.12 profiles C, D) and Rauchenwarth 1 (Rau1 in Figure 2.12, profile C). Towards NE, the Vienna Basin bottom dips mildly down to \sim 10km depth before a steeper drop is visible in the velocity model NE of borehole Aderklaa Ultratief 1 (AUT1 in Figure 2.12, profile D), down to depths of \sim 15-20km. The low velocities at these depths are consistently observed in the NE Vienna Basin and Western Carpathians (Figure 2.12, profile D). The reflection profile 8HR (Tomek & Hall, 1993) crosses from the SE edge of the Bohemian Massif into the Western Carpathians. It images a SE dipping reflector that is clearly visible down to depths \sim 10km below the Vienna Basin. Further towards SE, where we find a low-velocity anomaly at greater depths, the profile is less conclusive. Here, Ren et al. (2013) find low velocities beneath the Vienna Basin in depths of up to \sim 16km, matching our observations. The refraction profile CEL09 (Hrubcová et al., 2005) of the CELEBRATION2000 project (Guterch et al., 2003) crosses the study area \sim 50km South of the deep low-velocity anomaly in our model and reveals the same SE-dipping interface. They find low P-wave velocities up to depths of 8km just below the central Vienna Basin, consistent with our model.

The available data from most boreholes match well with the shear velocities in our model (Figure 2.12). When a borehole reaches the crystalline basement, our model generally transitions from $v_s \leq 2.9$ km/s to higher velocities at similar depths ($\pm \sim 2$ km). This is illustrated by the boreholes Laa 1 (L1 in Figure 2.12, profile B), Mauerbach 1 (Mau1 in Figure 2.12, profile C), and Aderklaa Ultratief 1 (AUT1 in Figure 2.12, profile D), which have reached the crystalline basement at varying depths.

In the NE Vienna Basin, no boreholes have reached the crystalline basement. This matches our model, which shows low shear velocities at the locations and termination depths of boreholes Maustrenk Übertief 1, Zistersdorf Übertief 2A (MÜT1 and ZÜT2A in Figure 2.12, profile B), and Zavod 93 (Z93 in Figure 2.12, profile D) (Wessely, 2006). While the crystalline basement is expected \sim 1km below the termination depths of MÜT1 and ZÜT2A, the crystalline basement below Z93 is expected well below 10km (Wessely, 2006). Our model corroborates this and the transition to velocities ≥ 2.9 km/s with depth (Figure 2.12, profile B, D) seems to mark the expected crystalline basement depths quite well. Therefore, our model suggests a very deep crystalline basement around 20km depth at borehole Z93 (profile D in Figure 2.12). We are aware of only few other works exploring these depths below the NE Vienna Basin, namely the tomography presented by Ren et al. (2013), which lacks the resolution to give better information on the depth extent of these observed features, and reflection profile 8HR presented in Tomek & Hall (1993), which is not clearly imaging any interfaces at these depths in the specific area. Additionally, Wessely (2006) interpret the sedimentary rocks underlying the Vienna Basin to extend to increasing depths towards NE, matching our observations, but their interpretations do not extend deeper than \sim 10km.

Notably, our model does not correlate well with the ground truth from borehole Berndorf 1 (Be1 in Figure 2.12, profile D). It is located at the edge of the Southern Vienna Basin and reaches the basement at a depth of 5-6km (Brix & Schultz, 1993). Our model shows shear velocities \geq 2.9km/s already at 2km depth. This apparent mismatch may be explained by the location of this borehole in the complex transition zone between the horizontally layered sedimentary basin and the hard rock of the Alpine orogen, illustrating the limitations of our methodology. The inversion routine is based on fitting dispersion curves computed in 1D layered media. This assumption is less valid in complex, deformed rheology. Still, this approximation seems valid inside the Vienna Basin, supported by the ground truth from boreholes located within the basin.

These observations, combined with the depth resolution analysis (Section 2.6.1, Figure 2.10) give us confidence that we properly resolve the Vienna Basin and its underlying structure in 4-20km depth. Thus, the deep low-velocity anomaly beneath the NE Vienna Basin (Figures 2.11, 2.12) does not appear to be an artifact introduced during Green's Function retrieval, dispersion curve measurements, or the inversion scheme and thus probably represents a true geological feature. It is unlikely to be caused by smearing of low velocities from shallow to greater depths during the inversion, because the deep low-velocity anomaly is not directly beneath the strongest shallow anomaly, but shifted by \sim 25km towards SE.

While the observed near-surface velocities (in the top 4km) correlate with expectation from surface geology, the shear velocities at these depths may not necessarily be properly-resolved. Our depth resolution analysis (Figure 2.10) suggests that these shallow velocities are dominated by the shear velocities at around 5km depth. Therefore, shallow velocities in our model are likely overestimated, given that seismic velocities generally increase with depth.

2.7.2 Little Hungarian Plain and Bohemian Massif

The Little Hungarian Plain is the second major low-velocity feature in our model. At 4km depth it spans from the Southern to the Western edge of our model (Figure 2.11). Towards SE it is limited by the Bakony mountain range geologically (Figure 2.13a), which correlates with higher velocities in the shallow crust at the SE edge of our model. Towards NW the Little Hungarian Plain ends at the Leitha Mountains and Little Carpathians geologically (Figure 2.13a), which our model represents well by velocity contrasts towards higher velocities, not unlike that seen under the Bakony mountain range. The center of the LHP is marked by velocities as low as 2.43km/s. The lateral extent we find in shallow depths coincides well with the model of Ren et al. (2013).

The shape of the strongest low-velocity anomaly in the Little Hungarian Plain at 4km depth fits particularly well with the Bouguer gravity anomaly (b in Figure 2.13b). Because decreased Bouguer anomalies can be associated with low density rocks (e.g., sedimentary rocks), this obser-

vation corroborates our lateral resolution estimation (Section 2.5.2, Figure 2.7).

We image the low velocities of the Little Hungarian Plain as deep as 10km. It is deeper than the SE Vienna Basin (Figure 2.12, profile C), but not as deep as the NE Vienna Basin and its underlying structures, which we image up to 20km depth (Figure 2.12, profile D). Other authors (e.g., Ren et al., 2013) report similar depths of this low-velocity feature.

We map the SE edge of the Bohemian Massif at the NW edge of our model. It is characterized by a relatively homogeneous high-velocity anomaly at shallow depths (Figure 2.11). Towards SE we observe a velocity contrast from 3.5km/s to 3.2km/s near the Diendorf Fault (DF) and a very high gradient - from 3.5km/s to 2.8km/s over ~20km - further towards NE, where the Molasse basin is very narrow (Figures 2.1a, 2.12a, 2.13a). With depth (e.g., at 20km, Figure 2.11), the Bohemian Massif exposes more complex velocity variations in the range of 3.0km/s to 3.5km/s. Beneath the high velocity top ($v_s \sim 3.5$ km/s) of the Bohemian Massif, lower velocities are visible ($v_s \sim 3.2$ km/s, Figure 2.12, profiles A-C). The high-velocity feature along the surface expression of the Alpine Front (AF) at depths 16-24km (Figure 2.11) seems to align with the top of the BM, dipping below the Vienna Basin (Figure 2.12, profiles A-C).

The Bohemian Massif is well-mapped in the Bouguer-gravity anomaly map (c in Figure 2.13b) as a positive anomaly relative to the surrounding region. We interpret this as the presence of high-density rocks (e.g., crystalline basement), which we image as high velocities. The lateral extent of the low velocities in our model and the higher gravity anomaly in the Bohemian Massif correlates well (Figures 2.11, 2.13).

Overall, we resolve the crustal structure of the Vienna Basin and surrounding region with previously unachieved resolution. Our model is consistent with and improves upon previous seismological studies (Tomek & Hall, 1993; Hrubcová et al., 2005; Behm et al., 2007; Ren et al., 2013; Behm et al., 2016), Bouguer gravity anomalies studies (Bonvalot et al., 2012), represents well-known surface geology (Aschk, 2005), and matches ground truth from most boreholes in the region (Wessely, 2006; Brix & Schultz, 1993).

Our model may be used in the future for several further studies. In seismological applications, the model can be utilized to improve regional wave propagation modeling, as well as the location accuracy of local and regional seismicity by accounting for local and regional heterogeneities affecting wave propagation. Geology and tectonics may profit from our model to gain new insight into the deeper crustal structure beneath the Vienna Basin and surrounding regions. These insights may help to better understand the complex tectonic evolution of the Vienna Basin and Alpine-Carpathian transition zone.

There is potential to further increase the resolution and accuracy of seismic velocities in the region through several means. The station density could be improved further, which would allow

even better resolution, either in the whole region or locally with dense seismic arrays (e.g., Nakata et al., 2016; Ben-Zion et al., 2015). The Alpine-Carpathian transition zone has been subject to several seismic studies, which generated plenty of non-simultaneous continuous seismic recordings. These could be utilized using the C3 technique (Stehly et al., 2008), which allows to compute estimated Green's Functions from non-simultaneous records (Spica et al., 2016). Apart from data, there are also opportunities to improve the results by discerning between and incorporating several surface-wave modes (especially at short periods), by measuring phase velocities in addition to group velocities, and by incorporating Love waves and jointly inverting Love and Rayleigh waves to derive an anisotropic velocity model.

2.8 Conclusions

We computed a detailed 3D shear-velocity model of the crust in the Vienna Basin and surrounding region using ambient-noise tomography. It complements previously released studies, imaging the wider Vienna Basin region (Behm et al., 2007; Ren et al., 2013; Behm et al., 2016). The model provides new insight into the deep structures of the Vienna Basin and surrounding regions by achieving better resolution thanks to the favourable station distribution of the AlpArray project seismic network (AlpArray Seismic Network, 2015). The main outcome of this study is:

- We image the main geological structures in the study area clearly, the Vienna Basin, the Bohemian Massif, and the Little Hungarian Plain (Figure 2.11). Their lateral extents match well with known geological features, i.e., faults marking the transition between features, such as the Diendorf Fault (DF), the Alpine Front (AF), and the Vienna Basin transfer fault system (VBTFS) (Figures 2.1, 2.13). We find prominent velocity contrasts near the surface expressions of those faults, which are expected due to the change of lithology between different geological units.
- Additional insight into the deep crustal structure (10-20km) of the wider Vienna Basin region (Figures 2.11, 2.12). We image the Northern Vienna Basin and underlying features up to depths of \sim 20km. A shear-velocity contrast with depth (from \sim 2.8km/s to \sim 3.2km/s) is visible near the expected depth of the crystalline basement for most locations, where borehole data are available (\pm 2km). The Bohemian Massif dips below the Vienna Basin towards South-East at an angle of \sim 10°. Additionally, the Vienna Basin dips towards North-East, mildly at first and then with a steeper slope (\sim 20°) to the greater depths observed.
- The model we provide has a previously unachieved lateral resolution of \sim 15km for most of the study area. This improves on previous work in the area (Behm et al., 2007; Ren et al., 2013; Behm et al., 2016).

Acknowledgments

The authors thank P. Strauss and W. Thöny from OMV for very insightful discussions regarding the expected depth extent of geological features in the study area. We also thank the two reviewers (Aurélien Mordret and Anonymous) for the useful comments and suggestions, which helped improve the manuscript. The data used in this study are provided by the operators of the national seismic networks (Austrian Seismic Network, 1987; Hungarian National Seismological Network, 1992; National Network of Seismic Stations of Slovakia, 2004; Czech Regional Seismic Network, 1973) and the members of the AlpArray Working Group (AlpArray Seismic Network, 2015). We thank the AlpArray Seismic Network Team: György HETÉNYI, Rafael ABREU, Ivo ALLEGRETTI, Maria-Theresia APOLONER, Coralie AUBERT, Simon BESANÇON, Maxime BÉS DE BERC, Götz BOKELMANN, Didier BRUNEL, Marco CAPELLO, Martina ČARMAN, Adriano CAVALIERE, Jérôme CHÉZE, Claudio CHIARABBA, John CLINTON, Glenn COUGOULAT, Wayne C. CRAWFORD, Luigia CRISTIANO, Tibor CZIFRA, Ezio D'ALEMA, Stefania DANESI, Romuald DANIEL, Anke DANNOWSKI, Iva DASOVIĆ, Anne DESCHAMPS, Jean-Xavier DESSA, Cécile DOUBRE, Sven EGDORF, ETHZ-SED Electronics Lab, Tomislav FIKET, Kasper FISCHER, Wolfgang FRIEDERICH, Florian FUCHS, Sigward FUNKE, Domenico GIARDINI, Aladino GOVONI, Zoltán GRÁCZER, Gidera GRÖSCHL, Stefan HEIMERS, Ben HEIT, Davorka HERAK, Marijan HERAK, Johann HUBER, Dejan JARIĆ, Petr JEDLIČKA, Yan JIA, Hélène JUND, Edi KISSLING, Stefan KLINGEN, Bernhard KLOTZ, Petr KOLÍNSKÝ, Heidrun KOPP, Michael KORN, Josef KOTEK, Lothar KÜHNE, Krešo KUK, Dietrich LANGE, Jürgen LOOS, Sara LOVATI, Deny MALENGROS, Lucia MARGHERITI, Christophe MARON, Xavier MARTIN, Marco MASSA, Francesco MAZZARINI, Thomas MEIER, Laurent MÉTRAL, Irene MOLINARI, Milena MORETTI, Helena MUNZAROVÁ, Anna NARDI, Jurij PAHOR, Anne PAUL, Catherine PÉQUEGNAT, Daniel PETERSEN, Damiano PESARESI, Davide PICCININI, Claudia PIROMALLO, Thomas PLENEFISCH, Jaroslava PLOMEROVÁ, Silvia PONDRELLI, Snježan PREVOLNIK, Roman RACINE, Marc RÉGNIER, Miriam REISS, Joachim RITTER, Georg RÜMPKER, Simone SALIMBENI, Marco SANTULIN, Werner SCHERER, Sven SCHIPPKUS, Detlef SCHULTE-KORTNACK, Vesna ŠIPKA, Stefano SOLARINO, Daniele SPALAROSSA, Kathrin SPIEKER, Josip STIPČEVIĆ, Angelo STROLLO, Bálint SÜLE, Gyöngyvér SZANYI, Eszter SZŰCS, Christine THOMAS, Martin THORWART, Frederik TILMANN, Stefan UEDING, Massimiliano VALLOCCHIA, Luděk VECSEY, René VOIGT, Joachim WASSERMANN, Zoltán WÉBER, Christian WEIDLE, Viktor WESZTERGOM, Gauthier WEYLAND, Stefan WIEMER, Felix WOLF, David WOLYNIEC, Thomas ZIEKE, Mladen ŽIVČIĆ. Data were acquired using the ORFEUS web services. The software used in this study was kindly provided by Beyreuther et al. (2010) and Herrmann (2013). Part of this work was performed using funding from the Austrian Science Fund (FWF): project number 26391. The authors also thank the COST ACTION ES1401: Time-DEpendent Seismology (TIDES) for funding a Short-Term Scientific Mission (STSM 35662), which funded an exchange visit for this project. The authors also thank the Austrian Agency for International Cooperation in Education & Research (OeAD-GmbH) for funding the Amadée project FR02/2017, which helped directly facilitate work on this project. This project was co-funded by the French Europe & Foreign Affair ministry and the French Higher Education and Research ministry under the project number PHC-AMADEUS 38147QH. D. Zigone thanks IPGS for its support in this work through the 2016 IPGS-internal call.

3 The Alland earthquake sequence in Eastern Austria

This section has been submitted to the Austrian Journal of Earth Sciences on 13.08.2019 as:

Schippkus, S., Hausmann, H., Duputel, Z., Bokelmann, G., the AlpArray Working Group. The Alland earthquake sequence in Eastern Austria: Shedding Light on Tectonic Stress Geometry in a Key Area for Seismic Hazard.

Abstract

We present our results on the fault geometry of the Alland earthquake sequence in Eastern Austria (Eastern Alps) and discuss its implications for the regional stress regime, and active tectonics. The series contains 71 known events with local magnitudes $0.1 \leq M_L \leq 4.2$. We locate the earthquakes in a regional 3D velocity model to find absolute locations. These locations are then refined by relocating all events relative to each other using a double-difference approach, based on relative travel times measured from waveform cross-correlation and catalogue data. We also invert for the moment tensor of the $M_L = 4.2$ mainshock by fitting synthetic waveforms to the measured seismograms using a combination of the L1- and L2-norms of the waveform differences. Direct comparison of waveforms of the largest events in the sequence suggests that all of them ruptured with very similar mechanisms. We find that the sequence ruptured a reverse-fault that is dipping with $\sim 30^\circ$ towards NNE at 6-7km depth. This is supported by both the hypocenters and the mainshock source mechanism. The fault is most likely located in the buried basement of the Bohemian massif, the "Bohemian Spur". This (reverse) fault has a nearly perpendicular orientation to the normal-fault structures of the Vienna Basin Transfer Fault System further East at shallower depth, indicating a lateral stress decoupling that can also act as a vertical stress-decoupling in some places. In the West, earthquakes (at larger depth within the upper crust) show compressive stresses, whereas the Cienna Basin shows extensional (normal-faulting) stress. This provides insight into the regional stress field and its spatial variation, and it helps to better understand earthquakes in the area, including the 1590 Neulengbach earthquake.

3.1 Introduction

The Alps have a rich and complex tectonic history, induced by the convergence of the African and European plates (e.g. Jolivet et al., 2003; Schmid et al., 2004; Malusà et al., 2015) that is not fully understood yet (e.g. Lippitsch et al., 2003; Mitterbauer et al., 2011; Sun et al., 2019). The convergence is accompanied by an eastwards extrusion of crustal blocks of the Eastern Alps since the late Oligocene and early Miocene (Gutdeutsch & Aric, 1988; Ratschbacher et al., 1991a; Wölfler et al., 2011). That lateral extrusion is associated with the formation of sinistral strike-slip faults, in particular the Salzach-Enns-Mariazell-Puchberg fault (SEMP, Figure 1) and the Mur-Mürz-Line fault (MML, Figure 1). Below these structures, we find the crystalline basement of the Bohemian

massif and, further to the East, the Austroalpine basement under the Vienna Basin (Wessely, 2006). These two basement types have rather different composition. The Bohemian massif is comprised of magmatic rocks, whereas the Austroalpine basement is comprised of sedimentary rocks (Wessely, 2006). Reinecker & Lenhardt (1999) argue that at this location the "Bohemian Spur" (see Fig. 3.1), the extent of the granitic basement of the Bohemian massif towards South, acts as an indenter, controlling the stress-field in the Eastern Alps.

Understanding of this area, together with the entire Alpine region, can now be improved, due to the new dataset that is currently gathered by the AlpArray project (Hetényi et al., 2018a). AlpArray is an international project of 24 institutions across Europe. It aims at advancing our understanding of the Alpine orogen and surrounding regions with a previously unachieved dense coverage of the entire Alps with broadband seismometers. In total, the network consists of almost 700 seismic stations, comprised of ~240 newly installed temporary broadband stations, ~30 ocean bottom seismometers, and ~400 permanent stations.

The Alland earthquake sequence (red circles in Fig. 3.1) is located just near the eastern edge of the Bohemian Spur (see Fig. 3.1). Seismic activity is commonly observed to the South along the MML and southern part of the Vienna Basin Transfer Fault System (VBTFS, Fig. 3.1), whereas it is more sparsely distributed to the North (Fig. 3.1). Still, one of the most notable earthquakes in the region, the so-called "Neulengbach earthquake" from the year 1590 (e.g. Gutdeutsch et al., 1987), has occurred in the same area (probably 20-30km to the North) with a macroseismic magnitude of ~6 (see Figure 1). Hammerl (2017) reappraised this earthquake to possibly have happened ~10km further towards East near Ried am Riederberg based on macroseismic data points. That earthquake was the strongest historically-documented earthquake in Northeastern Austria, which has produced significant damage in surrounding cities and villages, including Vienna. In the area surrounding the Alland earthquake series, only little seismic activity has been observed instrumentally in the past. According to the Austrian Earthquake Catalogue (AEC, 2018), there were only 13 documented earthquakes within a radius of 15km around the Alland main shock since the year 1000; the largest with an estimated magnitude ~4 in 1734 and none of the instrumentally recorded events exceeding magnitude 2.5. That makes the well-recorded Alland earthquake sequence and the information that can be gained from it particularly important. Earthquakes that have been detected along the MML and VBTFS consist mainly of strike-slip events, but there is also normal and reverse faulting (see Fig. 3.1), reflecting the complex tectonic setting of the region.

In this study, we analyze locations and focal mechanisms of the Alland earthquake series to gain additional insight into the regional stress field. Furthermore, the Alland sequence potentially illuminates the local fault geometry, which is only poorly known North of the MML and VBTFS due to the low seismicity of the region (see Figure 1). For this, we conduct two separate analyses that help constrain the properties of the ruptured fault. We study the hypocenter distribution of

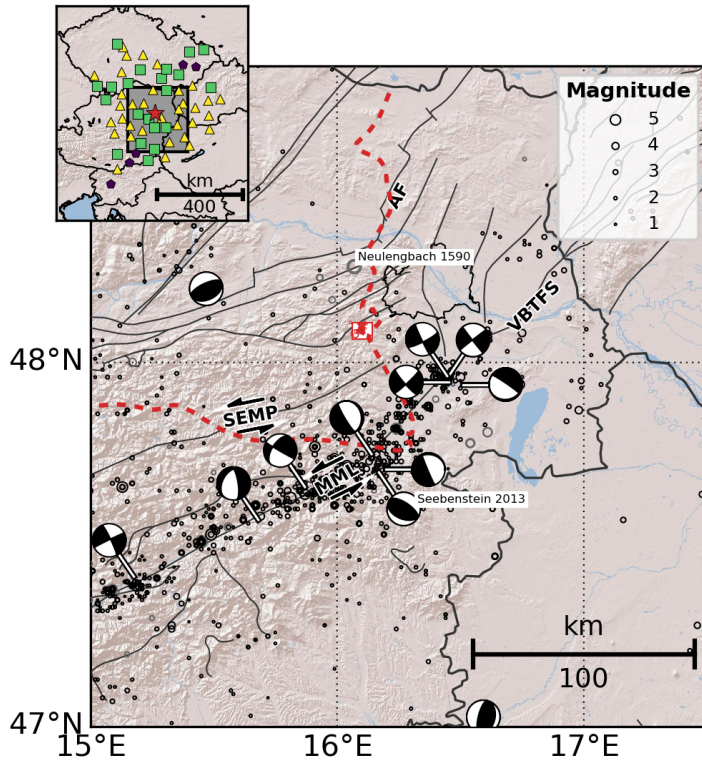


Figure 3.1: Map of historical seismicity in the study region. Earthquakes have been compiled from the Austrian Earthquake Catalogue and the EMSC catalogue. Black circles mark earthquakes after 1900, grey circles earthquakes before 1900, and red circles mark the Alland earthquake series. Source mechanisms are extracted from the ISC focal mechanism catalogue and provided by ZAMG. The red rectangle marks the zoomed-in view shown in Figure 3. Overview map (top left) shows the distribution of seismic stations used in this study. ■ marks stations that were used for relocation with HypoDD and moment tensor inversion, ▲ were used only during relocation, and ♦ were used only for moment tensor inversion. Red line marks the edge of the Bohemian Spur, redrawn from Wessely (2006). Labelled fault systems: AF (Alpine Front), SEMP (Salzach-Ennsbach-Mariazell-Puchberg fault), MML (Mur-Mürz Line), VBTFS (Vienna Basin Transfer Fault System).

the sequence (Section 4.1) and the source mechanism of the mainshock (Section 4.2). While the source mechanism gives insight into the rupture geometry, the detailed fault orientation can be poorly constrained, because of the limited resolution of long-period waves that are used to invert moment tensor solutions (e.g. Tsai, 2011). To help this, the aftershock distribution can provide additional information regarding the fault plane orientation (e.g. Rubin et al., 1999; Abercrombie et al., 2001; Bulut et al., 2007) and can help identify which of the two nodal planes has ruptured.

3.2 Data

The data used in this study consists of the seismic records of the Alland earthquake series recorded at 30 permanent stations (Czech Regional Seismic Network, 1973; Austrian Seismic Network, 1987; Hungarian National Seismological Network, 1992; Seismic Network of the Republic of Slovenia, 2004; National Network of Seismic Stations of Slovakia, 2004) and 51 temporary broadband stations of the AlpArray seismic network (AlpArray Seismic Network, 2015) in distances of 20 to 250km to the Alland main shock (see Fig. 3.1). Thanks to the consistent station spacing throughout the network, stations are distributed evenly in azimuth. Data were downloaded using the ORFEUS web services.

3.3 Earthquake Series Characterization

The Alland earthquake sequence spans \sim 1.5 years from April 2016 to November 2017 with 71 currently known events with $M_L \geq 0.1$ during that time, according to the Austrian Earthquake Catalogue (AEC, 2018). The events happened near the town of Alland, \sim 20km south-west of Vienna in the Eastern Alps (red circles in Fig. 1), in reported depths of 4 to 12km. Routine locations of the Alland series are available from the Austrian Seismological Service (Zentralanstalt für Meteorologie und Geodynamik, ZAMG), based on manual analysis of first P- and S-phase arrivals. The series seems to be divided into three sub-series that exhibit their own foreshock-mainshock-aftershock patterns (Fig. 3.2a).

The largest earthquake occurred on 25.04.2016 at 10:28:29UTC with an estimated local magnitude of $M_L = 4.2$. This mainshock is part of the first sub-series of earthquakes (yellow dots in Fig. 3.2a), which includes 37 events of $M_L \geq 0.1$ that show a typical decay of aftershock rate with time (Omori, 1894). After five days of no activity, the second sub-series (blue dots in Fig. 3.2a) with 20 events took place, including its largest event on 10.05.2016 with $M_L = 2.8$. Scattered throughout the following 2 months, there is little activity with 5 events $M_L < 2$ (white dots in Fig. 3.2a). Then, after 463 days of no activity, the third sub-series (green dots in Fig. 3.2a) occurred with 9 events, including the second-largest event of the series on 09.11.2017 with $M_L = 3.2$. For

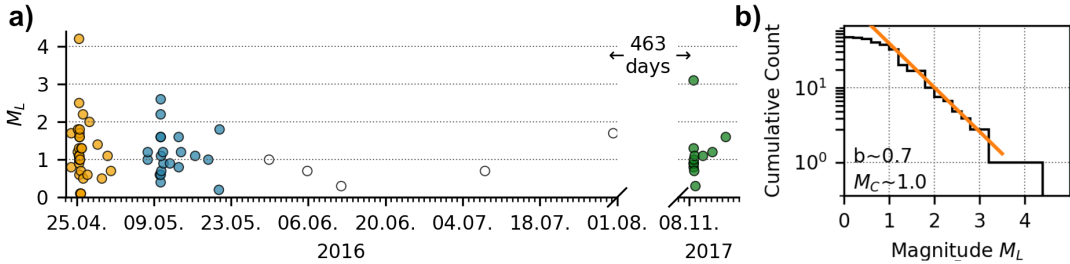


Figure 3.2: **a)** Time-history of the Alland earthquake series. The main shock occurred on 25.04.2016 with an estimated local magnitude of 4.2. We distinguish the series into three sub-series (marked as , ,). There is a 463-day-gap from 01.08.2016 to 08.11.2017 with no measured seismic activity in the area. **b)** Gutenberg-Richter plot of the Alland series. We find a b -value of 0.7 and estimate the magnitude of completeness M_C to be ~ 1.0 .

the complete sequence, we estimate the magnitude of completeness M_C , which is the lowest magnitude above which all events are detected, to be $M_C \simeq 1.0$ (Fig. 3.2b), which is similar to the one estimated for the Austrian Earthquake Catalogue from 1995 to 2018 ($M_C \simeq 1.4$, H. Hausmann, pers. comm.). A slightly lower M_C in this sequence may be attributed to the increased station density in recent years, e.g., as part of the AlpArray project. The b -value — the negative slope of the Gutenberg-Richter plot, which indicates the relative frequency of events with different magnitudes — is estimated as $b \simeq 0.7$ (Fig. 3.2b).

3.3.1 Locations

Accurate event locations can provide essential insight into the geometry and behavior of fault systems. Routine locations provided by ZAMG (Fig. 3.3) use the data of the AlpArray and TU-SeisNet (<http://gp.geo.tuwien.ac.at/gp/tuseisnet>) networks, but are based on phase-arrival picks only. No fault structure seems to emerge from these locations. This suggests either the events are broadly distributed and not located on a single fault or that there are large uncertainties in these locations.

To improve the absolute locations, we locate the events using NonLinLoc (Lomax et al., 2000) in a regional 3D velocity-model (Behm et al., 2007). NonLinLoc performs a probabilistic, non-linear, global search for earthquake locations in the given model using the Eikonal finite-difference scheme of (Podvin & Lecomte, 1991). We find the events to be slightly more clustered, and distributed along the discretized grid (Fig. 3.3b). Most notably, the largest events are now located $\sim 2\text{km}$ further towards north-east and the events are now in slightly shallower depth, around 1 to 12km.

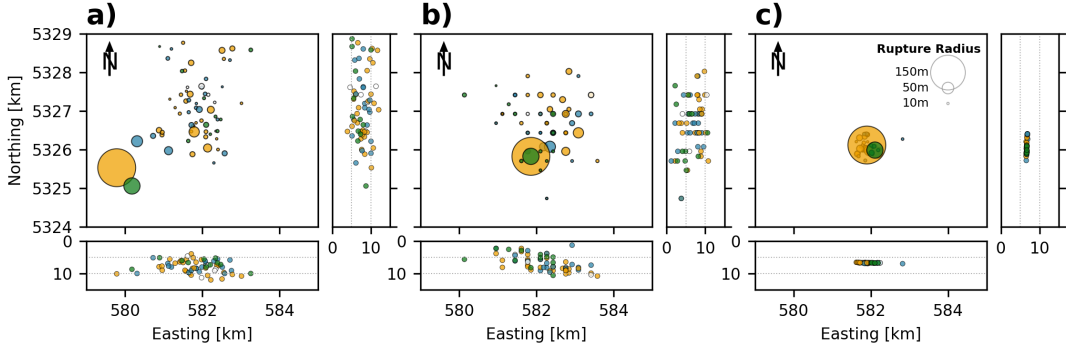


Figure 3.3: Locations of the earthquakes from the **a)** Austrian Earthquake Catalogue (AEC, 2018), **b)** NonLinLoc, and **c)** HypoDD. Circle sizes scale with the estimated rupture dimension, the drawn circle radii are three times the rupture radii. Circle colors are as shown in Figure 3.2. The coordinate system is UTM32N. While the NonLinLoc locations show already increased clustering of the events, the locations retrieved with HypoDD cluster very well in a narrow area.

Using these improved absolute locations as the initial locations, we relocate the events in this series relative to each other. Taking a double-difference approach to determine relative locations of nearby and similar events has been repeatedly shown capable to provide precise estimates of the rupture geometry; it is a well-established procedure (e.g. Prejean et al., 2002; Schaff et al., 2002; Waldhauser & Schaff, 2008). The approach is based on the assumption that differences in travel-times measured for nearby events are only caused by a change in location, as the path effects are essentially the same. We use the HypoDD software package (Waldhauser & Ellsworth, 2000; Waldhauser, 2001) to find improved relative locations. With this approach, 68 of the 71 known events in this series are relocated. Three events are excluded, because they occurred within only 16s and their waveforms overlap heavily. On these waveforms, we cannot easily distinguish the different phases of the three events.

We use both waveform cross-correlation as well as travel times from the catalogue (ZAMG) to estimate relative arrival times for all event pairs. Relative time shifts from cross-correlation are measured for P- and S-phase separately in time windows around the theoretical first P- and S-arrivals, computed by ray-tracing (Crotwell et al., 1999) in a 1D medium (Kennet, 1991). The P-phase time-window is defined as 2s before and 6s after the first theoretical arrival. For the S-phase, we use 2s before and 12s after. Some stations require static time corrections (up to 3s), because the 1D model does not account for lateral heterogeneities and therefore the theoretical phase arrivals are not always properly aligned with the actual arrivals in the seismograms (see

Fig. B.1). We bandpass-filter the data from 5Hz to 15Hz to ensure high signal-to-noise ratio (SNR) for all event magnitudes and exclude all waveforms with $SNR < 10$. Here, we define $SNR = \frac{\text{peak amplitude}}{\text{standard deviation(noise)}}$, where the noise window is in between the source time and the first theoretical P-arrival. For each station-pair we shift the filtered waveforms towards the highest cross-correlation coefficient, which also acts as the weight given to the measurement during the relocation process (see Fig. B.2). To ensure high data quality, we allow only measurements where the estimated relative P- and S-arrivals match roughly (i.e., they are within 10% of each other), given that both measurements passed the SNR threshold. We retrieve a total of 17,939 relative P- and 17,939 relative S-arrival times from waveform cross-correlation. The catalogue-based relative travel times for P- and S-phases are initially weighted with 0.01, because manual phase picks are generally less precise than waveform cross-correlations and are subject to human error. There are 3,235 relative P- and 2,913 relative S-arrival times available.

In HypoDD, we use the Singular-Value-Decomposition mode (Waldhauser & Ellsworth, 2000) to solve for relative locations, because the data set is relatively small and the computational cost is low. After testing several parameter settings, we decided to use four sets of four iterations each with successively stricter residual threshold (residual threshold for cross-correlations (WRCC) and catalogue data (WRCT) = None, 5s, 3s, and 2s) and maximum distance between linked pairs (distance-threshold for cross-correlations (WDCC) and catalogue data (WDCT) = None, None, 5km, and 3km). The velocity-model we use for relocation is the mean model extracted from Schippkus et al. (2018), assuming a v_p/v_s ratio of $\sqrt{3}$. All 68 events are automatically assigned to the same cluster by HypoDD.

The locations found with HypoDD are much more densely clustered than the previous locations (Fig. 3.3c), with estimated location errors less than 10m (see Appendix A). Most events are located to the south-east of the mainshock and all events are at shallower depth ($\sim 6.5 - 7.0$ km) than the previously inferred locations, with the mainshock at 6.7km depth (Figure 3.3c). All events seem to fit on a single fault plane, allowing us to fit a plane through the new locations of all events with $M_L > 0.2$ (Fig. 3.4a). The three events with $M_L \leq 0.2$ are apparently too weak to be well-located, as they have low signal-to-noise ratio and are recorded on only a few nearby stations, and they are excluded. We find an excellent match of the remaining events with that plane. The mean misfit is 20m and there is no deviation larger than 152m. To better illustrate the fit, we present a down-dip- and a side-view of the plane (Fig. 3.4b). The plane has a strike of 299° and dips towards NE with a dip angle of 26° from horizontal.

Most aftershocks do not cluster in the immediate vicinity of the mainshock (Fig. 3.4c), suggesting that most of them do not overlap with the co-seismic rupture area of the mainshock. They are more distributed towards the edge and outside of the main shock rupture area. Inter-event distances (Figure 4d), i.e., the distance of a given event to the next one, can be interpreted to give

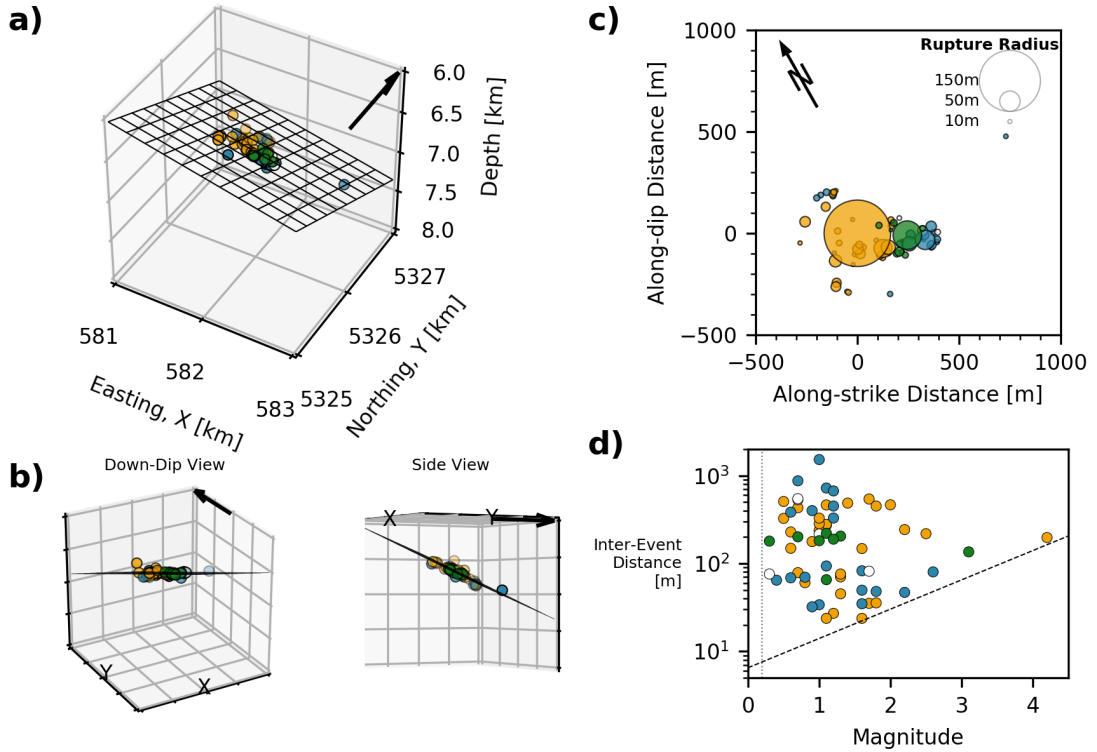


Figure 3.4: Final relative locations of the Alland earthquake series. **a)** Oblique 3D-view towards north-west of the hypocenter locations after relocating the event series with HypoDD, and the best-fitting plane through all events $M_L > 0.2$ with strike 299° and dip 26° (black mesh). **b)** Down-dip- and side-views of the plane to illustrate the fit. **c)** Fault-projected view of inter-event distances with circle sizes representing the estimated rupture areas. **d)** Inter-event distances, i.e., the distance from one event of a given magnitude to the next one in time. The dashed line represents the modelled rupture radius, which is used in c), assuming a stress drop of $\Delta\sigma = 10\text{ MPa}$. All arrows mark North. Circle colors are as shown in Figure 3.2.

an estimate of rupture size (Rubin et al., 1999) as it is unlikely for an aftershock to occur within the rupture area of its mainshock (Mendoza & Hartzell, 1988). Assuming a circular crack model, we can estimate the stress drop $\Delta\sigma$ by $r = (\frac{7M_0}{16\Delta\sigma})^{\frac{1}{3}}$ (Eshelby, 1957), with the rupture radius r and the seismic moment M_0 . Abercrombie (1996) gave an empirical relation between local magnitude M_L and seismic moment $M_0 = 10^{(1.0+M_L \cdot 9.8)}$, which we apply here. We estimate a stress-drop of $\Delta\sigma = 10\text{ MPa}$ (dashed line in Figure 4d) for the larger events, as there is no event below the dashed line (Rubin et al., 1999). This stress-drop is larger than the global average of 3MPa, but it is consistent with the fact that intra-plate earthquakes are often associated with larger stress-drop (Allmann & Shearer, 2009). Circle sizes in Figures 3 and 4c are based on these estimated fault dimensions. The new locations from NonLinLoc and HypoDD are attached as a table in the appendix (Table B.1).

3.3.2 Source Mechanism

We determine the source mechanism of the mainshock ($M_L = 4.2$ on 25.04.2016) by grid-searching the double-couple (DC) parameter-space for the best fit with synthetic waveforms. The synthetic waveforms for each combination of strike, dip, and rake are computed by modal summation using the Computer Programs in Seismology (Herrmann 2013) in a 1D model (Kennet 1991) for all necessary source-station distances and back-azimuths (known from Section 3.3.1), as well as a range of depths.

To evaluate the waveform fit, we follow the approach presented in Zhu & Helmberger (1996), which builds upon Zhao & Helmberger (1994) by fully using amplitude information. The approach combines L1- and L2-norm of the displacement-waveform-differences, where the waveforms are allowed to be shifted in time towards the best fit to account for regional geological deviations from the 1D model (for more details see B.1). This approach to misfit estimation is susceptible to strong biases by faulty/noisy channels, because there are no inherent quality checks performed on the data and the full waveform is utilized. Therefore, we take an iterative approach to finding the best solution for each depth, similar to Duputel et al. (2012), in which we run multiple iterations with increasingly stricter waveform selection (for more details see B.2). For the first run, we remove only channels with physically unreasonable amplitudes, most likely caused by incorrect instrument response information.

To reduce computational cost, the parameter space is confined by excluding equivalent plane solutions, i.e., we limit strike to $180^\circ - 360^\circ$. We sample the parameter space with 5° spacing in strike, dip, and rake during the first two iterations, and increase the grid density to 1° spacing for the last three iterations to converge to a more precise solution.

We use bandpass-filtered waveforms in the frequency band from 0.02Hz to 0.05Hz to estimate

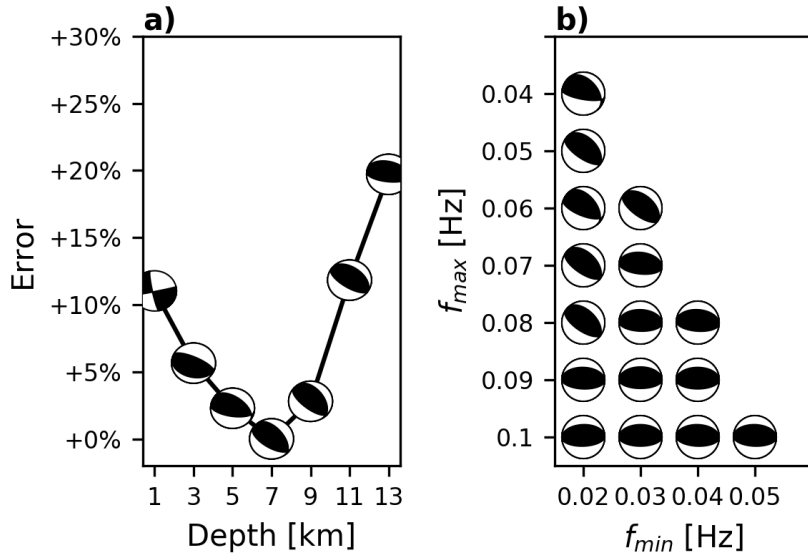


Figure 3.5: **a)** Depth-dependence of the mainshock source mechanism. In most depths a reverse-faulting mechanism is preferred and the lowest misfit is found at 7km depth. **b)** Frequency-band dependence of the best-fit source mechanism in 7km depth. In all tested frequency bands a reverse-faulting mechanism is preferred. The strike of the preferred rupture plane varies NW-SE to W-E for higher frequencies.

the waveform-fit. In this band, we do not expect the seismic wave propagation to be heavily influenced by local geological heterogeneities, i.e., the waves are dominated by source- rather than path- or site-effects. Therefore, we deem computing the synthetic waveforms in a 1D model appropriate, given that we allow the waveforms to shift in time. We decided on the 0.02Hz - 0.05Hz frequency-band to have the waveform-fit be insensitive to local heterogeneities. This also reduces the amount of information that needs to be fit, for lower computational cost. The downside of this choice is that the iterative approach eliminates more channels if the periods used are relatively long, because not all stations have good-quality long-period records on all components. This affects especially the horizontal channels of the temporary stations of the AlpArray project. 36 channels (27 Z, 7 R, 2 T) are used in the final iteration to compute the best-fit solution.

We compute the best-fit solution for depths from 1km to 13km in 2km steps (Figure 3.5) to get additional constraints on the depth of the mainshock that may reassure our findings in section 4.1. The best waveform fit is found for a source at 7km depth. All depths from 5km to 9km show misfits within 5% of the lowest misfit. A reverse-faulting solution is preferred for all depths from 3km to 13km, and only at 1km depth a strike-slip solution is found, although with considerably higher error (+11%). There, the solution is based only on 5 remaining waveforms in the final iteration. We

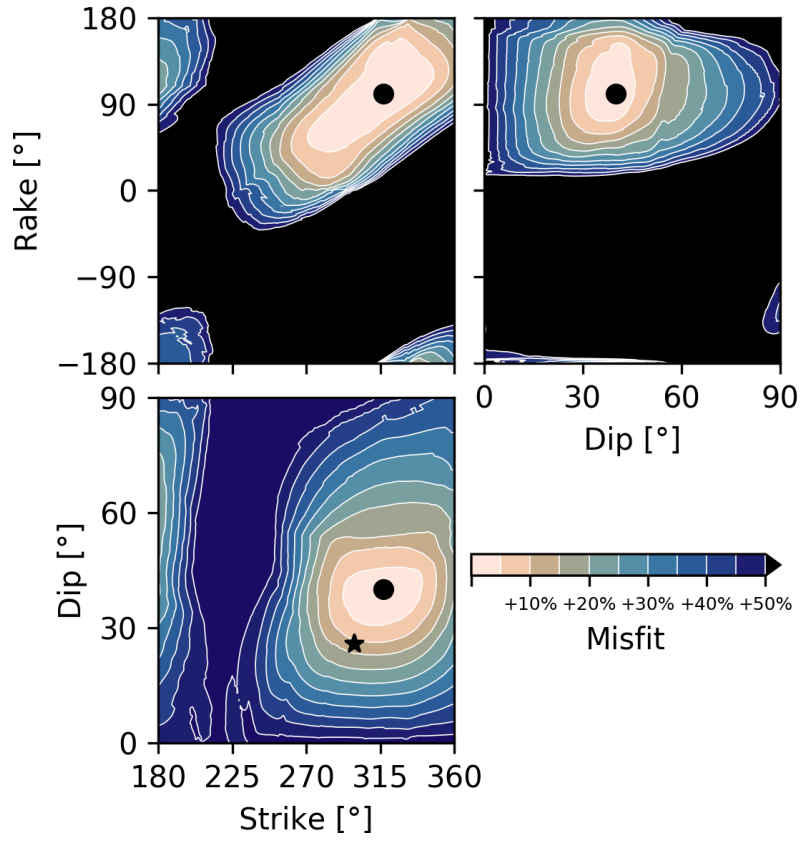


Figure 3.6: Slices through the solution space, crossing the best-fit solution (●) for 7km depth and 0.02Hz - 0.05Hz frequency-band for the last iteration, estimated on the 30 remaining waveforms. ★ marks the orientation of the plane fit through the earthquake hypocenters (see Fig. 3.4, Section 3.3.1).

tested the influence of the frequency-band on our results and found that reverse-faulting solutions are preferred for all tested frequency-bands at 7km depth (Figure 3.5b), although the best-fit strike changes between SW/NE- and W/E-orientations, depending on the band.

Three slices crossing the DC parameter-space for the best-fit source-mechanism with a source depth of 7km show a stable solution that is well-defined in the rake-strike, rake-dip, and dip-strike planes (Fig. 3.6). We find that the main shock ruptured as a slightly oblique reverse-faulting event on either a plane with strike 317° , dip 40° , and rake 101° , or on the equivalent plane with 123° strike, 51° dip and 81° rake. The moment magnitude $M_W = 3.7$ is estimated from the mean seismic moment (Hanks & Kanamori, 1979) measured over all 36 channels that were used in the last iteration (Fig. 3.7).

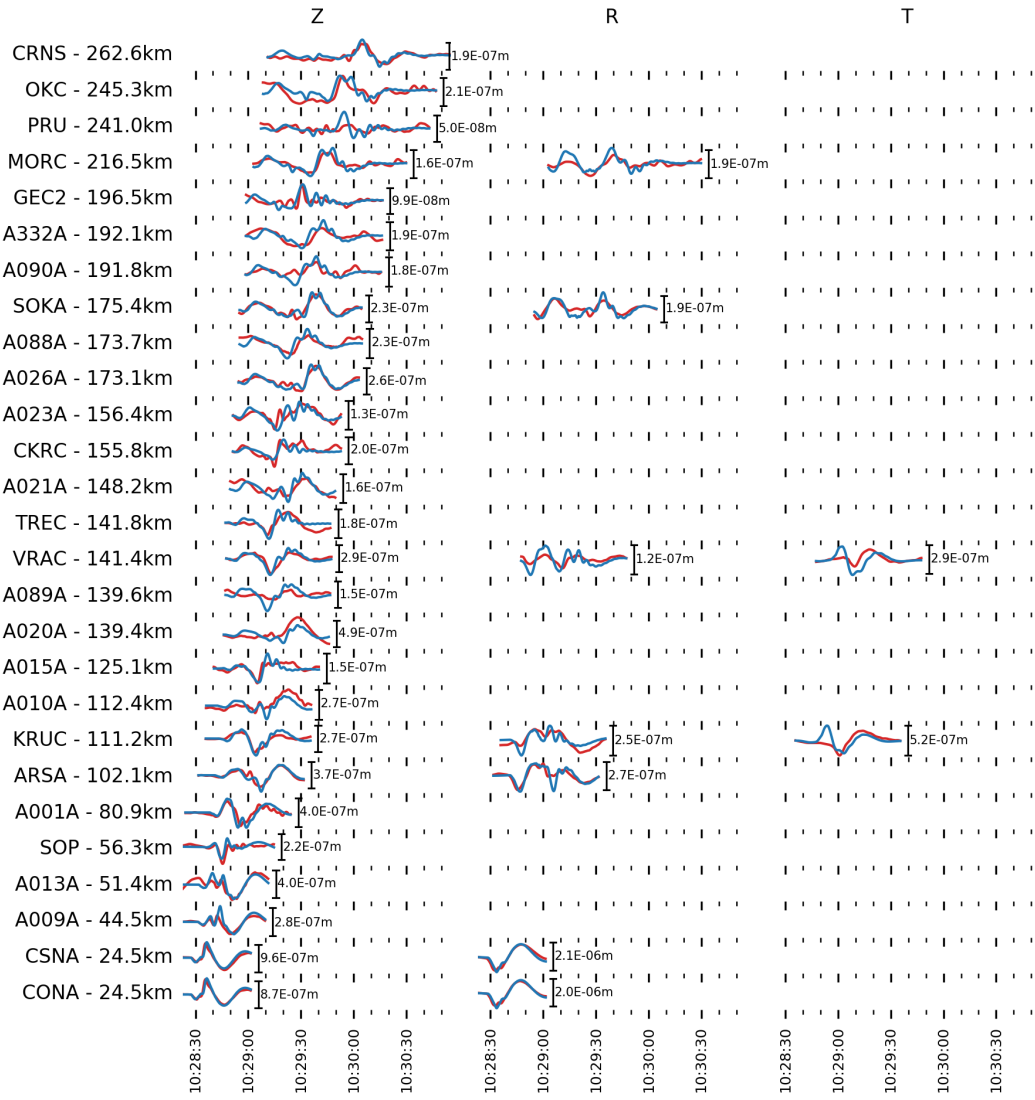


Figure 3.7: Waveform fit of recorded displacement seismograms (red) and synthetic waveforms (blue) for 7km depth and 0.02Hz - 0.05Hz. Shown are the 36 remaining waveforms in the last iteration.

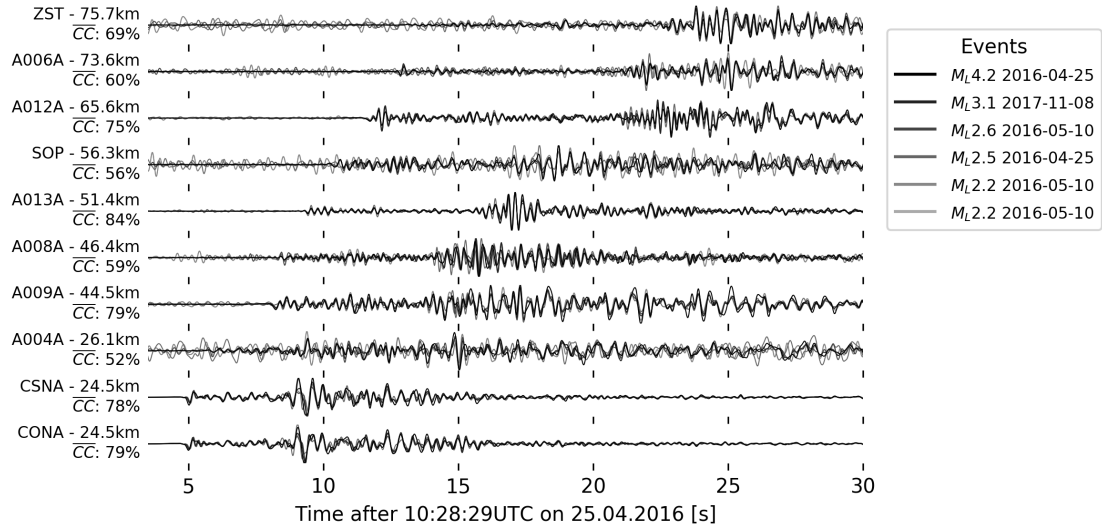


Figure 3.8: Overlaid waveforms (vertical component) of the 6 largest events ($M_L > 2$) in the series, bandpass-filtered 0.5Hz - 5Hz and shifted towards the best fit on the 10 closest stations. A strong similarity between aftershock waveforms with the main shock (mean cross-correlation coefficients (CC) between 52% and 84%) suggest similar source mechanisms and locations for all of these events.

The waveform fit with synthetics for smaller events in the series, e.g., the $M_L = 3.2$ earthquake on 08.11.2017, proved to be unstable. Because of the lower magnitude, higher frequencies have to be utilized, as recordings of lower frequencies are heavily affected by long-period noise for smaller earthquakes. Comparing waveforms at these higher frequencies leads to inaccuracies due to computing the synthetics without full knowledge of the subsurface structure. The available network of stations is not dense enough (40km average inter-station spacing) to find a stable DC-solution by waveform comparison with synthetics at higher frequencies. Instead, we visually compare the seismograms of the six largest events ($2.2 \leq M_L \leq 4.2$), recorded on the vertical components (bandpass-filtered 0.5Hz - 5Hz) of the ten closest stations to the source (Fig. 3.8). We find a remarkable similarity of these waveforms (mean cross-correlation coefficients (CC) with the mainshock from 52% to 84%, Figure 8). This clearly suggests that the mechanisms for the largest aftershocks are very similar to the main shock.

3.4 Discussion

We have studied locations of the Alland earthquake sequence and the orientation of the main shock, and we have seen that the earthquakes occurred on a rather well-defined planar surface in the basement, which agrees fairly well with (one of the possible) fault planes of the Alland main shock (Fig. 3.6). We will discuss this, starting with the robustness of our results and later putting them into the geological/tectonic context of the region. The hypocenter location errors from HypoDD in all three dimensions are small, usually well below 10m (see Table B.1). The depth determined from the source mechanism, on the other hand, is only poorly constrained. The misfit found at depths from 5 to 9km depth are within only 5% of the misfit at 7km depth (Fig. 3.5). We do not claim this difference in waveform fit to be significant enough to make statements about source depth from the source mechanism alone. Still, the best-fit depth corroborates the depth found by relocation (6.7km, Figs. 3.3, 3.4, Table B.1). Similarly, the fault planes found from aftershock hypocenters (strike 299° and dip 26° , Fig. 3.4) and the mainshock source mechanism (strike 317° , dip 40° , rake 101° or equivalently strike 123° , dip 51° , rake 81° ; Fig. 3.6) agree fairly well, although the dip towards NNE differs by 14 degrees. When looking at solutions that are within 5% misfit of the best-fit source mechanism (first contour line in Fig. 3.6), we cannot confidently distinguish solutions over a relatively wide range in strike ($\sim 290^\circ - 340^\circ$) and dip ($\sim 30^\circ - 45^\circ$) and an interdependence of strike and rake is apparent. We show only three planes crossing the global minimum in the 3-D parameter space that can only give limited insight into the distribution of misfits in the full parameter space. Still, it seems that the dip angle is constrained better than strike and rake (Fig. 3.6). We can therefore consider the two found planes to be consistent with each other. This also supports our choice of frequency-band for the inversion (Fig. 3.5b). While the fault orientation rotates towards E-W-strike at higher frequencies, the two independent analyses of the fault plane orientation match only for the lower frequencies used in this study, suggesting that small-scale geological heterogeneities may indeed bias the results of the moment tensor inversion at higher frequencies.

This is further supported by the two other fault plane solutions of the Alland mainshock that are available from ZAMG (Freudenthaler, pers. comm.) and Saint Louis University Earthquake Center (Saint Louis University, 2016). The solution provided by ZAMG is based on manual analysis of first P-arrivals, their polarities and SV to P amplitude ratios (Fig. 3.8a), whereas the automatically generated solution by SLU (Fig. 3.8b) is based on fitting waveforms with synthetics, similar to our approach. We find good agreement of our results with the solution reported by ZAMG (strike 324° , dip 41° , rake 105°), while the solution reported by SLU (strike 348° , dip 46° , rake 144°) deviates from our findings, mostly in rake. We speculate that this is the case, because the SLU-solution is based on only permanent stations that are preferentially distributed towards North and South and not all waveforms used for the determination of the source mechanism have high cross-correlation

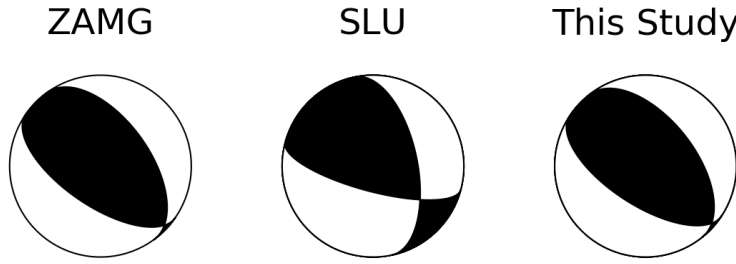


Figure 3.9: Fault plane solutions. Left: $323^\circ/41^\circ/105^\circ$ from Zentralanstalt für Meteorologie und Geodynamik (ZAMG) based on first P-, SH-, and SV-arrival polarities (Freudenthaler, pers.comm.). Center: $348^\circ/46^\circ/144^\circ$ from Saint Louis University Earthquake Center (SLU) based on waveform fitting with synthetics using only permanent stations that are preferentially distributed towards North and South (Saint Louis University, 2016). Right: $317^\circ/40^\circ/101^\circ$ from this study.

coefficients with the synthetics (as low as 4%, Saint Louis University (2016)). Nonetheless, the SLU-solution seems to lie within +5% misfit our best-fit solution (Figure 6).

The Alland earthquake sequence ruptured a fault that is situated near the eastern edge of the Bohemian Spur at depths of 3-4km below the crystalline basement top (Fig. 3.10). In Fig. 3.10, we show the first depth at which the shear-velocity model of Schippkus et al. (2018) exceeds 2.9km/s. Schippkus et al. (2018) argue that the 2.9km/s-isosurface is a good representation of the crystalline basement top. We compare these depths with basement depths known from boreholes and interpreted from geological profiles (Fig. 3.10), as well as the shape of the Bohemian Spur as drawn in Wessely (2006) (dashed line, Fig. 3.10). We find reasonable agreement between these observations. An important question for the understanding of this sequence is where exactly the edge of the Bohemian Spur is located and whether the ruptured fault is located in the granitic basement of the Bohemian Massif or in the sedimentary Austroalpine basement to the east. The velocity-model of Schippkus et al. (2018) seems to corroborate a shape of the Bohemian Spur similar to that in Wessely (2006) (dashed line, Fig. 3.10). We extract shear-velocity profiles from the model of Schippkus et al. (2018) in the study area and classify them as being located ‘inside’ or ‘outside’ the Bohemian Spur, following the interpretation of Wessely (2006) (Fig. 3.11). We find that the velocity profile near Alland (black line in Fig. 3.11, top) more closely resembles the mean velocity profile inside the Bohemian Spur (red line in Fig. 3.11, top). The RMS-misfit between these two profiles is 0.08km/s, compared to 0.21km/s for the mean velocity profile outside the Bohemian Spur (blue line in 3.11, top). The distribution of velocities at 7km depth, the source depth of the Alland sequence, further illustrates that the shear-velocities found near Alland (black line in Fig. 3.11, bottom) match the distribution of velocities inside the Bohemian Spur (red histogram in Fig.

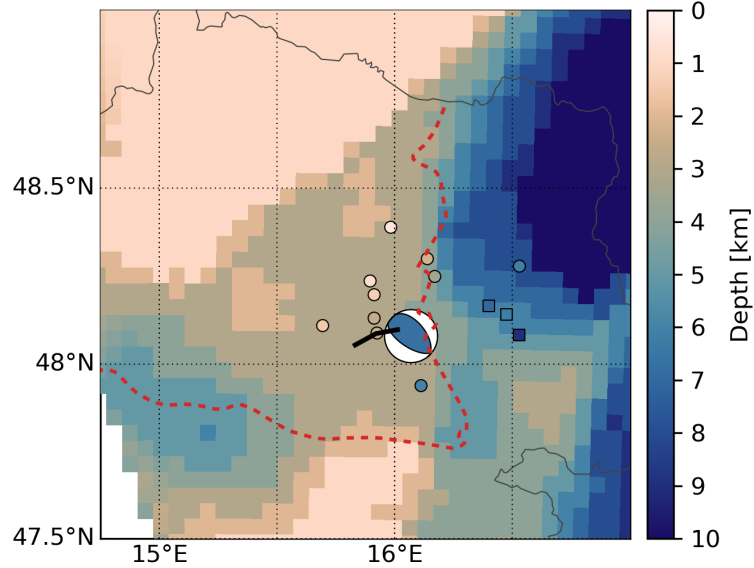


Figure 3.10: Alland earthquake near the edge of the Bohemian Spur. Background image shows the first depth at which 2.9km/s shear-velocity is exceeded in the velocity model of Schippkus et al. (2018), which may be interpreted as the top of crystalline basement (see Schippkus et al., 2018, for more details). Crystalline basement depths, known from boreholes (marked as \circ) or estimated from geological profiles (marked as \square) from Wessely (2006). The beachball represents the Alland main shock, also colored by depth. Red line marks the edge of the Bohemian Spur, redrawn from Wessely (2006). Black line marks seismic profile C 8503 that crosses the borehole St. Corona 1 (see Fig. 3.12).

3.11, bottom) better.

Therefore, it seems very likely that the Alland sequence ruptured the crystalline basement of the Bohemian Massif and not the Austroalpine basement. In the Bohemian Massif, a criss-cross pattern of SSW/NNE- as well as SSE/NNW-striking strike-slip faults is well documented (e.g. Brandmayr et al., 1995), which have shown only little activity recently. A continuation of this fault pattern down to the buried Bohemian Spur appears quite possible; this could then result in a favourable alignment of one of these faults, so it might have been reactivated by reverse faulting.

The seismic reflection profile C 8503, kindly provided by OMV, crosses the nearby borehole St. Corona 1 and runs in close proximity to the Alland sequence epicenters (Fig. 3.12); the eastern end of the profile is located in \sim 7km distance. The borehole gives ground truth for the top of the crystalline basement in 2.6km (at \sim 1s one-way-travel-time (OWT) in the profile). Below, in the

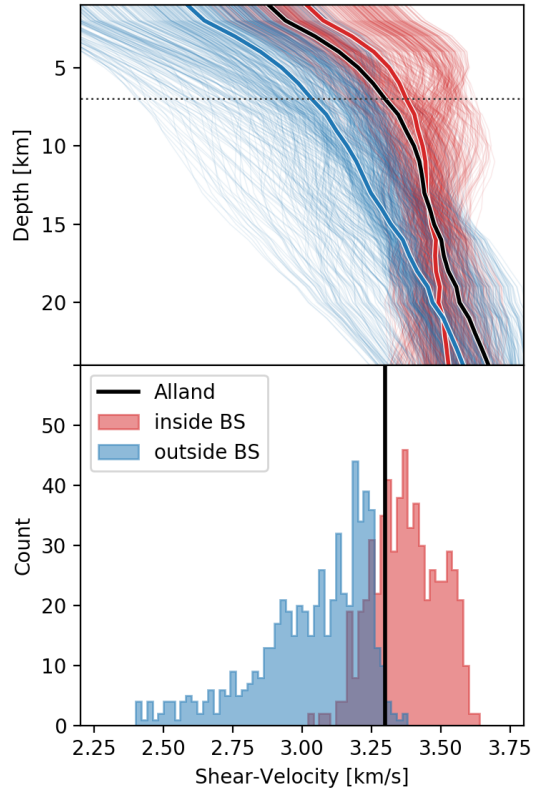


Figure 3.11: Velocity model of Schippkus et al. (2018), classified by 'inside' (red color) and 'outside' (blue color) the Bohemian Spur (BS) after Wessely (2006). Classification is based on edge of the BS as drawn in Figures 3.1 and 3.10. Top: Velocity profiles, extracted at each grid-cell in Figure 3.10, extracted from Schippkus et al. (2018). Thick lines represent the mean velocity profiles inside (red) and outside (blue) of the BS. The velocity profile at the location of the Alland sequence is drawn in black. The Alland profile (black) is similar to the mean velocity profile inside the BS (red). Bottom: Histogram of shear velocities at 7km depth (source depth of Alland main shock, dotted line in top panels). Clear separation of faster and slower velocities by the classification with some overlap. The shear-velocity found in 7km depth near the Alland series (black line) appears more likely to be representative of the BS (red distribution).

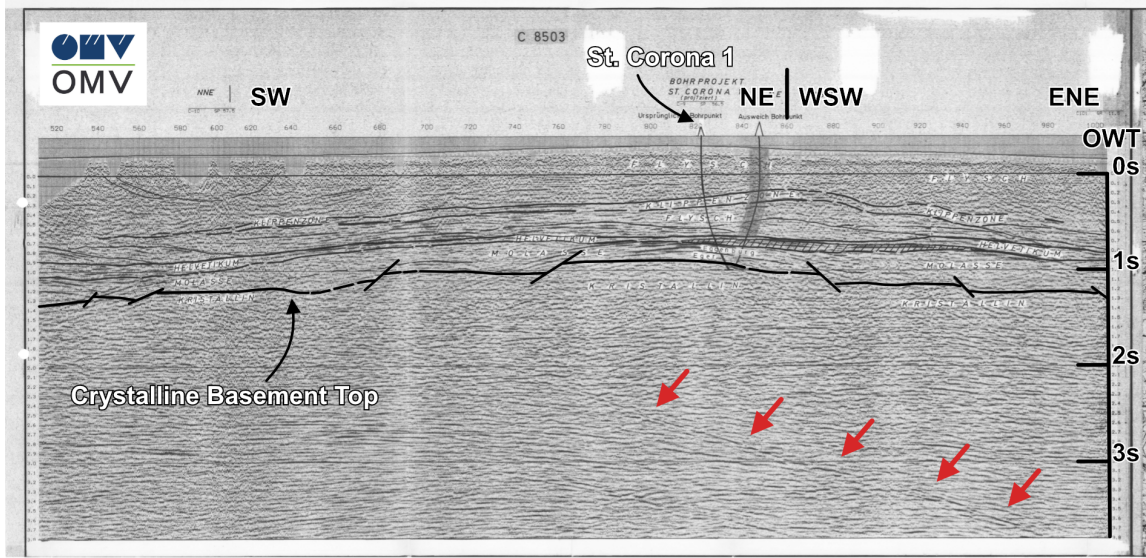


Figure 3.12: Seismic reflection profile C 8503, provided by OMV. The profile crosses the borehole St. Corona 1, which reached the crystalline basement at 2.3km depth, corresponding to 1s one-way-travel-time (OWT) in the profile. The Alland sequence ruptured a fault at 6-7km depths (~3s OWT). At these depths, the profile reveals an extensive ~NE dipping feature in the crystalline basement (indicated by red arrows), roughly consistent with the fault-orientation of the Alland sequence (see Figs. 3.4, 3.6, 3.9). The eastern end of the profile is located ~7km from the Alland main shock (see Fig. 3.10).

crystalline basement, there is an extensive ~NE-dipping reflector visible at ~3s OWT (red arrows in Fig. 3.12), corresponding to depths of ~6-7km. This profile confirms the presence of major NE-dipping features in the crystalline basement, in depths consistent with the fault plane of the Alland sequence (see Figs. 3.4, 3.6, 3.9).

The Alland sequence ruptured the fault with a reverse mechanism, which is not uncommon in the area. The Seebenstein $M_L = 3.6$ earthquake of 25.01.2013 was a reverse-faulting earthquake, with a rather similar source geometry to that of the Alland earthquake (see Fig. 3.1) and at a similar depth (10km from AEC, 2018). On 16.04.2019 a $M_L = 3.1$ earthquake occurred about 40km to the North, near Tulln (April 2019 seismicity report from ZAMG) in a previously seismically quiet area, which potentially ruptured more shallow rocks (9km depth from ZAMG) with a reverse-faulting mechanism that may have been oriented similarly to the Alland earthquake (C. Freudenthaler, pers. comm.). There were reverse-fault events dispersed throughout the Northern Calcareous Alps (C. Freudenthaler, pers. comm.), and they may possibly also have occurred in Eastern Switzerland (Strasser et al., 2006). These observations in combination with the results presented in this paper

make it clear that reverse faulting is an important rupture mechanism in the Eastern Alps and along its eastern edge.

These consistent larger-scale observations are likely driven by the regional stress field. The Alland earthquake with a moment magnitude $M_W = 3.7$ therefore also sheds light on the regional stress field, and thus into the forces that drive tectonic deformation in the area today. The source area of the main shock is about 400m long (see Fig. 3.4c); due to this extended size the earthquake is probably more representative of the regional stress field than borehole-derived stress indicators that relate to smaller spatial scales, and usually to shallower levels in the crust. The source mechanism of the main shock indicates that the maximum horizontal compressive stress σ_H is oriented ~ 30 degrees from North over East in the upper crust near the edge of the Bohemian Spur. The dip of the fault plane is around 26 - 40 degrees from the horizontal (see Figs. 3.4, 3.6), a nearly-optimal orientation for a reverse fault. This also supports the Alland earthquake as an important indicator for the regional stress field in this region, where we have little information on crustal stress.

The study of Reinecker & Lenhardt (1999) implies that this reverse-faulting stress regime with a SSW-NNE orientation of σ_H is prevalent in the region to the West of Alland, till Salzburg. Near the eastern edge of the Bohemian Spur, however, they report SSE/NNW σ_H -orientations, which would render the observed source mechanism of the Alland main shock unlikely, if not impossible. If the rotation of σ_H -orientation around the Bohemian Spur was not representative of the regional stress field and instead SSW/NNE-orientations were also present just (south-)east of the Bohemian Spur, that would furthermore render the Southern Vienna Basin Transfer fault (VBTSF in Fig. 3.1), as well as the Mur-Mürz-Line (MML in Fig. 3.1) nearly optimally-oriented, as strike-slip faults. Indeed, larger-scale studies (e.g. Bada et al., 2007; Heidbach et al., 2018) also show a coherent SSW/NNE orientation of σ_H in the Vienna basin.

This leads us to speculate that the mountain-range-perpendicular σ_H -orientation, rotating along the Alpine front and observed elsewhere, e.g., in Bavaria and Switzerland (Reinecker et al., 2010; Heidbach et al., 2018), also holds for eastern Austria. This may indicate that a buoyancy- rather than rheology-driven stress field (as suggested in Reinecker & Lenhardt (1999)) may be important, but to substantiate this is beyond the scope of this paper.

The tectonic regime in the adjacent Vienna basin is obviously a different one compared with that in the Bohemian Spur and West of it; it is dominated by strike-slip and normal faulting. It may be surprising that the tectonic regime can vary over distances of just tens of kilometers. There have been suggestions before though that the stress field in the Vienna basin differs from that in the basement below. In particular, the Steinberg fault (e.g. Lee & Wagreich, 2016) seems to be the place of a major change in the orientation of the stress field (Marsch et al., 1990; Decker et al., 2005).

While we are confident that the results presented in this paper are sound, further analysis of the sequence can help confirm our findings, mainly by detection and location of additional aftershocks to more precisely constrain the rupture fault geometry. These currently include only events found by routine analysis at ZAMG. No automatic detection of aftershocks was performed, e.g., by matched filtering (Caffagni et al., 2016) or subspace detectors (Harris, 2006). Additionally, further improving the density of the regional seismic network may help detect and locate especially smaller magnitude events that currently may be missed. While the AlpArray Seismic Network (2015) provides great insight in that regard, it is a temporary deployment of just a few years, and gives an important but only partial view into the seismicity. Densifying the permanent network seems an important task for the future.

3.5 Conclusions

We provide information about the geometry and behavior of the fault involved during the Alland earthquake sequence in eastern Austria. The Alland earthquake sequence occurred from April 2016 to November 2017 and includes 71 known events, its largest event has a moment magnitude of $M_W = 3.7$. Our source mechanism indicates that this event ruptured a reverse-fault with a strike of 317° and a dip of 40° (Fig. 3.6), which is roughly consistent with the distribution of relocated aftershock hypocenters that fit on a plane with strike 299° and dip 26° (Fig. 3.4). The six largest events ($M_L > 2$) show high waveform-similarity with the main shock, suggesting that these events ruptured with similar reverse-fault mechanisms (Fig. 3.8). Earthquake relocation indicates that the sequence occurred at around 6.5 - 7km depth with the mainshock at 6.7km (Fig. 3.4), which is in agreement with the best point-source depth of our moment tensor inversion (Fig. 3.5). The ruptured fault is situated near the eastern edge of the Bohemian Spur (Fig. 3.10) in depths below the overthrust Alpine nappes and likely ruptured a pre-existing fault in the granitic basement of the Bohemian Massif (Figs. 3.11, 3.12). This event provides evidence that the orientation of the maximum horizontal stress σ_H in the upper crust in this region may be oriented normal to the Alps, which is also observed in the Western and Central Alps (Reinecker et al., 2010; Heidbach et al., 2016), resulting in a \sim NNE-orientation of σ_H at the eastern edge of the Eastern Alps. This is suggestive of an important effect from buoyancy (caused by the higher elevation of the Alps and Bohemian massif, and possibly by lateral density variation, e.g., by crustal roots) on the stress field in the vicinity of the Alps. In any case, the orientation of the stress field in the basement seems to be different from the one in the adjacent (and partly overlying) Vienna Basin, and the basin-bounding faults seem to be effective in decoupling the two stress fields. The Alland earthquake, the very recent 2019 Tulln earthquake, and potentially also the $M \simeq 6$ Neulengbach/Ried am Riederberg earthquake of 1590, have responded to the compressive basement stress field.

Acknowledgements

The data used in this study are provided by the operators of the national seismic networks (Czech Regional Seismic Network, 1973; Austrian Seismic Network, 1987; Hungarian National Seismological Network, 1992; Seismic Network of the Republic of Slovenia, 2004; National Network of Seismic Stations of Slovakia, 2004) and the members of the AlpArray Working Group (AlpArray Seismic Network, 2015). We thank the AlpArray Seismic Network Team: György HETÉNYI, Rafael ABREU, Ivo ALLEGRETTI, Maria-Theresia APOLONER, Coralie AUBERT, Simon BESANÇON, Maxime BÉS DE BERC, Götz BOKELMANN, Didier BRUNEL, Marco CAPELLO, Martina ČARMAN, Adriano CAVALIERE, Jérôme CHÉZE, Claudio CHIARABBA, John CLINTON, Glenn COUGOULAT, Wayne C. CRAWFORD, Luigia CRISTIANO, Tibor CZIFRA, Ezio D'ALEMA, Stefania DANESI, Romuald DANIEL, Anke DANNOWSKI, Iva DASOVIĆ, Anne DESCHAMPS, Jean-Xavier DESSA, Cécile DOUBRE, Sven EGDORF, ETHZ-SED Electronics Lab, Tomislav FIKET, Kasper FISCHER, Wolfgang FRIEDERICH, Florian FUCHS, Sigward FUNKE, Domenico GIARDINI, Aladino GOVONI, Zoltán GRÁCZER, Gidera GRÖSCHL, Stefan HEIMERS, Ben HEIT, Davorka HERAK, Marijan HERAK, Johann HUBER, Dejan JARIĆ, Petr JEDLIČKA, Yan JIA, Hélène JUND, Edi KISSLING, Stefan KLINGEN, Bernhard KLOTZ, Petr KOLÍNSKÝ, Heidrun KOPP, Michael KORN, Josef KOTEK, Lothar KÜHNE, Krešo KUK, Dietrich LANGE, Jürgen LOOS, Sara LOVATI, Deny MALEN-GROS, Lucia MARGHERITI, Christophe MARON, Xavier MARTIN, Marco MASSA, Francesco MAZZARINI, Thomas MEIER, Laurent MÉTRAL, Irene MOLINARI, Milena MORETTI, Helena MUNZAROVÁ, Anna NARDI, Jurij PAHOR, Anne PAUL, Catherine PÉQUEGNAT, Daniel PETERSEN, Damiano PESARESI, Davide PICCININI, Claudia PIROMALLO, Thomas PLENEFISCH, Jaroslava PLOMEROVÁ, Silvia PONDRELLI, Snježan PREVOLNIK, Roman RACINE, Marc RÉGNIER, Miriam REISS, Joachim RITTER, Georg RÜMPKER, Simone SALIMBENI, Marco SANTULIN, Werner SCHERER, Sven SCHIPPKUS, Detlef SCHULTE-KORTNACK, Vesna ŠIPKA, Stefano SOLARINO, Daniele SPALLAROSSA, Kathrin SPIEKER, Josip STIPČEVIĆ, Angelo STROLLO, Bálint SÜLE, Gyöngyvér SZANYI, Eszter SZŰCS, Christine THOMAS, Martin THOR-WART, Frederik TILMANN, Stefan UEDING, Massimiliano VALLOCCHIA, Luděk VECSEY, René VOIGT, Joachim WASSERMANN, Zoltán WÉBER, Christian WEIDLE, Viktor WESZTERGOM, Gauthier WEYLAND, Stefan WIEMER, Felix WOLF, David WOLYNIEC, Thomas ZIEKE, Mladen ŽIVČIĆ. The software used in this study was kindly provided by Lomax et al. (2000), Herrmann (2013), and Krischer et al. (2015). Part of this work was performed using funding from the Austrian Science Fund (FWF): Projects 26391 and 30707. The authors thank the Austrian Agency for International Cooperation in Education & Research (OeAD-GmbH) for funding the Amadée project FR02/2017, which helped directly facilitate work on this project. This project was co-funded by the French Europe & Foreign Affair ministry and the French Higher Education and Research ministry under the project number PHC-AMADEUS 38147QH. Thanks to OMV for insightful discussions and providing the seismic reflection profile C 8503. Thanks to the Central Institute for Meteorology and Geodynamics, Vienna, Austria (ZAMG) for providing their focal mechanism solution for the 2015 Alland and 2019 Tulln main shocks.

4 Azimuthal anisotropy as a proxy for the stress-field

This section has been submitted to Geophysical Journal International on 01.08.2019 as:

Schippkus, S., Zigone, D., Bokelmann, G., the AlpArray Working Group. Azimuthal anisotropy in the wider Vienna Basin region: A proxy for the present-day stress field and deformation

Abstract

We infer seismic azimuthal anisotropy from ambient-noise-derived Rayleigh waves in the wider Vienna Basin region. Cross-correlations of the ambient seismic field are computed for 1,953 station pairs and periods from 5s to 25s to measure the directional dependence of inter-station Rayleigh-wave group velocities. We perform the analysis for each period on the whole dataset, as well as in overlapping 2° -cells to regionalize the measurements, to study expected effects from isotropic structure, and isotropy-anisotropic tradeoffs. To extract azimuthal anisotropy that relates to the anisotropic structure of the Earth, we analyze the group velocity residuals after isotropic inversion. The periods discussed in this study (5s - 20s) are sensitive to the crustal structure, and they allow us to gain insight into two distinct mechanisms that result in fast orientations. At shallow crustal depths, fast orientations in the Eastern Alps are oriented S/N to SSW/NNE, roughly normal to the Alps. This effect is most likely due to the formation of cracks aligned with the present-day stress-field. At greater depths, fast orientations rotate towards NE, almost parallel to the major fault systems that accommodated the lateral extrusion of blocks in Miocene. This is coherent with the alignment of crystal grains during crustal deformation occurring along the fault systems and the lateral extrusion of the central part of the Eastern Alps.

4.1 Introduction

Tectonics and seismic activity are consequences of the acting stress field. Gaining insight into the present-day orientation of the stress-field and its evolution over geological time can thus improve our understanding of regional tectonics and future seismicity sharply. Today, the wider Vienna Basin region is one of the seismically most active regions in Austria. It has been subject to major earthquakes in the past, e.g., the M~6 Neulengbach/Ried am Riederberg event in 1590 that caused considerable damage in Vienna (e.g. Gutdeutsch et al., 1987; Hammerl & Lenhardt, 2013). Due to the short earthquake record in the area and the sparse knowledge of the regional stress field, there are major uncertainties in seismic hazard assessments in the region. Various techniques such as paleoseismology have been used to better constrain past and current seismic hazard (Gribovszki et al., 2017; Hintersberger et al., 2018), however they remain mostly pointwise measurements that lack the coverage over the whole Vienna Basin region. Understanding the stress field better, and which faults may be reactivated to produce significant earthquakes in the

near future - as dictated by the stress-field - is therefore of great importance for accurate assessment of seismic hazard.

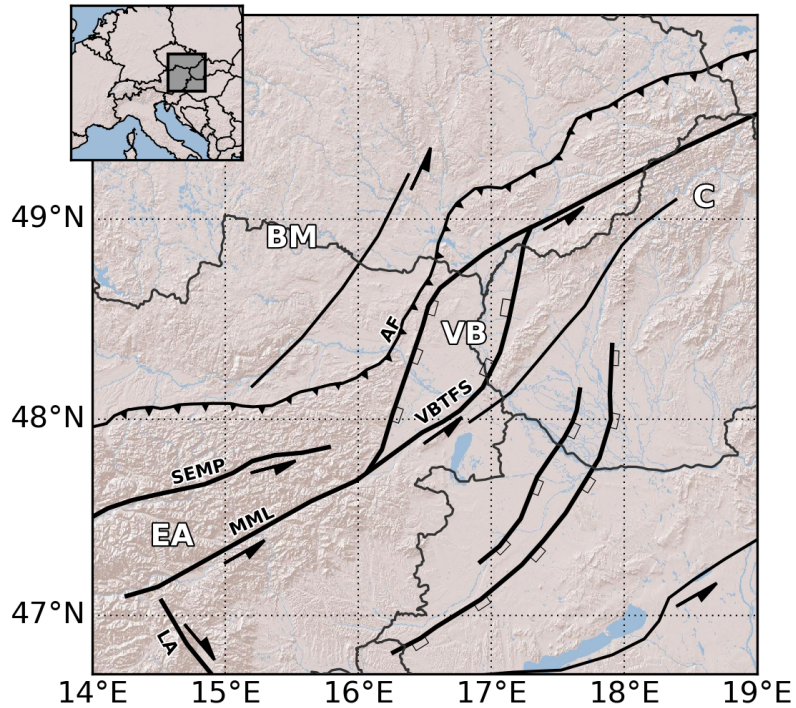


Figure 4.1: Tectonic sketch map of the study area illustrating the lateral extrusion of blocks (the southeastern half), accommodated by the major fault systems and subsequent formation of the Vienna Basin in the Alpine-Carpathian transition zone. Labelled fault systems: AF (Alpine Thrust-Front), LA (Lavanttal fault), MML (Mur-Mürz-Line), SEMP (Salzach-Ennstal-Mariazell-Puchberg fault), VBTFS (Vienna Basin Transfer Fault System). Labelled major geographical features: Bohemian Massif (BM), Carpathians (C), Eastern Alps (EA), Vienna Basin (VB). Faults are drawn after Peresson & Decker (1997).

The wider Vienna Basin region lies in the Alpine-Carpathian-Pannonian junction (ALCAPA), which is defined by its complex tectonic history. In brief, the N/S-collision of the Eurasian plate with the African and Adriatic plates resulted in the orogeny of the Alps (e.g. Schmid et al., 2004, and references therein). During the Miocene, this led to the lateral northeastwards extrusion of blocks

(Gutdeutsch & Aric, 1988; Ratschbacher et al., 1991b; Wölfle et al., 2011), accommodated by the major fault systems in the region (see Fig. 4.1). The sinistral Salzach-Ennstal-Mariazell-Puchberg fault (SEMP in Fig. 4.1), the Mur-Mürz Line (MML in Fig. 4.1), and the Vienna Basin Transfer Fault System (VBTFS in Fig. 4.1) mark the northern edge of extrusion. The dextral Periadriatic Line, and Lavanttal (LA in Fig. 4.1) fault systems delimit the Southern edge of extrusion (Gutdeutsch & Aric, 1988). As part of this extrusion, the Vienna Basin (VB in Fig. 4.1) formed as a thin-skinned pull-apart basin on top of thrust sheets and has undergone a complex history, including formation of the pull-apart structure, fault reactivation, graben formation, and normal faulting and rollover (Decker et al., 2005; Hölzel et al., 2010; Lee & Wagreich, 2016).

The paleo-stress orientation of maximum horizontal compressive stress σ_H that facilitated the formation of the structures appears to be dominantly oriented N/NNE in the last 17Ma (see Decker et al., 2005, and references therein). These conclusions are consistent with the block model proposed in Gutdeutsch & Aric (1988). Gerner et al. (1999), however, modelled the stress field using finite elements based on focal mechanisms, borehole breakouts and in-situ stress measurements. Their modelling suggests that the present-day σ_H -orientation in our study region is rotated to \sim NW, roughly normal to the Bohemian Massif (BM in Fig. 4.1). Similarly, Reinecker & Lenhardt (1999) argue that the BM acts as an indenter that results in a \sim NW σ_H -orientation in the eastern part of our study region. This would imply σ_H -orientations almost normal to the MML and nearby fault systems, raising the question why these faults are seismically active today. The focal mechanisms used in these studies (Gerner et al., 1999; Reinecker & Lenhardt, 1999) are mainly sinistral strike-slip mechanisms along the MML. In contrast, Bada et al. (2007) present a smoothed map of stress-field measurements with \sim N-orientations of σ_H in the West and North of our study area, and \sim NE-orientations in the East and South. These orientations are roughly normal to the Alps (instead of the BM) and are indeed compatible with the observed seismic activity along the MML. More recently, seismicity along the MML and in the region has been found to be a combination of strike-slip-, normal-, and thrust-faulting events (Brückl et al., 2014), which raises further questions about the present-day orientation of σ_H .

In this study, we investigate the azimuthal anisotropy of Rayleigh waves in the region to gain insight into the orientation of the stress-field and historical deformation. For this, we rely on two mechanisms that generate seismic anisotropy, and faster propagation of Rayleigh waves along σ_H : in the upper crust, cracks open in the direction perpendicular to σ_H , if the lowest compressive stress σ_3 is horizontal. Seismic waves travel faster along that axis, because fluid-filled cracks reduce seismic velocities in the direction normal to it (Nur, 1971). On the other hand, deformation can align crystals, especially in the lower crust (Barruol & Kern, 1996), which may cause seismic anisotropy. Because the Rayleigh waves we utilize are retrieved from ambient-noise cross-correlations, which means they represent estimated Green's Functions between receiver pairs (Nakata et al.,

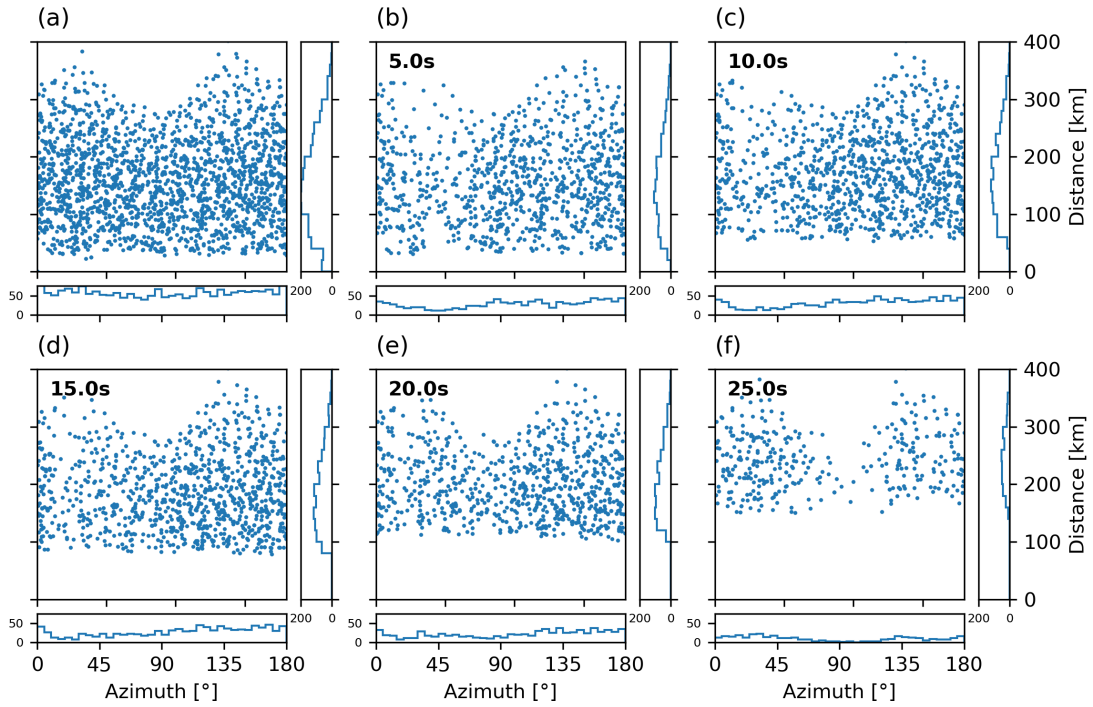


Figure 4.2: Inter-station geometry for all available station pairs (a) and the station pairs remaining after selection criteria applied during group velocity measurements for different periods (b - f). At shorter periods, slight bias of removal for inter-station orientations \sim NE due to decreased signal-to-noise-ratio of CCFs that are oriented normal to the main noise source direction. Increasing minimum inter-station distance with increasing period to due to the minimum-wavelength criterion, leading to strong azimuth-bias at 25s. For more details on the retrieval of group velocities, see Schippkus et al. (2018).

2019, and references therein), effects on the propagation speed are contained within the study area and they are sensitive to anisotropy in the area.

In the following, we describe our approach, the directional dependence of Rayleigh wave velocities, how they may relate to azimuthal anisotropy, and finally discuss limitations and advantages of our approach as well as our observations of the present-day stress field and historical deformation.

4.2 Data and Method

The data used in this study are the fundamental-mode Rayleigh-wave group velocities presented in Schippkus et al. (2018). Here, we analyze the measured group velocities u_m , predicted group velocities from the isotropic model u_p , and their residuals $u_r = u_p - u_m$. In Schippkus et al. (2018), inter-station group velocities are estimated from ambient-noise cross-correlation functions (CCFs) for 1,953 station pairs. 37,162 (46.4%) inter-station measurements pass the quality- and statistics-based selection procedure, with the number of remaining measurements depending on period (Fig. 4.2). These measurements were previously used to compute an isotropic shear-velocity model of the region (Schippkus et al., 2018). The inter-station paths remaining after selection show no significant bias in available azimuth for the periods discussed later in this study (5s - 20s, Fig. 4.2). At longer periods ($T > 20$ s), the criterion that limits minimum inter-station distance results in a skewed distribution in azimuth, due to only certain azimuths being available for long inter-station distances (Fig. 4.2f). We therefore refrain from interpreting those periods in greater detail.

We parametrize azimuthal anisotropy of Rayleigh wave group velocities following Smith & Dahmen (1973) by

$$u(\Theta) = u_0 + A \cdot \cos(2(\Theta - \phi_2)) + B \cdot \cos(4(\Theta - \phi_4)),$$

with the isotropic velocity u_0 , the amplitude A and phase shift ϕ_2 of the 2Θ -term, and the amplitude B and phase shift ϕ_4 of the 4Θ -term. To stabilize the fitting, we use the medians of azimuth-binned group-velocities (5°-bins) and weigh them by their respective standard-deviations (see Fig. C.1). While we account for the 4Θ -term during the curve-fit (Fig. C.2), in this study we aim to only interpret the 2Θ -term.

To learn about the spatial distribution of A and fast orientation ϕ_2 in the study area, we regionalize the approach, i.e., we estimate the azimuthal anisotropy in smaller sub-areas. For this, an evenly-spaced grid (in latitude and longitude) of overlapping cells is defined across the region. For each of those cells, we estimate the directional dependence, as described above, of those inter-station paths that cross the cell. The median for each azimuth-bin is measured from inter-station group velocities weighted by their path-length inside the cell. More precisely, for each of those cells, all 5km-cells (from the parametrization of the isotropic inversion of Schippkus et al. (2018)) contained within the large cell are checked for crossing paths and these paths' group velocities and azimuths are taken as data points. Therefore, paths that cross n 5km-cells within a large cell result in n velocity-azimuth data points for that cell, i.e., the velocity medians are weighted approximately by their path-length within the larger cell.

4.3 Results

In the following, we present our findings on the directional dependence of measured group velocities (4.3.1), of modelled group velocities from the isotropic velocity model (4.3.2), and of group velocity residuals (4.3.3).

4.3.1 Measured Group Velocities

The directional dependence of group velocities, measured on all paths for a given period (Fig. 4.3a), shows that fast orientations vary from -5° to 50° (S-N to SSW-NNE), depending on period. In the following, we will refer to them only by one direction, in this case N to NNE. The amplitude of the directional variation is larger for shorter periods ($\sim 6\%$ at 5s), decreasing with period and reaching a plateau at around 10s, where lower amplitudes of 1% - 2% are observed. At periods larger than 20s, the amplitude increases again up to $\sim 4\%$. All shown error bars indicate one standard deviation. There is an interdependence of errors in direction and amplitude with the amplitude A itself. The lower the amplitude A , the less-well-determined A and ϕ_2 are. This leads to very high errors ($\pm 3\%$) for amplitudes $< 2\%$, meaning that no directional dependence ($A = 0$) of group velocities is consistent with the observations at least for some periods (10s - 20s, Fig. 4.3a).

We regionalize the directional dependence, as described above, of the measured group velocities for 5s (Fig. 4.4a) and 20s (Fig. 4.4e) to represent the shallow (5s) and mid-crustal structure (20s). We find that these periods show distinctly different behavior in our approach that is representative for the entire period-range. Here, we choose to parametrize the grid-cells with 2° width and height, and 85% overlap. This dense distribution of cells is used to more clearly illustrate the observations we make and support the arguments we bring forward. For the purpose of discussion, however, we will later apply a coarser grid to prevent overinterpretation given the limitations in lateral resolution of our approach. The most striking feature of the regionalized fast orientations is that they seem to form a tangential shape around the southeastern part at 5s (Fig. 4.4a). The 'center' of this shape is roughly collocated with the major sedimentary basins in the region (VB and Little Hungarian Plain (LHP)), marked by the two low-velocity features in the isotropic model of Schippkus et al. (2018) (Fig. 4.4d). For a given 2° -cell, the paths across sedimentary basins are generally slower than paths across crystalline basement rocks of the BM. This results in a pattern where fast orientations are oriented tangentially around the low-velocity anomalies. The same effect is visible for 20s (Fig. 4.4e) for which only the VB and underlying structure remains as a dominant low-velocity anomaly (Fig. 4.4h), resulting in a smaller radius of the tangential feature (Fig. 4.4e). These observations suggest that the regionalized fast orientations determined from measured inter-station group-velocities may be dominated by isotropic effects - the heterogeneous

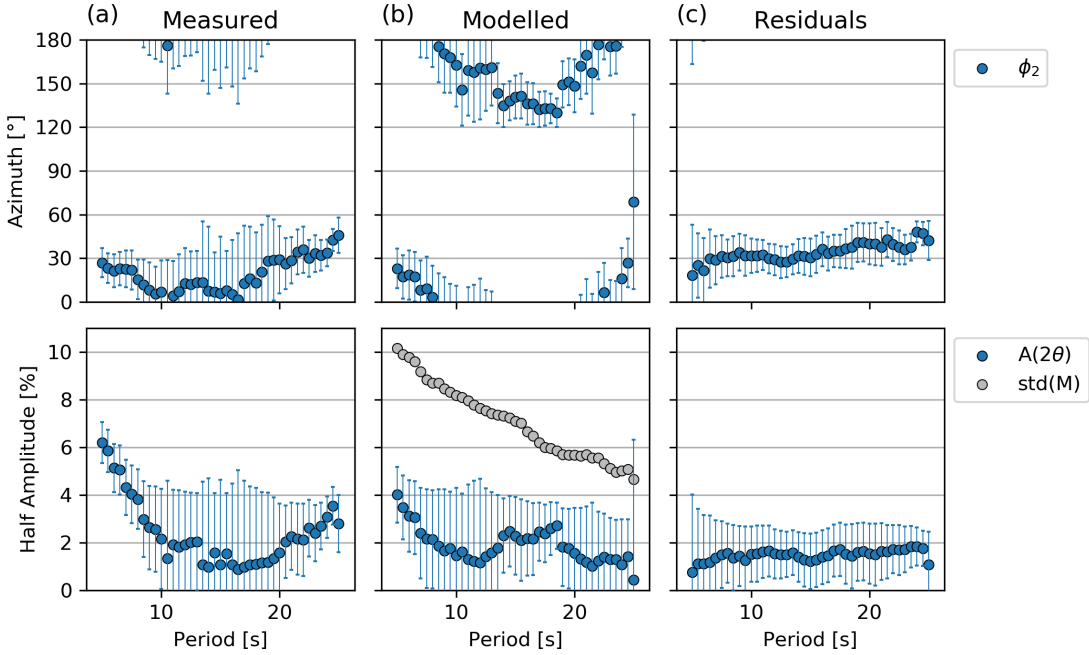


Figure 4.3: Directional dependence (2Θ -terms) of group velocities for measured (a), modelled (b), and residual (c) group velocities. a) Measured group velocities show N to NNE fast directions (ϕ_2) for all periods. Amplitude decreases with period until plateau is reached. b) Group velocities modelled from the isotropic velocity model also show directional dependence. Similar trend in amplitude as (a), but at lower magnitude. Decreasing amplitude of velocity model (represented by standard deviation $\text{std}(M)$, grey points) with period may explain decreasing amplitude of the 2Θ -term. c) Residual group velocities show stable NNE fast orientation that rotates slightly towards E with increasing period. Lower, but stable amplitudes for all periods around 1-2%.

distribution of velocities - rather than anisotropic structure.

4.3.2 Modelled Group Velocities

To test this hypothesis, we determine the directional dependence of group velocities as predicted by the isotropic velocity model (Schippkus et al., 2018), first on the entire region. We find that the isotropic model also predicts a directional dependence of Rayleigh wave velocities (Fig. 4.3b), although different from the measured group velocities (Fig. 4.3a). Fast orientations are varying over a larger range (-50° to 65°) and amplitudes are generally lower, especially at short ($5\text{s} - 10\text{s}$) and

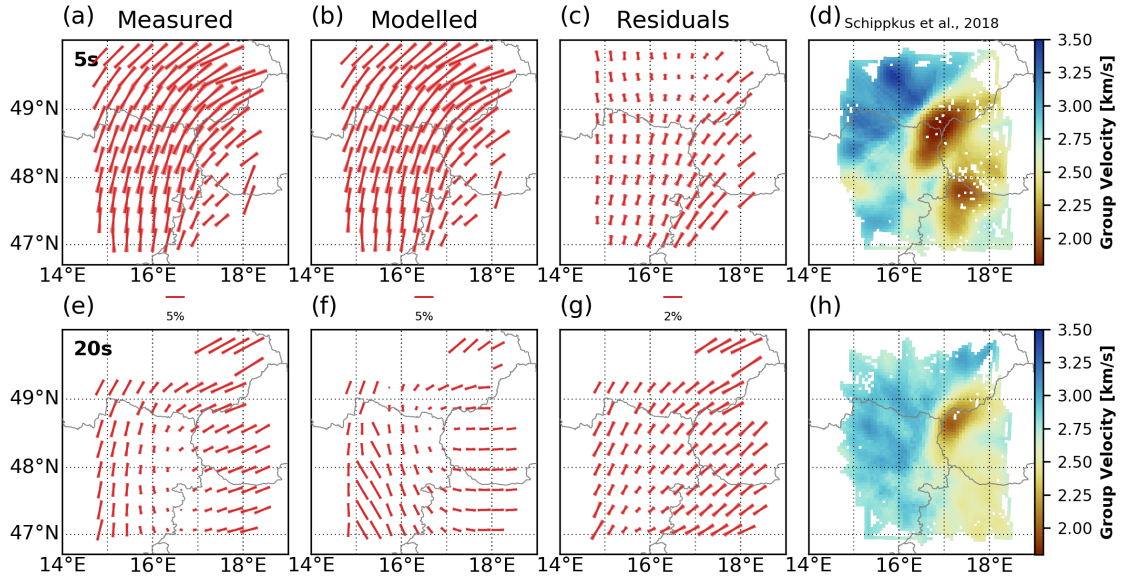


Figure 4.4: Regionalization of fast directions for measured (a, e), modelled (b, f), and residual group velocities (c, g) in a grid of 2° -cells, overlapping with 85% at 5s (top row) and 20s (bottom row). The group velocity maps (d, h) of Schippkus et al. (2018) allow to interpret the observed features. Fast directions (ϕ_2) estimated from measured and modelled group velocities show a very similar pattern. Striking is the tangential alignment of fast directions around the major low-velocity anomalies, explained by isotropic effects (fast paths within a cell are those that do not cross the low-velocity anomalies). Locally, amplitudes can be considerable ($A \sim 10\%$). Residual group velocities at 5s (c) show a smoothly varying distribution of fast directions, although fast directions in the Southeast that are similar to both a) and b) remain. At 20s (g), fast directions from residuals are universally aligned \sim NE.

long periods (20s – 25s). At intermediate periods (10s – 20s), a slight increase in amplitude is observed, corresponding to a change in fast orientation to NW. However, an amplitude decrease with period for short periods (5s – 10s) is present for both the measured (Fig. 4.3a) and predicted group velocities (Fig. 4.3b). The standard deviation of the isotropic velocity model $\text{std}(M)$ (Fig. 4.3b) suggests that the decrease of amplitude with period may be partly explained by the decreasing model amplitude. The amplitude of directional dependence may be influenced by the velocity-contrasts within the model, pointing again to isotropic effects rather than anisotropic structure.

The regionalized fast orientations as estimated from modelled group velocities (Fig. 4.4b, f) show striking similarity with those estimated from measured group velocities (Fig. 4.4a, e), especially for 5s (Fig. 4.4a, b). At 20s (Fig. 4.4f, e), some differences are visible, but the overall pattern

is very similar, with the main feature - fast orientations tangential to the low-velocity anomalies - well visible. Our hypothesis that the distinct pattern of fast orientations is largely explained by the heterogeneity of isotropic velocities seems to hold, given how closely the patterns from measured and modelled group velocities resemble each other.

4.3.3 Group Velocity Residuals

As shown above, the fast orientations estimated from measured group velocities appear to be dominated by isotropic effects. Therefore, we analyze the residuals after isotropic inversion, i.e., the difference of measured and modelled group velocities, to extract azimuthal anisotropy. These residuals contain only effects that the isotropic model cannot explain, i.e., errors in data (e.g., inaccurate measurements), errors in the model (e.g., invalid assumptions, smoothing), and effects of the anisotropic structure, the target of our study. The group velocity residuals (Fig. 4.3c) show a stable NNE ($\sim 30^\circ$) fast orientation ϕ_2 that rotates slightly towards East (from 25° to 50°) with increasing period. The amplitude A is relatively stable around 1.5% and no longer exhibits a decreasing trend.

The regionalized fast orientations of residual group velocities at 5s (Fig. 4.4c) show a distribution that still appears to contain some previously-observed features, but it is overall very different from the patterns observed for measured (Fig. 4.4a) and modelled (Fig. 4.4b) velocities. Most notably, the NE ϕ_2 -orientation at the Southeastern edge, present for both - measured and modelled - group velocities (Fig. 4.4a, b), remains consistent, although with reduced amplitude. The clear tangential pattern observed previously (Fig. 4.4a, b) is no longer present and instead a spatially-coherent rotation of the fast orientation (N to NE) from West to East is visible. At 20s (Fig. 4.4g), the fast orientations are spatially coherent NE over the entire region with only minimal variation. Still, a very slight tangential trend appears to be present around the low-velocity anomaly in the NE, but the effect is negligible compared to previous observations (Fig. 4.4a, b, e, and f).

4.3.4 Impact of smoothing constraint

As mentioned above, the smoothing constraint during the isotropic inversion may propagate isotropic effects into the residuals. Because we have direct control over this parameter, we can test how it may bias our measurements. For this, we invert the measured group velocities with weaker smoothing and compare to our results with stronger smoothing (Fig. 4.5). Each panel (a-d) shows the regionalized fast orientation measured from group-velocity residuals on the left. On the right, we show the inverted group-velocity residuals, where the residuals are used as input in a second isotropic inversion to regionalize them. The second inversion is parametrized the same as the

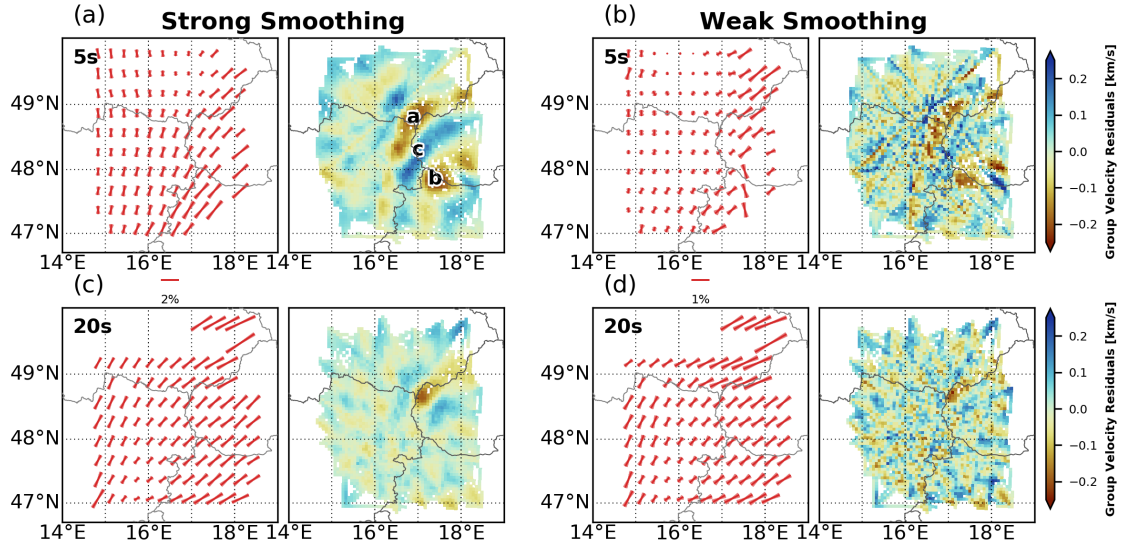


Figure 4.5: Impact of the smoothing constraint applied during isotropic inversion on retrieved azimuthal anisotropy from group-velocity residuals. Each panel (a - d) shows the regionalization of anisotropy (left) and the inverted group velocity residuals, in a second isotropic inversion. Left: Results for the stronger smoothing constraint used in Schippkus et al. (2018) ($\alpha = 35$). Right: Results for a weaker smoothing constraint ($\alpha = 10$). With stronger smoothing, isotropic velocity structure carries over into the residuals (a, c) and may continue to bias estimation of anisotropy. Distribution of residuals with weaker smoothing (b, d) appears more random and less representative of isotropic structure, although some influence remains. At 5s, the smoothing constraint has strong impact on retrieved anisotropy. At 20s, the smoothing has only minimal impact on the retrieved directions. Note the different scale for strong and weak smoothing, and that the amplitude of anisotropy decreases with weaker smoothing.

first inversion. This allows insight into whether the residuals are randomly distributed or heavily influenced by the isotropic velocity structure.

With stronger smoothing, as used in this study and Schippkus et al. (2018) (smoothing factor $\alpha = 35$), the model does not fully explain the measured group velocities. The model velocities in the VB and LHP are not low enough to fully account for the measured velocities (a, b in Fig. 4.5a). Similarly, the model velocities in between the basins are too low to explain the data (c in Fig. 4.5a). Here, the Little Carpathians separate the two basins. This mountain range is geographically too narrow to be properly represented with the chosen smoothing constraint. This suggests that isotropic effects do indeed propagate into the residuals. Isotropic inversion with a weaker smoothing constraint ($\alpha = 10$, Fig. 4.5b) results in a more random distribution of residuals. They still contain isotropic effects, but the effects are no longer as dominant in the model. The

retrieved azimuthal anisotropy from those residuals is generally much weaker and constrained more poorly (Fig. 4.5b) and may locally even change direction dramatically. Note that the amplitude of the directional dependence decreases with weaker smoothing, because a weaker smoothing constraint results in a better data-fit and therefore lower residuals. The fast orientations (Fig. 4.5b), however, still appear to be mostly consistent with the findings for stronger smoothing (Fig. 4.5a).

At 20s, similar observations can be made. The model velocities near the VB are also too low to fully explain the data (Fig. 4.5c) and with weaker smoothing the residual distribution appears more random (Fig. 4.5d). However, the isotropic effects are not as impactful on the regionalized fast orientations at 20s as compared to 5s. This is evident by the minimal effect of the smoothing constraint on the retrieved fast orientations (Fig. 4.5c, d). Importantly, the tangential-trend-argument mentioned above does not explain the consistently observed NE fast orientations across the entire region (Fig. 4.5c, d).

4.4 Discussion

We split the discussion into two parts: a methodological and a structural part. In the methodological part, we aim to discuss the assumptions, robustness, and limitations of our approach in order to argue that we do indeed observe structural anisotropy in residual group velocities. In the structural part, we discuss our findings in the geological and tectonic context.

4.4.1 Methodology

The observed anisotropy on the order of a few percent raises the question about the accuracy of our travel-time measurements and potential biases therein. Errors on this order are negligible for interpreting tomographic images of the crust (Schippkus et al., 2018), but this is still to be seen in the context of anisotropy.

A non-isotropic distribution of noise sources might, in extreme cases, introduce travel-time errors on the order of a few percent in Green's functions estimated from cross-correlations of the ambient seismic field (Tsai, 2009; Froment et al., 2010). Froment et al. (2010) find faster velocities for station pairs that are aligned roughly normal to the dominant noise source direction. However, if the wavefield is sufficiently scattered, i.e., if not ballistic waves are cross-correlated but their coda, this error is reduced to almost zero (Froment et al., 2010). The primary (~ 14 s) and secondary (~ 7 s) microseism peaks are generated by different mechanisms (Longuet-Higgins, 1950; Hasselmann, 1963) and originate at different locations (Juretzek & Hadzioannou, 2016), resulting in a less-well-defined dominant noise source direction. Furthermore, we use data recorded over

2 years to retrieve estimated Green's Functions, accounting for different dominant noise source regimes, which are different in winter and summer months. Therefore, in our case, the wavefield likely consists of a variety of ballistic and scattered waves arriving from different directions. We believe that this alleviates potential travel-time errors.

This study is based on group velocities measured on estimated Green's Functions that contain Rayleigh waves. Group-velocity measurements are not very precise, because the peak of the envelope of a filtered waveform is picked as an estimate for group-velocity (Dziewonski et al., 1969). The distribution of residuals in Figure C.1 indicates that measurement errors give rise to velocity errors that are not larger than 0.2km/s, and probably smaller than that (since unmodeled effects are also included). One might think that longer periods would be associated with less precise measurements, due to the filter-width increase with wavelength. Figure C.1 suggests though that this does not seem to be the case. Overall, the uncertainties are not large.

Some of the errors that enter prior to the retrieval of residual group velocities are on the order of the measured effect of a few percent. To test for the significance of our results, we model the worst-case scenario: What if the combination of all errors results in entirely random group-velocity residuals that are no longer representative of any physical feature? For this, we compute 10,000 sets of randomly distributed inter-station residuals for each period, using the available inter-station geometry per period and measure azimuthal anisotropy on them (Fig. C.3). We find that our results, although small in amplitude and subject to potentially significant errors, are extremely unlikely to be a result of chance, especially given the consistency of our results over the period range. This gives more credibility to our results and agrees with our previous considerations that the errors we introduce are likely smaller than the amplitude of anisotropy A . This approach does not account for the propagation of physical effects other than from anisotropic structure into the residuals, though. Our tests on the impact of the smoothing constraint (Fig. 4.5) should give confidence that the isotropic velocity structure does not heavily influence the retrieved fast orientations, at least for periods longer than 5s.

The interpretation of group velocity residuals in terms of azimuthal anisotropy relies not only on negligible propagation of isotropic effects into the residuals, but also on a purely isotropic model that does not already account for anisotropic effects. As discussed in Schippkus et al. (2018), we believe this model is a good representation of the isotropic velocity structure of the wider Vienna Basin region. In addition to the arguments presented in Schippkus et al. (2018), which include surface geology, velocity contrasts at known faults, and gravitational anomalies to confirm the lateral extent of the observed features, as well as ground truth from boreholes and refraction profiles to confirm the depth-extent, the refraction profile 7R (Dvorak et al., 1990) is also in good agreement with the imaged deep low-velocity anomaly in the Vienna Basin. Therefore, we believe that there is no significant influence of anisotropy on the isotropic velocity model.

In recent literature, it is common practice to interpret azimuthal anisotropy directly from measured group velocities (e.g. Mordret et al., 2013b; Zigone et al., 2015; Taylor et al., 2019). In this study, we show that interpretation of measured group velocities in terms of anisotropic structure can be misleading, as the heterogeneities of the isotropic velocity structure can dominate the apparent fast orientations. This can occur even with a relatively homogeneous distribution of path geometries (Fig. 4.2). We suggest that a simple 2-step approach of isotropic inversion and interpretation of residuals will result in more confident estimates of anisotropic structure.

4.4.2 Geological and Tectonic Context

These arguments lead us to conclude that the group velocity residuals contain mainly anisotropic effects (and not errors or biases), and they can thus be interpreted in terms of structure and tectonics.

In the study area, most of the major fault systems (SEMP, MML, VBTFS, LA, see Fig. 4.1) accommodate the lateral extrusion of blocks during the Miocene (Gutdeutsch & Aric, 1988; Ratschbacher et al., 1991b), a consequence of the Africa-Eurasia collision and the Alpine orogeny (e.g. Schmid et al., 2004, and references therein). These faults and with them the extruded blocks are oriented towards NE, roughly matching the fast orientations we observe on the group velocity residuals across all available periods (Figs. 4.3c, 4.4, 4.6). We notice an overall rotation to more eastern orientations at longer periods. The most likely explanation for the consistent change in fast orientation towards NE with increasing period (Figs. 4.3c, 4.4, 4.6) is the depth sensitivity of Rayleigh waves (Fig. 4.7), which all measurements are based on. The two periods we will discuss here (5s and 20s, Fig. 3.6) have their maximum sensitivity at depths of \sim 2km, and \sim 15km, respectively (Fig. 4.7). The full range of studied periods are presented in Figure C.4. Seismic anisotropy in the crust generally consists of two parts, a) stress-related and b) texture-related anisotropy (Fig. 4.8; Kern (1990)). The effect of crack-induced (i.e., stress-related) anisotropy is confined to the topmost kilometers in the crust (see also Nur & Simmons, 1969), while texture-related anisotropy can occur at any depth. Whether anisotropy appears in seismological observations depends largely on processes that align the microscopic anisotropy at spatial scales comparable to seismic wavelengths (kilometers to tens of kilometers). There are two candidates for such aligning processes, a) cracks in the topmost kilometers may be aligned by the tectonic stress field, and b) shear in the lower crust may align minerals spatially. Crack-related anisotropy is therefore likely to appear in measurements for the shorter periods, and (especially around 5s), making it possible to characterize the present-day stress-field acting within the topmost kilometers. This has been confirmed by borehole studies (e.g. Zinke & Zoback, 2000). If the measurements do not pertain to the vicinity of major faults, seismic fast orientations then directly give the orientation of maximum horizontal

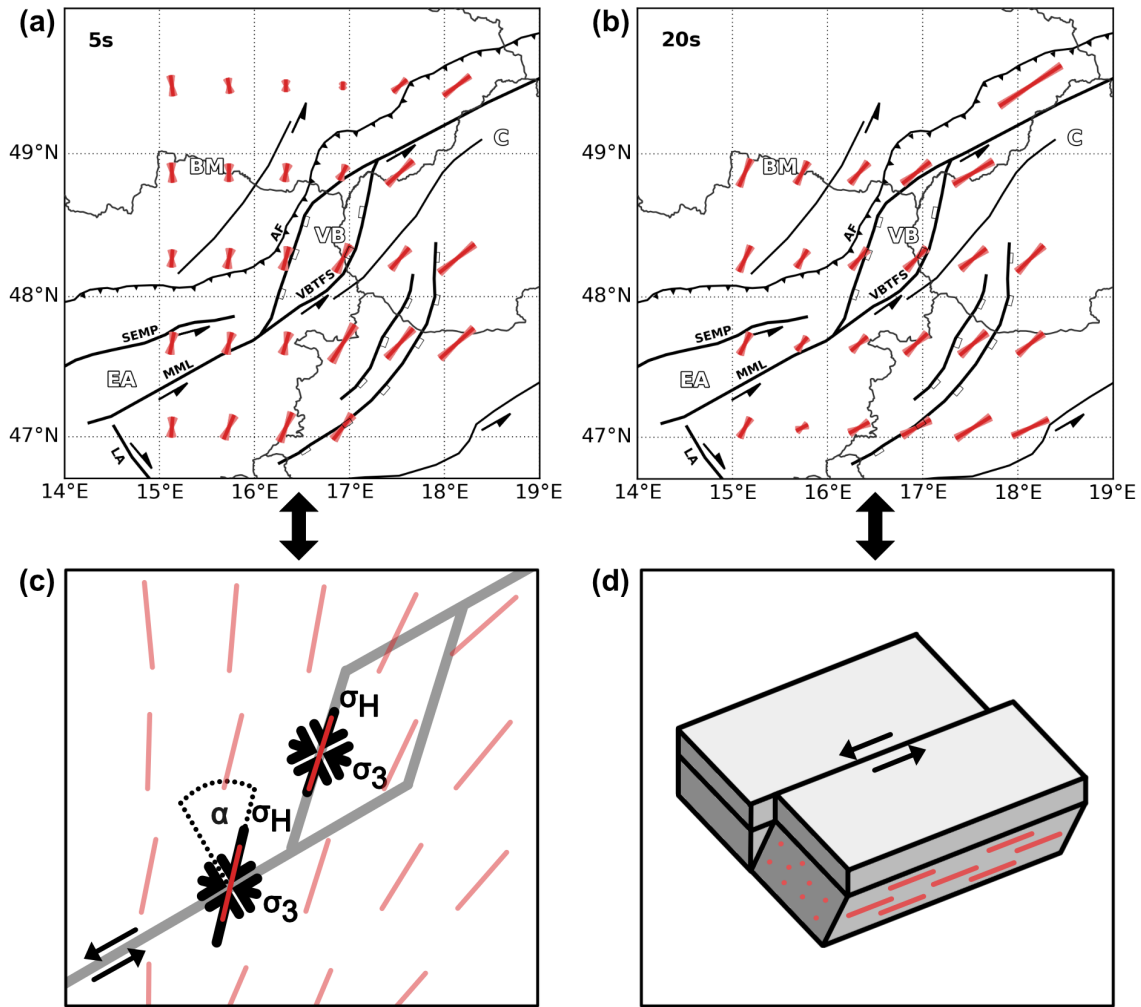


Figure 4.6: Regionalized azimuthal anisotropy of Rayleigh waves (a, b) and their shallow (c) and mid-crustal (d) interpretations. a) At 5s - sensitive to the top few kilometers of the crust - fast orientations align with the orientation of the maximum horizontal compressive stress σ_H , due to formation of cracks. b) At 20s - sensitive to mid-crustal depths - there is a rotation of fast orientation towards northeast, almost parallel to the faults that accommodates lateral extrusion of blocks. c) Near the MML, fast orientations ϕ_2 are oriented with 30-45 degrees to the fault, which is compatible (for σ_H) with reactivation of slightly-weakened rocks (see Fig. 4.9). Near the normal-faults of the VBTFS ϕ_2 are oriented essentially parallel to them. The horizontal principal stress are indicated for both the strike-slip ($\sigma_H = \sigma_1$) and the normal faults ($\sigma_H = \sigma_2$). d) Mid-crustal deformation due to lateral extrusion results in alignment of crystals along in the direction of relative motion, leading to fast orientations along the same axis.

compressive stress σ_H (Boness & Zoback, 2006). Longer periods (more than ~ 10 s), on the other hand, are no longer sensitive to cracks, as potential cracks are likely to be closed due to higher lithostatic pressure at depths larger than a few kilometers (Fig. 4.8). The longer periods are most likely sensitive to the alignment of crystals in the deeper crust during long periods of deformation (Barruol & Kern, 1996), i.e. the deformation associated with the deeper extent of the faults and the lateral extrusion of blocks. Thus Rayleigh waves can in principle distinguish crack-induced anisotropy from that created by deeper crustal deformation. This allows insight into each of the two processes separately.

In the very shallow crust (Fig. 4.6a), two regions of common fast orientation ϕ_2 can be distinguished. In the West, and especially to the West of the Vienna Basin (VB), fast orientations align along $\sim N$. To the east, roughly south of the AF (Fig. 4.6a) fast orientations are rotated towards NE. Some of these ϕ_2 -orientations agree with the stress-field orientations of Reinecker & Lenhardt (1999), especially in the region around the SEMP and the western part of the MML, the lower-left part of Figure 4.6a. They are also consistent in tendency in the Bohemian Massif, with an observed rotation to NNW. The agreement is lower for the Vienna Basin area, the eastern MML, and VBTFS, where Reinecker & Lenhardt (1999) also show NNW orientations. There, the stress-field orientations they report are however almost normal to the eastern MML, inconsistent with its seismic activity. They correspond to angles of the stress-field with MML of around $\alpha \simeq 20^\circ$, requiring that the fault moves despite rather low values of the coefficient of internal friction (see Fig. 4.9). The results in Reinecker & Lenhardt (1999) are based on individual focal mechanisms, which scattered strongly around the (known) orientation of the fault.

Bada et al. (1998) and Gerner et al. (1999) have investigated the stress field in a larger area including the VB region, but their observations do not seem to obey these constraints. There is also a large mismatch between their modeled and the observed stress-field orientations in that region. Stress data from the oil industry scatter a lot (and possibly vary spatially), but they seem to often show $\sim N-S$ orientations of σ_H (e.g. Marsch et al., 1990; Decker et al., 2005).

The stress-field orientations reported in Bada et al. (2007), however, are consistent with our results, especially in the Western and Southern parts of our study area. In the Northeast, the orientations do not agree; they are almost perpendicular to each other. There, at the edge of our study area, our results are based only on few data (as can be seen by unresolved pixels in the shear-velocity model in Figure 4.4d), giving a possible explanation for the mismatch. The results of Bada et al. (2007) are based on a smoothed map of pointwise measurements of the stress-field orientation over a larger region. In the wider Vienna Basin region, these measurements scatter considerably and are sparse (e.g., Bada et al., 2007; Heidbach et al., 2018) and the recently increased number of measurements on the broader regional scale may prevent over-interpretation of individual measurements.

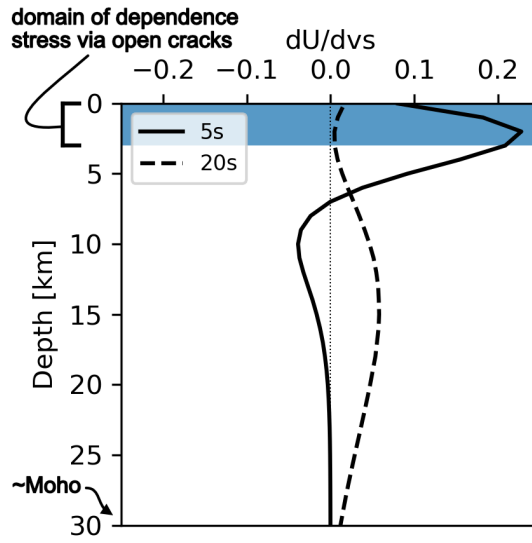


Figure 4.7: Group-velocity sensitivity to shear-velocity structure for the mean velocity model of the region (Schippkus et al., 2018). The period range in this study probes the crustal structure, with maxima at different depths. Periods of 5s - 15s are most sensitive to shallow crustal structure (top 10km), whereas periods $T > 15s$ are more sensitive to the deeper crustal structure (below 10km).

Our results show seismic fast orientations to have angles with the MML α between 30 and 45 degrees (Figs. 4.6a, c). These are reasonable values for an “actively moving” fault (see Fig. 4.9), which is characterized by the occurrence of earthquakes (or fault creep). Near the normal-fault sides of the VBTFS, the fast orientations are essentially parallel to the faults, which is not surprising, if the fast orientation ϕ_2 indeed represents σ_H (as shown by Zinke & Zoback, 2000). These observations are illustrated in Figure 4.6c, where we present a schematic view of how the fast orientations ϕ_2 (and thus orientation of σ_H) likely relate to the geometry and different faulting regimes of the MML and VBTFS.

These considerations suggest that the ϕ_2 -orientations we find do indeed indicate the orientations of σ_H , and with that a more coherent orientation of σ_H NNE-SSW across the region (Figs. 4.6a, c) as compared to the lateral change of σ_H reported by Reinecker & Lenhardt (1999). This is of much interest especially for an area like the wider Vienna Basin region, where many aspects of the stress-field are not well-known. Our reported σ_H -orientations are consistent with the geometry of the different fault systems (see Fig. 4.6c), even though the type of stress-field regime (strike-slip-, normal- or reverse-faulting) appears to vary at close spatial distance, indicated by the complexity of faulting in the area. A simple schematic model like the one in Figure 4.6c cannot – and is not intended to – fully capture the spatial complexity nor the necessary time-dependent

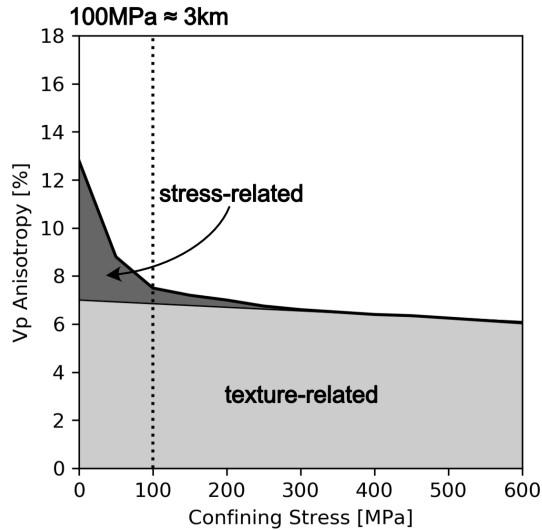


Figure 4.8: General dependence of seismic anisotropy on confining pressure (redrawn after Kern, 1990). There are two types of seismic anisotropy, stress-related versus texture-related. Stress-related anisotropy is due to the existence of open cracks, and it is thus confined thought to be confined to the topmost kilometers (100MPa confining stress corresponds roughly to 3km depth).

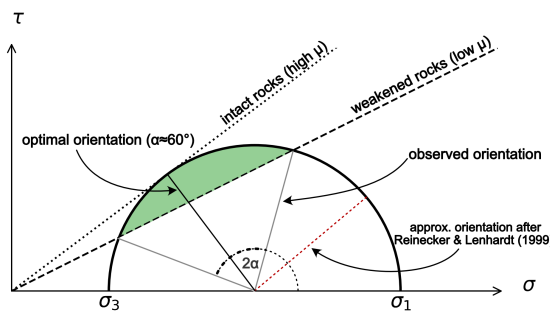


Figure 4.9: Schematic Mohr's circle to illustrate the interaction between stress-field and seismic activity at the MML fault. The repeatedly ruptured and therefore weakened rocks of the MML likely have reduced coefficients of internal friction μ . This allows a wider range of rupture plane orientations to be active (green area), beyond optimally-oriented faults. Therefore, the the fast orientations (and hence the stress-field) we observe in this study is compatible with the recent seismic activity along the MML, one of Austria's seismically most active faults.

deformation. Some of this complexity (or time-dependence) may however be reflected by indications of a vertical rotation of σ_H in the crystalline basement compared to the overlying rocks across individual faults such as the Steinberg fault (e.g. Decker et al., 2005).

From Figure 4.6a we further note that amplitudes of azimuthal anisotropy are smaller in the BM and higher to the East, in the sedimentary basins (VB, LHP). However, at this point it seems beyond our goals to speculate about whether that difference in amplitude could be explained by the difference in susceptibility of crystalline and sedimentary rocks to crack-formation, or the increased stresses in the East due to the stronger tectonic deformation in that region (e.g., ongoing influence of lateral extrusion).

To understand the general characteristics of the stress field, it appears useful to look at the larger regional scale. Reinecker et al. (2010) and Heidbach et al. (2018) show highly consistent orientations of $\sigma_H \sim N-S$ in the Molasse region that rotate towards west into a NNW-SSE orientation - suggesting an important role of the gravitational potential of the Alps. Toward the East, σ_H rotates into NNE-SSW orientations, as reported in Reinecker & Lenhardt (1999) at least for Upper Austria. This study suggests that the stress field continues its consistent trend even further to the East towards the eastern edge of the Alps and into the Alpine-Carpathian transition zone, which supports the strong impact of gravitational forces to the regional stress field.

In the deeper crust (Fig. 4.6b), we find fast orientations generally towards NE. These orientations inside and at the edge of the extruded blocks are almost parallel to the major sinistral strike-slip fault systems (SEMP, MML, VBTFS in Figs. 4.1, 4.6). To the North of these fault systems, ~NNE fast orientation seem to be dominant. At the larger depths to which the Rayleigh waves are sensitive at these periods, this anisotropy could very-well be caused by crystal alignment associated with crustal deformation (e.g. Barruol & Kern, 1996). During the lateral extrusion over a long period of time (at least since the mid-Miocene) the crystalline structure of the deeper basement rocks likely aligned along this axis, resulting in the fast orientation of Rayleigh waves in the direction of relative motion with respect to the underlying medium. This would imply that the extrusion is at least partly accommodated at crustal depths, and that we're observing its effect in the seismic recordings. We show a schematic view (Fig. 4.6d) to illustrate how the lateral extrusion may induce these fast orientations, whereas the shallow crust is more rigid and largely unaffected by this effect. This explains why the anisotropy in the deeper crust is generally stronger to the SE of the Southern Vienna Basin Fault.

4.5 Conclusions

We have demonstrated that fast orientations of ambient-noise-derived Rayleigh waves can provide important information on the crustal stress field, at different depths, where either stress field or

deformation-related crystal alignment strongly affect seismic anisotropy. A prerequisite is that the isotropic-anisotropic tradeoff is studied carefully, though. We find that interpretation of measured Rayleigh wave group velocities in terms of anisotropic structure can be heavily biased by isotropic structure, i.e., the heterogeneous distribution of velocities. However, velocity residuals after isotropic inversion appear to contain mostly anisotropic effects and allow to study the anisotropic structure. Seismic anisotropy in the Vienna Basin area in the topmost kilometers of the crust is apparently controlled by the regional stress field, via crack-induced anisotropy. Fast orientations can be interpreted as orientations of σ_H . This is corroborated by the active faults in the area whose orientation agrees closely with what is expected from the stress-field orientation. At deeper levels in the crust, anisotropy is rather controlled by crystal alignment by deformation due to faults and the lateral extrusion in the area. Orientations agree closely with what is expected from deformation.

Acknowledgements

Part of this work was performed using funding from the Austrian Science Fund (FWF): Projects 26391 and 30707. Data were acquired using the ORFEUS web services. The software used in this study was kindly provided by Krischer et al. (2015) and Herrmann (2013). The data used in this study are provided by the operators of the national seismic networks (Czech Regional Seismic Network, 1973; Austrian Seismic Network, 1987; Hungarian National Seismological Network, 1992; Seismic Network of the Republic of Slovenia, 2004; National Network of Seismic Stations of Slovakia, 2004) and the members of the AlpArray Working Group (AlpArray Seismic Network, 2015). We thank the AlpArray Seismic Network Team: György HETÉNYI, Rafael ABREU, Ivo ALLEGRETTI, Maria-Theresia APOLONER, Coralie AUBERT, Simon BESANÇON, Maxime BÉS DE BERC, Götz BOKELMANN, Didier BRUNEL, Marco CAPELLO, Martina ČARMAN, Adriano CAVALIERE, Jérôme CHÉZE, Claudio CHIARABBA, John CLINTON, Glenn COUGOULAT, Wayne C. CRAWFORD, Luigia CRISTIANO, Tibor CZIFRA, Ezio D'ALEMA, Stefania DANESI, Romuald DANIEL, Anke DANNOWSKI, Iva DASOVIĆ, Anne DESCHAMPS, Jean-Xavier DESSA, Cécile DOUBRE, Sven EGDORF, ETHZ-SED Electronics Lab, Tomislav FIKET, Kasper FISCHER, Wolfgang FRIEDERICH, Florian FUCHS, Sigward FUNKE, Domenico GIARDINI, Aladino GOVONI, Zoltán GRÁCZER, Gidera GRÖSCHL, Stefan HEIMERS, Ben HEIT, Davorka HERAK, Marijan HERAK, Johann HUBER, Dejan JARIĆ, Petr JEDLIČKA, Yan JIA, Hélène JUND, Edi KISSLING, Stefan KLINGEN, Bernhard KLOTZ, Petr KOLÍNSKÝ, Heidrun KOPP, Michael KORN, Josef KOTEK, Lothar KÜHNE, Krešo KUK, Dietrich LANGE, Jürgen LOOS, Sara LOVATI, Deny MALENGROS, Lucia MARGHERITI, Christophe MARON, Xavier MARTIN, Marco MASSA, Francesco MAZZARINI, Thomas MEIER, Laurent MÉTRAL, Irene MOLINARI, Milena MORETTI, Helena MUNZAROVÁ, Anna NARDI, Jurij PAHOR, Anne PAUL, Catherine PÉQUEGNAT, Daniel PETERSEN, Damiano PESARESI, Davide PICCININI, Claudia PIROMALLO, Thomas PLENEFISCH, Jaroslava PLOMEROVÁ, Silvia PONDRELLI, Snježan PREVOLNIK, Roman RACINE, Marc RÉGNIER, Miriam REISS, Joachim RITTER, Georg RÜMPKER, Simone SALIMBENI, Marco SANTULIN, Werner SCHERER, Sven SCHIPPKUS, Detlef SCHULTE-KORTNACK, Vesna ŠIPKA, Stefano SOLARINO, Daniele SPALAROSSA, Kathrin SPIEKER, Josip STIPČEVIĆ, Angelo STROLLO, Bálint SÜLE, Gyöngyvér SZANYI, Eszter SZÚCS, Christine THOMAS, Martin THORWART, Frederik TILMANN, Stefan UEDING, Massimiliano VALLOCCHIA, Luděk VEC-

SEY, René VOIGT, Joachim WASSERMANN, Zoltán WÉBER, Christian WEIDLE, Viktor WESZTERGOM, Gauthier WEYLAND, Štefan WIEMER, Felix WOLF, David WOLYNIEC, Thomas ZIEKE, Mladen ŽIVČIĆ.

5 Summary and Conclusions

The crustal structure and stress field in the wider Vienna Basin region are the focal points of this thesis. This thesis provides new insight into the geometry of the major geological crustal structures of the region, such as the Vienna Basin (and underlying rocks), and the Bohemian massif, as well as the orientation of the present-day stress field in the crust. Additionally, it gives insight into the geometry and mechanism of the recent Alland earthquake sequence, and the deeper crustal deformation of laterally extruded blocks.

Tomographic models of the region have been published by several authors before this thesis, but they show considerable disagreement on key aspects of the crustal structure in the wider Vienna basin region, e.g., the number, location, and extent of low-velocity anomalies (often associated with sedimentary basins). Studies on the orientation of the present-day stress-field are rare in this region, and they rely on pointwise measurements, such as borehole breakouts and focal mechanisms. Stress-field maps that are based on tectonic modelling show orientations of the stress-field that would render the observed seismic activity along the major fault systems in the region unlikely, if not impossible.

This thesis relies on a number of established seismological techniques and new data to shed light on the inconsistencies between previous studies of the region. The main approach is the utilization of the ambient seismic field to retrieve estimated Green's functions between station pairs without the need for earthquakes to generate seismic waves to illuminate the Earth. These inter-station Green's functions are used to compute an isotropic velocity model of the crust, as well as study the anisotropic structure in the region. In addition, classical techniques of earthquake seismology, namely aftershock relocation and moment tensor inversion, are applied to the Alland earthquake sequence.

The insights presented in this thesis are only possible thanks to the AlpArray project. The network of seismic stations, installed as part of this project, provides a dense coverage of continuous seismic records over several years, previously unavailable in the wider Vienna Basin region. In addition to these temporary broadband stations, this thesis relies on data of permanent broadband stations, provided by the national network operators of Austria, Czech Republic, Hungary, Slovakia, and Slovenia.

5.1 Crustal structure

The shear-velocity model presented in this thesis provides new and detailed insight into the crustal structure of the wider Vienna Basin region (Section 2). It is based on Rayleigh waves with periods

from 5s to 25s, retrieved from cross correlations of ambient noise across 67 broadband stations. These Rayleigh waves are used to constrain shear velocities in the top 30km across the region. At shallow depths (4km), the model reveals two separate major low-velocity anomalies in the center and Southeast of the study region, the Vienna Basin and Little Hungarian Plain. This observation is consistent with the model of Ren et al. (2013), but with greatly increased lateral resolution. Similarly, the Northwestern part of the study region shows consistently high velocities, representing the crystalline rocks of the Bohemian massif. Profile sections through the model reveal the crystalline basement of the Bohemian massif dipping towards Southeast, giving new constraints on the geometry of the European-Adriatic subduction interface. Underneath the Northeastern Vienna Basin, the model confirms a deep-seated low-velocity anomaly that appears to be a physical structure, not an artifact introduced during inversion. This feature has been previously observed in the model of Ren et al. (2013) and the previously unpublished seismic profile 7R by Dvorak et al. (1990). However, it remains unclear what this structure is. The model presented in this thesis further matches well with other observables, such as depths of the crystalline basement from boreholes and Bouguer gravity anomaly. The model constitutes the clearest image of the velocity structure of the crust in the wider Vienna Basin region yet.

The Alland earthquake sequence of 2016-2017 occurred in this region. In Section 3, the sequence is studied in terms of rupture geometry and mechanism. To estimate the geometry of the ruptured fault, the earthquakes are first relocated using NonLinLoc (Lomax et al., 2000) to retrieve improved absolute locations, which are then used as input to relocate all events relative to each other, using a double-difference approach (Waldhauser & Ellsworth, 2000). The sequence ruptured a Northeast-dipping fault in the crystalline basement in \sim 6.5km depth. It is located near the Eastern edge of the Bohemian Spur (Wessely, 2006), likely located in the crystalline basement of the Bohemian massif. The shear-velocity model in Section 2 confirms this assessment, as velocity profiles inside and outside the Bohemian Spur are distinct from each other. The velocity-model in Section 2 therefore also gives insight into the shape of the Bohemian Spur. Additionally, there is evidence for major NE-dipping reflectors in the Bohemian Spur from a local seismic reflection profile, consistent with the rupture geometry of the Alland sequence.

5.2 Stress field

The source mechanism of the Alland sequence (Section 3) provides insight not only into the geometry of the ruptured fault, but also the acting stress-field. Moment tensor inversion by matching synthetic with recorded waveforms shows that the main shock ruptured with a thrust-faulting mechanism striking NW/SE, consistent with the fault-plane orientation from aftershock relocation. The maximum horizontal compressive stress σ_H is therefore likely oriented NE-SW to facilitate this

sequence. This gives an important but pointwise proxy of the stress-field orientation.

To further substantiate the assessment that σ_H likely is oriented NE/SW in the region, the Rayleigh-wave group velocities that were used in Section 2 to retrieve an isotropic velocity model are studied carefully for azimuthal anisotropy in Section 4. The fast orientation of surface-wave propagation aligns with the orientation of σ_H in the shallow crust due to the formation of fluid-filled cracks along the stress field (Nur, 1971). The orientation of azimuthal anisotropy is therefore a proxy of the stress-field orientation. At the period that is most sensitive to shallow depths (5s), the stress-field shows a generally NNE/SSW-orientation, consistent with the Alland source mechanism. The distribution of regionalized fast orientations reveals a trend from West to East, with ~N/S-orientations of σ_H at the Western edge of the wider Vienna Basin region that rotate towards ~NE/SW-orientations in the East. These orientations are compatible with the seismic activity along the major fault systems in the wider Vienna Basin region, the sinistral strike-slip MML and Southern VBTFS, as well as the normal-faulting sides of the VBTFS. The results provide an independent estimate of the stress-field orientation and they are consistent with the smoothed map of stress-field orientations from pointwise measurements by Bada et al. (2007). The maps of Reinecker & Lenhardt (1999), Bada et al. (1998), and Gerner et al. (1999), however, show orientations normal to the Bohemian Spur, unsupported by the results of this thesis.

At greater depths, fast orientations of Rayleigh waves are no longer sensitive to fluid-filled cracks, as they are closed beyond ~3km depth. Instead they may represent the orientation of aligned crystals in the deeper crust due to continued deformation. At 20s (sensitive to mid-crustal depths), fast orientations rotate further towards ENE/WSW-orientations compared to the shallow crust, consistent with the direction of lateral extrusion of blocks from the Eastern Alps.

This thesis further demonstrates that measuring fast orientations of surface waves directly from group velocities and interpreting them in terms of anisotropic structure can heavily bias the results. The isotropic-anisotropic trade-off has to be considered carefully.

Appendices

A Appendix to Section 2

A.1 Determination of Pre-Processing Parameters

We tested the pre-processing of raw seismic records on a representative subset of the complete dataset to determine a processing-routine that enables reliable group-velocity dispersion measurements. We selected 5 temporary and 3 permanent stations, which represent a similar distribution in azimuth and inter-station distances compared to all available stations. For those station pairs, we used 110 simultaneously available days. We pre-processed the data from those stations with 384 parameter combinations to determine the optimal pre-processing scheme by tracking the development of signal-to-noise ratio (SNR) with number of stacked days (Figure A.1a).

We achieve 384 combinations by testing 4 different window lengths (Figure A.1a), 3 different clipping thresholds (Figure A.1b), 4 different energy-threshold levels (Figure A.1d), using spectral whitening or not (Figure A.1d), and 4 different thresholds for gap detection (not shown due to negligible influence on the SNR).

Stacking increases the SNR dramatically in the first \sim 10 days for all parameter sets. After this initial state, strong SNR differences appear between the 384 tested combinations. Generally, the SNR increases over time for all parameter sets, but some are more erratic than others. To look into this in more detail, we show the influence of each processing parameter in Figures A.1b) - e).

Figure A.1b illustrates that the window length has a strong effect on SNR. With shorter time windows, there is more data available to stack, which increases the SNR. There is a lower limit to the window lengths, which is dictated by the seismic waves travelling through the scattering medium from one station to the other. Therefore, we can not use indefinitely short time windows and settled on 30 minutes.

The influence of the clipping threshold is more complex to interpret (Figure A.1c). While the lowest SNR we find is achieved with the highest clipping threshold of 6 times the standard deviation, we also achieve very good SNR with the same clipping threshold. Similarly, the energy threshold (Figure A.1d), also displays a complex interplay with SNR. There seems to be a trade-off between clipping the data and energy-based removal of traces, because they have similar aims, i.e., removing unwanted signals from the continuous seismic records.

Finally, using no spectral whitening (Figure A.1e) results in the highest and lowest SNRs achieved, highly dependant on the other parameters. Importantly, while whitened examples have

a lower average SNR, the development of SNR with stacked days is much more stable. The whitening indeed aims to lessen the impact of remaining unwanted signals that pass the other thresholds. Therefore, we decided to use spectral whitening to reliably and stably increase SNR with increasing number of stacked days.

In Figure A.1f) and g) we show two examples of pre-processed, stacked cross-correlation functions for station pair A006A-A009A for the chosen parameter set (Figure A.1f) and the worst parameter set (Figure A.1g). We show the unfiltered stacked CCF and the filtered stacked CCF in the bandpass that we use in the study ($5\text{s} \leq T \leq 25\text{s}$). While the main arrival on the causal part is visible, although shaped slightly differently, in both examples the minor arrival on the acausal part remains only for the chosen parameter set (Figure A.1f).

A.2 Inter-station group velocities

The inter-station group velocities used to retrieve group velocity maps during the inversion scheme are shown in Figure A.2 for selected center periods. Over the entire period range, we see higher velocities in the West and lower velocities in the East of the study area. They range from 2.1km/s at $T = 5\text{s}$ to 3.3km/s at $T = 25\text{s}$. With increasing center period, the average group inter-station velocities increase from 2.7km/s at $T = 5\text{s}$ to 2.9km/s at $T = 25\text{s}$. Here, apparently no anomalous measurements remain thanks to the employed selection criteria and outlier removal. There is also no obvious velocity bias with distance or azimuth.

A.3 Regularization parameters λ and β

Here, we provide the 2D L-curve analysis for the regularization parameters controlling the norm of model λ , and β . In Figure A.3 we show the same visualizations as in Figure 5. The magnitude of variance reduction with varying λ and β is much less than for the other regularization parameters. Thus, we conclude that both of those parameters have only minimal impact on the inversion results. Still, we chose parameters near the maximum Gaussian curvature of the λ - β surface ($\lambda = 0.4$, $\beta = 5$), with negative values of curvature set to 0. Here, the Gaussian curvature analysis is less stable due to the maximum curvature occurring near the edge of the parameter space.

A.4 Group-velocity misfit

We present the Rayleigh group-velocity misfit distribution between the measured 1D group-velocity dispersion curves and the synthetic dispersion curves, calculated from the final shear-velocity

model. We extract and invert 1D dispersion curves for all cells that have an average of 3 paths crossing in the period range of 5 - 25s. We define misfit as the difference between observed and synthetic group velocities $m = v_{obs} - v_{syn}$. Therefore, positive misfits imply underestimated velocities in our final shear-velocity model, while negative misfits suggest overestimated velocities.

In Figure A.4a, we show the misfit distribution as boxplots for all center periods used in this study. For center periods $5 \leq T \leq 21$ s, the median misfit is close to 0km/s (± 0.01 km/s), suggesting that our final shear velocity model can explain the measured group velocity dispersion curves well in this period range. Towards higher periods ($T > 21$ s), the median deviates more strongly from 0km/s, with the largest deviation at $T = 25$ s with $m \sim 0.05$ km/s. This suggests that the group velocities at those higher periods are less well-represented by our final shear velocity model and the model likely underestimates velocities in the depth range, for which Rayleigh groups around $T = 25$ s are sensitive (see figure 9d in the main article).

In Figure A.4b, we show the stacked misfit-distribution over the whole period range. This distribution has a mean of 0.0005km/s, with a standard deviation of 0.37km/s. Overall, our model represents the measured dispersion curves well.

A.5 Figures

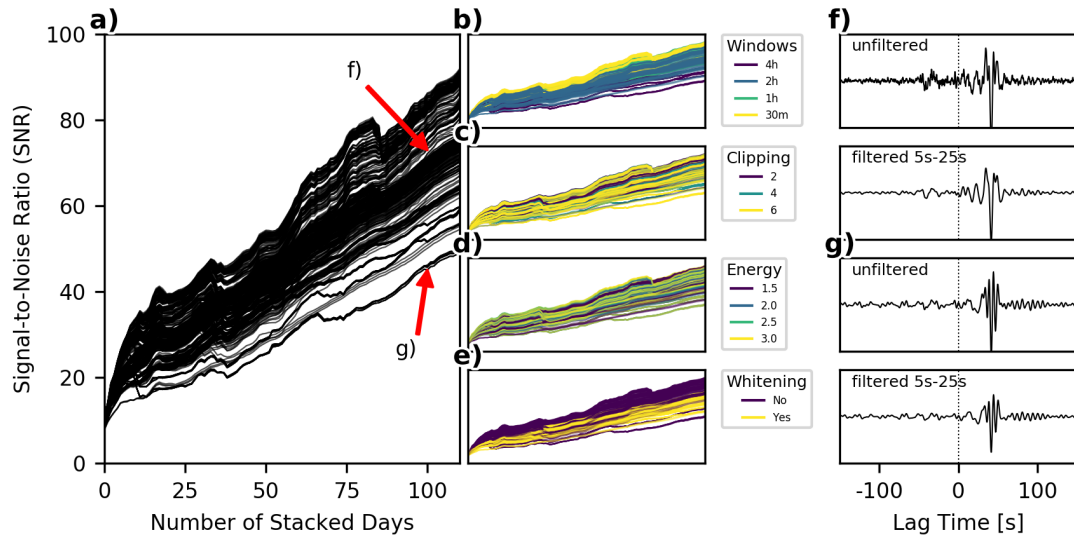


Figure A.1: Determination of pre-processing parameters using a representative subset of all data.
a) Evolution of Signal-to-Noise Ratio (SNR) with number of stacked days for 384 parameter sets.
b) Same as (a), colored by window length. **c)** Same as (a), colored by clipping threshold. **d)** Same as (a), colored by energy threshold. **e)** Same as (a), colored by the use of whitening. **f)** Unfiltered and filtered example stacked cross-correlation function of station pair A006A-A009A for the chosen parameter set. **g)** Same as (f) for the worst parameter set.

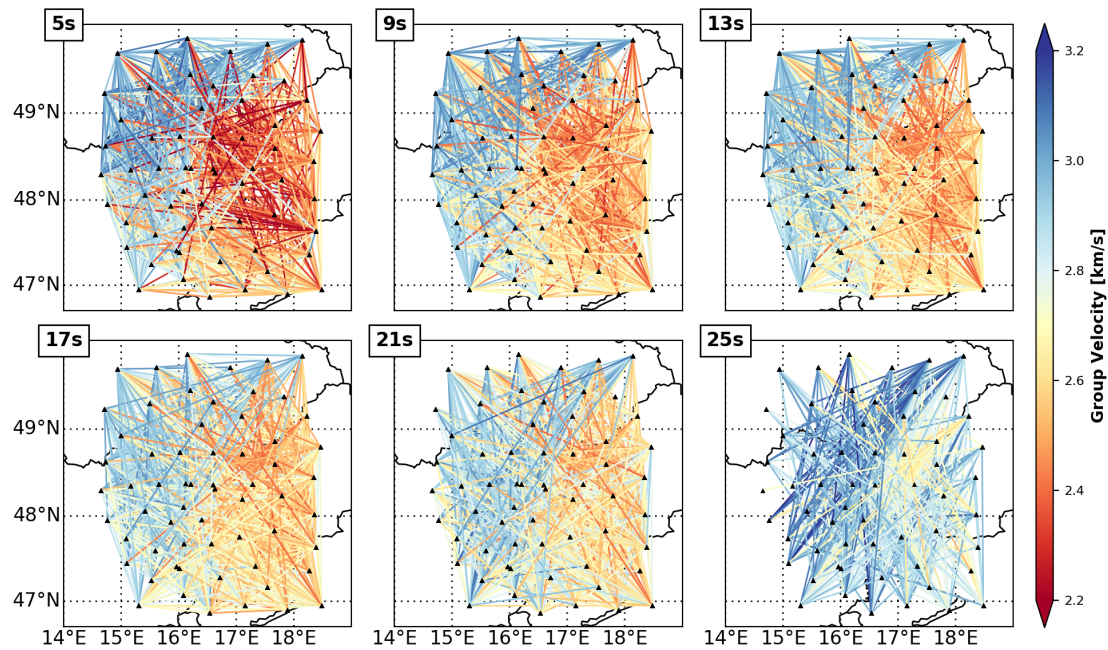


Figure A.2: Inter-station group velocities for selected center periods: 5s, 9s, 13s, 17s, 21s, and 25s. For all periods, we see higher velocities in the West and lower velocities in the East of the study area. With increasing period, velocities generally get faster.

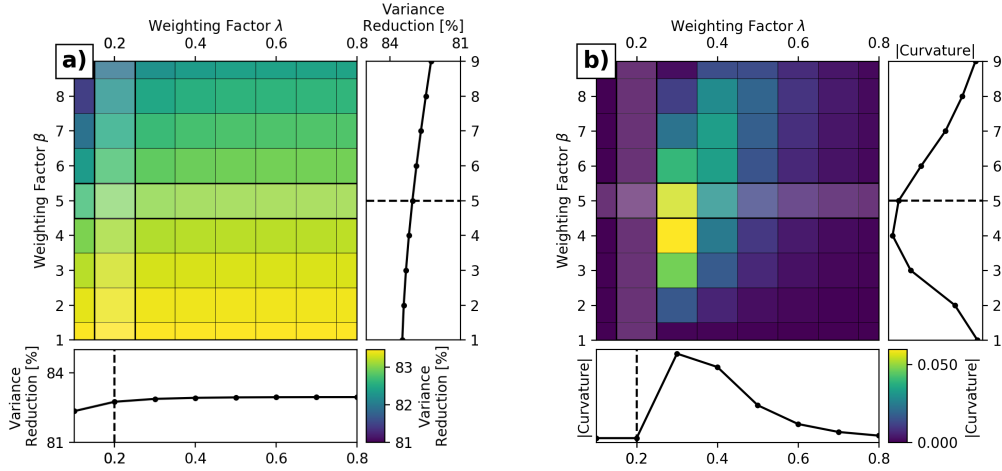


Figure A.3: 2D L-curve analysis for the regularization parameters λ and β . **a)** The main view shows the 2D surface of variance reduction in parameter space. The right view represents the slice through that surface at $\lambda = 0.4$. The bottom view represents the slice through the surface at $\beta = 5$. **b)** The main view shows the Gaussian curvature of the 2D surface in a). The other views are slices through the curvature. The values for the regularization parameters are picked near the maximum curvature ($\lambda = 0.4$, $\beta = 5$).

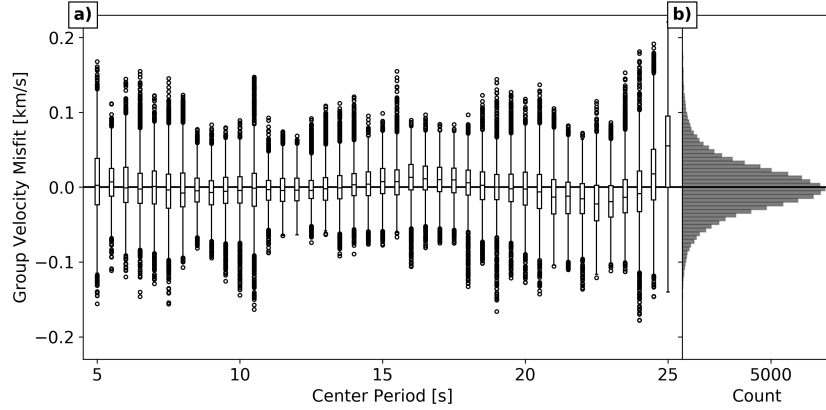


Figure A.4: Group velocity misfit distribution. **a)** Group velocity misfit boxplots for each center period, comparing measured velocities with synthetic group velocities, computed using our final shear velocity model. **b)** Stacked misfits over the entire period range $5s \leq T \leq 25s$.

B Appendix to Section 3

B.1 Estimation of Waveform Misfit

To evaluate the waveform fit, we follow the approach presented in Zhu & Helmberger (1996), which builds upon Zhao & Helmberger (1994) by fully utilizing amplitude information. The objective function is a combination of L1- and L2-norms of the waveform misfit, which are estimated by

$$e_{ijk} = d_k * ||f_k(t) - M_{0i}g_k(t)||,$$

with type of moment estimation i , the type of norm j (L1: $j = 1$, L2: $j = 2$), the channel k , the distance scaling factor d_k , the seismogram $f_k(t)$, the waveform predictions $g_k(t)$ computed for a scalar moment of 1Nm, and the seismic moment M_{0i} . $||x||$ represents the norm. The seismic moment M_{0i} is estimated as the ratio of the peak amplitudes of the seismograms and waveform predictions, for either only the current channel ($i = 1$) or averaged over all available channels of the current station ($i = 2$). Two norms are utilized, because the L1-norm emphasizes higher frequencies, whereas the L2-norm is more sensitive to lower frequencies Zhao & Helmberger (1994). The distance scaling factor $d_k = \frac{r_k}{r_0}^p$ with the epicentral distance r_k , a reference distance r_0 , and the scaling factor p aims to compensate amplitude decay due to geometrical spreading and attenuation Zhu & Helmberger (1996). Following Zhu & Helmberger (1996), we chose $r_0 = 100\text{km}$, $p = 0.55$ for Love waves, and $p = 0.75$ for Rayleigh waves. For every channel we estimate four waveform misfits: two types of norm ($j = 1, j = 2$) and the two types of moment estimation ($i = 1, i = 2$). For this error estimation, the waveforms are allowed to be shifted in time towards the best fit to account for regional geological deviations from the 1D model.

The objective functions computed for the two types of norm j are combined to

$$\hat{e}_{ik} = (e_{i,j=1,k} + e_{i,j=2,k} + (2e_{i,j=1,k}^2 + 2e_{i,j=2,k}^2)^{\frac{1}{2}})/4$$

and ultimately the final error \bar{e} over all investigated channels n is computed as

$$\bar{e} = \frac{1}{n} \sum_{k=1}^{k=n} (\hat{e}_{i=1,k} + \hat{e}_{i=2,k}).$$

Note that our use of indices deviates from Zhao & Helmberger (1994) and Zhu & Helmberger (1996) to more explicitly illustrate how the different errors are combined.

B.2 Moment Tensor Inversion Iterations

For the iterations after the first run, we determine the relative RMS misfit $\rho_k = \frac{(f(t)_k - g(t)_k)^2}{g(t)_k^2}$ for the seismogram $f_k(t)$ and synthetic waveform $g_k(t)$ of the channel k , and remove channels with an increasingly strict threshold over the following four iterations ($\rho_k > 10, \rho_k > 3, \rho_k > 2, \text{ and } \rho_k > 1$). The lenient threshold in the first iteration ($\rho_k > 10$) removes faulty or noise-dominated channels that do not fit the data at all and were not caught during the initial selection. The stricter thresholds used for the following three iterations ($\rho_k > 3, \rho_k > 2$, and $\rho_k > 1$) help converge to a stable solution that is preferred by the majority of available channels and is refined using only the best-fitting channels.

B.3 Figures

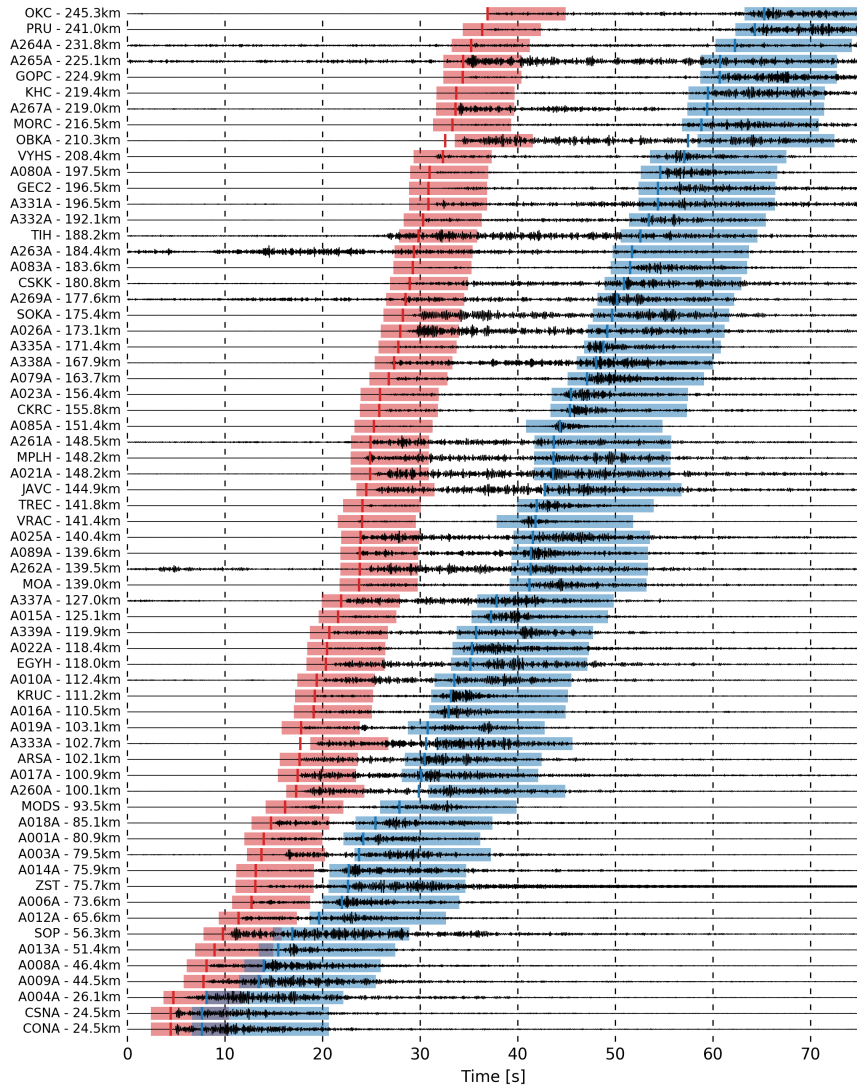


Figure B.1: Waveforms of the 25.04.2016 Alland mainshock on all seismological stations available on ORFEUS within 250km. Colored vertical lines indicate the theoretical first arrivals of P (red) and S (blue). The shaded areas indicate the P- (red) and S-time windows (blue) for each station used for cross-correlation.

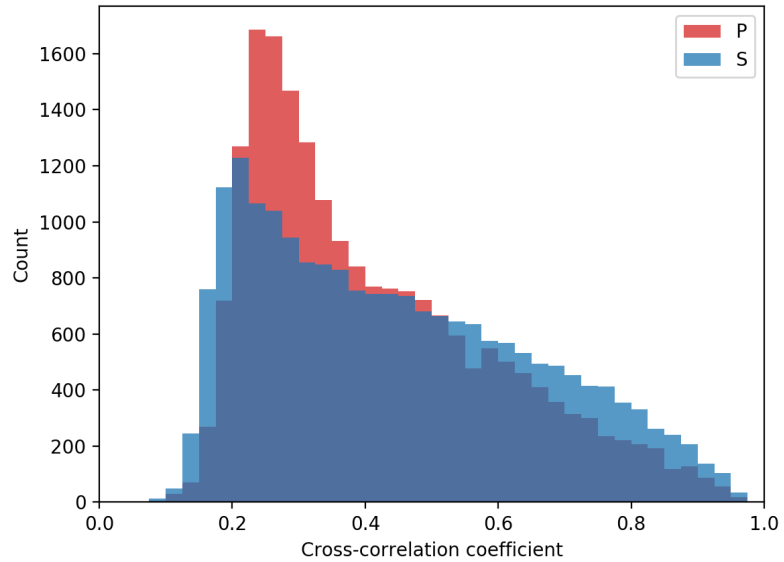


Figure B.2: Histogram of cross-correlation coefficients for P- (red) and S-phases (blue) used as weights for relocation, estimated on waveforms that were bandpass-filtered 5Hz - 15Hz. S-phases are better correlated (mean=0.44, median=0.41) than P-phases (mean=0.41, median=0.36). Generally high correlation coefficients suggest similar source mechanisms in nearby locations (see also Fig. 3.8).

Table B.1: Location of the Alland earthquake series from NonLinLoc (subscript **N**) and HypoDD (subscript **H**). The units are: Time in UTC, Magnitude (**MAG**) in local magnitude, Depths (**DEP**) in kilometers, NonLinLoc errors (**EX_N**, **EY_N**, **EZ_N**) in kilometers, HypoDD errors (**EX_H**, **EY_H**, **EZ_H**) in meters.

EVID	TIME	MAG	LAT _N	LONG _N	DEPN	EX _N	EY _N	EZ _N	LAT _H	LONG _H	DEPH	EX _H	EY _H	EZ _H
52699566	2016-04-24 00:17:42.74	1.7	48.0914	16.1059	9.2	1.67	1.67	3.26	48.087223	16.101303	6.654	3.1	2.6	3.6
52699568	2016-04-24 00:21:38.27	0.8	48.0772	16.1023	5.4	4.31	4.31	4.75	48.087321	16.100964	6.632	3.6	3.1	4.1
52699597	2016-04-25 10:28:22.84	4.2	48.0805	16.099	8.9	1.13	1.13	1.98	48.088265	16.10195	6.664	4.6	3.8	4.6
52699607	2016-04-25 10:49:36.70	2.5	48.0858	16.1157	8.4	2.07	2.07	3.52	48.086987	16.102815	6.687	3	2.3	3.3
52699623	2016-04-25 10:34:33.72	1.1	48.0903	16.1026	5.6	3.31	3.31	5.69	48.08871	16.104419	6.735	3.8	3.3	3.8
52699624	2016-04-25 10:36:06.63	1.1	48.0948	16.0982	5.6	4.11	4.11	5.76	48.088902	16.100909	6.706	3.1	3	4.3
52699633	2016-04-25 04:54:04.45	1.2	48.0882	16.1047	5.2	3.5	3.5	5.4	48.087476	16.101712	6.648	3.2	2.7	3.9
52699634	2016-04-25 05:40:45.05	1.8	48.0936	16.1103	8.4	1.66	1.66	3.29	48.087508	16.101358	6.643	2.9	2.3	3.5
52699639	2016-04-25 10:26:16.87	1.3	48.0903	16.1114	6.4	3.25	3.25	4.49	48.087675	16.101606	6.667	3.4	2.9	3.9
52699642	2016-04-25 10:36:48.90	0.9	48.086	16.0981	4.1	4.42	4.42	5.74	48.088013	16.104405	6.754	3.3	3.9	5.5
52699645	2016-04-25 10:58:32.71	1	48.0905	16.0893	8.1	5.37	5.37	8.11	48.088196	16.100516	6.67	3.8	4.4	5
52699646	2016-04-25 11:58:36.46	0.6	48.0706	16.1043	3.8	28.21	28.21	11.39	48.086857	16.103004	6.671	2.8	2.3	3.4
52699647	2016-04-25 12:05:52.05	1.1	48.0883	16.0959	3.2	4.24	4.24	5.85	48.087878	16.104189	6.71	3.3	3.2	4
52699648	2016-04-25 12:18:52.52	1.6	48.0859	16.1069	7.9	2.26	2.26	4.52	48.086365	16.09878	6.553	4	3.9	4.3
52699650	2016-04-25 12:33:17.82	1.7	48.0948	16.1027	8.1	2.04	2.04	3.45	48.086194	16.098584	6.552	4.7	4.1	4.6
52699651	2016-04-25 13:17:52.68	1.6	48.0946	16.1203	9.9	2.34	2.34	3.62	48.090214	16.101194	6.789	3.9	3.8	5.1
52699652	2016-04-25 13:28:25.52	1.8	48.1001	16.1127	9.8	1.92	1.92	3.32	48.089954	16.099408	6.731	3.5	3	3.5
52699653	2016-04-25 13:38:51.41	1	48.0792	16.1221	10.8	7.42	7.42	7.15	48.086556	16.102427	6.632	3	3.2	4.6
52699654	2016-04-25 14:57:43.35	1	48.0859	16.1113	10.1	3.53	3.53	5.74	48.085649	16.099072	6.544	3.9	4.5	5.6
52699659	2016-04-26 03:40:51.12	2.2	48.0815	16.1112	8.9	2.25	2.25	3.79	48.086934	16.103169	6.685	2.8	2.3	3.3
52699669	2016-04-25 18:35:51.53	0.7	48.086	16.0981	7.4	5.88	5.88	7.8	48.087516	16.102763	6.696	3	2.8	3.7
52699670	2016-04-25 17:18:40.19	0.1	48.0883	16.0959	4.8	8.51	8.51	8.6	48.089083	16.102077	6.503	7.4	8.1	10.4
52699672	2016-04-25 18:37:50.04	0.1	48.0794	16.0957	4.8	24.75	24.75	9.1	48.089237	16.100403	6.352	10.7	11.6	13.9
52699674	2016-04-25 20:23:21.43	1.3	48.0913	16.1125	8.6	1.76	1.76	3.37	48.086698	16.102952	6.657	2.9	2.3	3.4
52699676	2016-04-25 22:39:44.26	1.3	48.0859	16.1113	8.4	1.88	1.88	3.47	48.086719	16.102367	6.645	3	2.5	3.4
52699823	2016-04-26 23:04:40.67	0.6	48.0883	16.0871	3.8	8.16	8.16	6.93	48.089095	16.098269	6.527	4.7	6.3	7.4
52699844	2016-04-25 15:38:51.18	0.1	48.0794	16.0957	4.8	31.15	31.15	9.23	48.087622	16.102099	6.449	4.4	5.6	7.6
52699861	2016-04-27 07:48:52.54	2	48.0903	16.1114	9.1	2.92	2.92	3.79	48.087431	16.099594	6.627	3.4	2.8	3.8
52700013	2016-04-28 19:17:45.99	1.4	48.0947	16.1071	7.9	2.58	2.58	3.66	48.09069	16.102129	6.85	4	3.3	3.8

EVID	TIME	MAG	LAT _N	LONG _N	DEPN	EX _N	EY _N	EZ _N	LAT _H	LONG _H	DEPTH	EX _H	EY _H	EZ _H
52700068	2016-04-26 04:48:32.97	0.5	48.0794	16.0957	2.2	27.34	27.34	11.49	48.089022	16.102225	6.667	7.3	7.9	10.7
5270146	2016-04-29 13:52:39.60	0.5	48.0905	16.0893	5.9	4.53	6.22	48.086369	16.100456	6.647	5.7	4.9	5.4	
5270174	2016-04-30 14:47:39.08	1.1	48.0992	16.0983	7.9	2.4	3.73	48.090735	16.102244	6.883	4.7	3.5	4.1	
5270192	2016-05-01 05:19:41.46	0.7	48.0903	16.107	9.1	3.14	4.63	48.090759	16.102411	6.863	3.9	3.5	4.5	
52700966	2016-05-07 21:14:36.05	1	48.0882	16.1047	8.2	2.19	3.42	48.090881	16.101374	6.869	3.6	3.4	4.6	
52700967	2016-05-07 21:23:44.10	1.2	48.0903	16.1114	8.4	2.05	2.05	3.33	48.090889	16.101828	6.868	3.6	3.3	3.8
52700982	2016-05-10 05:52:00.84	2.6	48.0827	16.1057	9.6	1.4	2.84	48.086483	16.105586	6.681	3.1	2.4	3.3	
52700988	2016-05-10 05:41:41.74	2.2	48.0827	16.1035	8.1	1.69	3.28	48.086637	16.104519	6.704	2.8	2.1	3.3	
52700996	2016-05-10 05:44:44.98	1.6	48.0881	16.1135	7.2	2.36	3.8	48.087048	16.104962	6.707	2.8	2.3	3.5	
52700998	2016-05-10 06:04:34.96	1.6	48.0859	16.1069	7.9	2.25	2.25	4.12	48.086723	16.105735	6.698	2.8	2.1	3.4
52701000	2016-05-10 02:01:57.42	0.6	48.0859	16.1025	9.1	3.56	5.63	48.08783	16.099841	6.611	7.6	6	9.1	
52701004	2016-05-10 05:43:22.12	0.4	48.0882	16.1047	6.8	8.11	9.09	48.086922	16.104211	6.678	7.4	6.7	7	
52701008	2016-05-10 05:58:02.19	0.6	48.0706	16.1043	3.8	6.41	6.41	7.24	48.086523	16.10552	6.761	3.8	5.7	7.7
52701012	2016-05-10 07:17:16.89	1.1	48.0903	16.1026	5.6	3.18	3.18	5.27	48.086554	16.106365	6.712	2.9	2.3	3.5
52701013	2016-05-10 08:15:59.86	0.7	48.0883	16.0871	2.2	9.6	9.6	7.55	48.089657	16.114374	6.947	10.2	8.8	19.2
52701118	2016-05-10 15:49:12.24	1.2	48.0948	16.0938	4.4	2.96	4.1	48.086941	16.103963	6.696	3.4	2.9	3.7	
52701120	2016-05-10 17:49:54.76	0.9	48.099	16.116	8.1	3.35	3.35	5.28	48.084668	16.101403	6.579	3.7	3.9	5.2
52701179	2016-05-11 22:07:11.25	0.9	48.0859	16.1025	5.4	2.59	4.06	48.086121	16.106167	6.668	2.8	2.5	3.9	
52701299	2016-05-13 11:57:23.32	1.6	48.0817	16.098	2.9	2.39	3.52	48.086096	16.105743	6.673	2.8	2.2	3.6	
52701493	2016-05-16 11:50:23.27	1.1	48.086	16.0981	6.1	2.33	2.33	3.63	48.090828	16.101028	6.864	3.6	3.1	4.4
52701564	2016-05-13 12:21:07.18	0.8	48.0793	16.1133	1.2	6.67	6.67	6.08	48.085974	16.105634	6.642	3.2	2.7	3.7
52701632	2016-05-13 22:16:52.04	1.2	48.0902	16.1202	7.4	2.23	2.23	3.99	48.086247	16.106306	6.68	3	2.3	3.9
52701749	2016-05-18 20:55:26.99	1	48.0948	16.0938	6.1	6.14	6.14	6.63	48.090564	16.102043	6.817	3.5	2.8	3.9
52702011	2016-05-20 22:00:17.72	1.8	48.0902	16.1158	8.9	1.74	1.74	3.01	48.086991	16.106469	6.709	3	2.4	3.4
52702111	2016-05-20 19:07:56.52	0.2	48.0706	16.1043	1.8	32.91	32.91	7.95	48.085311	16.102522	5.409	7.7	8.1	7
52702674	2016-05-29 21:19:15.35	1	48.0904	16.0981	6.4	3.33	3.33	5.54	48.08658	16.106608	6.699	3.3	2.8	3.6
52703238	2016-06-05 19:56:41.68	0.7	48.0904	16.0937	4.1	4.05	4.05	5.61	48.088082	16.104974	6.763	5.6	5.2	5.7
52703803	2016-06-11 23:26:41.84	0.3	48.0817	16.098	5.9	6.06	6.06	6.62	48.086569	16.098846	6.568	4.6	4.3	5.1
52705998	2016-07-08 01:04:14.59	0.7	48.0859	16.1113	8.1	2.37	2.37	3.83	48.085722	16.099022	6.549	4.3	4.2	5.1
52708045	2016-07-31 07:13:25.80	1.7	48.0946	16.1203	10.4	1.74	1.74	3.12	48.086975	16.105802	6.705	2.9	2.2	3.4
52737523	2017-11-08 18:36:27.04	3.1	48.0805	16.099	8.2	1.43	1.43	3.04	48.087093	16.104749	6.723	3.6	3.1	3.6
52737570	2017-11-08 18:54:19.83	1.3	48.095	16.0762	5.6	3.58	3.58	4.59	48.086454	16.103415	6.664	2.8	2	3.4
52787571	2017-11-08 18:53:12.94	0.9	48.0816	16.1068	4.9	6.91	6.91	6.32						
52787572	2017-11-08 18:53:04.87	0.8	48.0794	16.1045	4.8	8.79	8.79	6.67						

EVID	TIME	MAG	LAT _N	LONG _N	DEP _N	EX _N	EY _N	EZ _N	LAT _H	LONG _H	DEP _H	EX _H	EY _H	EZ _H
52787575	2017-11-08 19:37:59.03	1	48.0816	16.1024	4.1	4.88	4.88	5.81	48.087085	16.105894	6.719	3.6	2.8	3.7
52787579	2017-11-08 21:10:36.65	0.7	48.0772	16.1023	5.1	6.35	6.35	5.79	48.086422	16.103787	6.664	3.5	2.8	3.7
52787581	2017-11-08 23:03:27.59	1.1	48.0904	16.0937	5.9	4.44	4.44	5.45	48.088171	16.103512	6.711	2.8	2.1	3.3
52787641	2017-11-08 18:53:20.24	0.9	48.0927	16.0916	2.5	119.13	119.13	19.14						
52787653	2017-11-09 02:33:35.72	0.3	48.0971	16.0873	2.2	34.74	34.74	11.87	48.087683	16.104002	6.711	3.3	3.3	4.2
52788021	2017-11-10 11:13:34.44	1.1	48.0794	16.0957	2.8	5.83	5.83	6.01	48.086186	16.103834	6.644	3	2.2	3.3
52788567	2017-11-12 04:34:00.92	1.2	48.0859	16.1069	10.6	2.64	2.64	5.23	48.087972	16.104466	6.729	3.1	2.9	4.3
52788879	2017-11-14 14:32:46.88	1.6	48.0903	16.107	6.6	1.99	1.99	3.74	48.086479	16.103621	6.663	3.1	2.5	3.4

C Appendix to Section 4

C.1 Figures

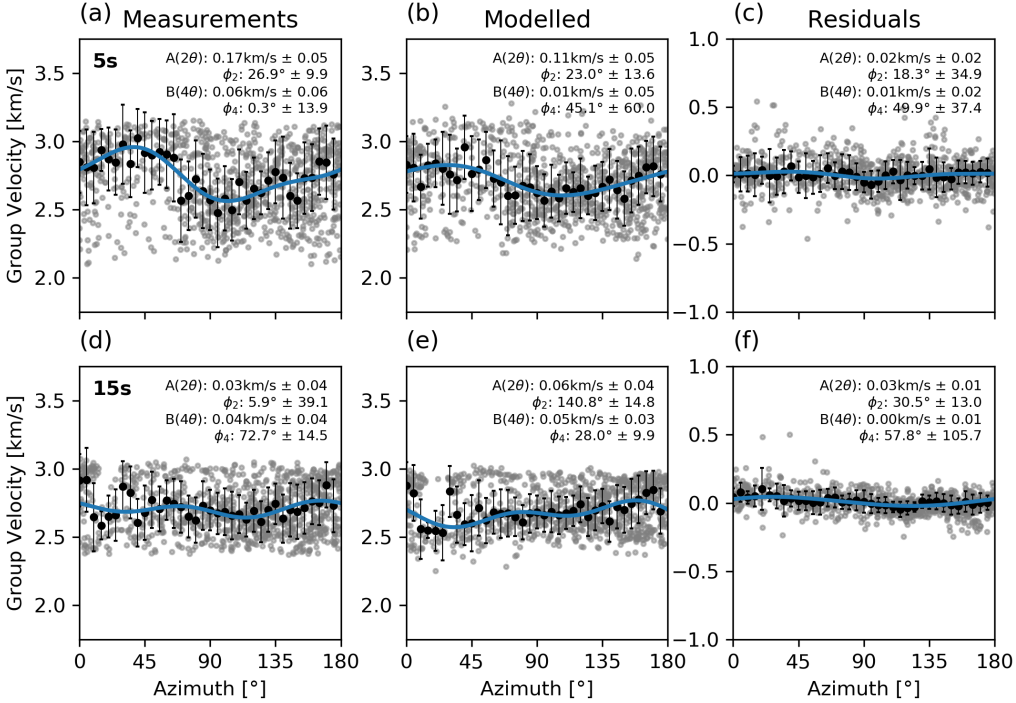


Figure C.1: Measurement of the 2θ - and 4θ -anisotropy terms on all available group velocities for 5s (a - c) and 15s (d - f) on measured group velocities (a, d), modelled group velocities (b, e), and group velocity residuals (c, f). Group velocities are binned in 5° azimuth bins and the medians in each bin (black dots) are weighted by standard deviation (error bars). The blue line is the best fitting curve, using the parametrization described in the main text. Strong directional dependence on measured group velocities (left column) is fairly well-explained by modelled group velocities (center column) from the isotropic velocity model of (Schippkus et al., 2018). Residuals show weaker anisotropy on the order of 1%.

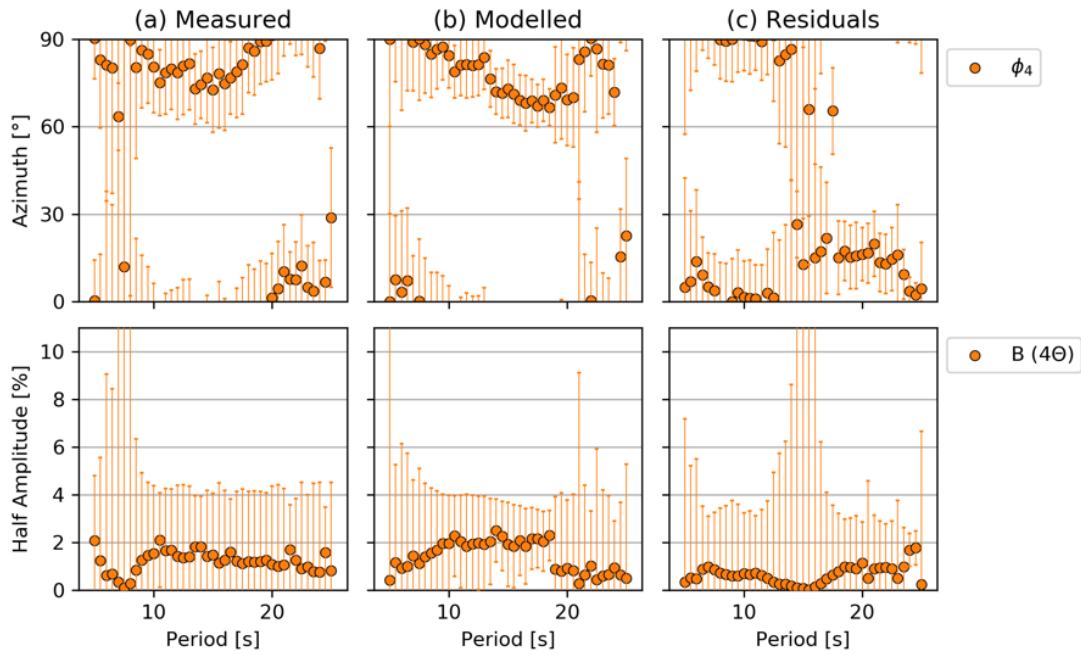


Figure C.2: Directional dependence (4Θ -terms) of group velocities, similar to Figure 4.3. Azimuth limited to $0 - 90^\circ$, because of $\pi/2$ -symmetry of the 4Θ -term. Low amplitudes ($B \leq 2\%$) for all periods on measured (a), modelled (b), and residual group velocities (c). Fast directions for measured and modelled group velocities match fairly well. Fast directions measured on residual group velocities show very low amplitudes with high errors, suggesting that there is no significant contribution of the 4Θ -terms.

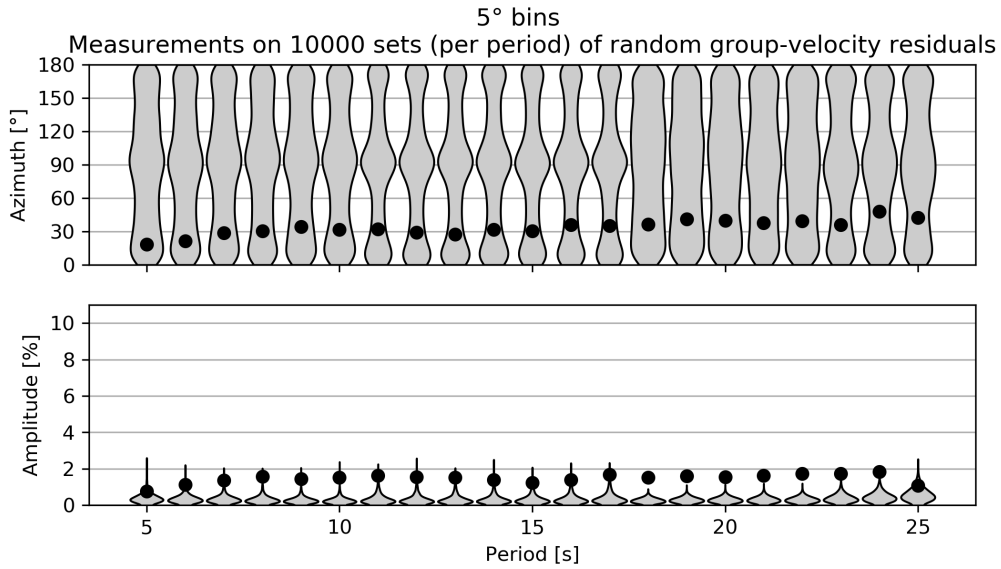


Figure C.3: Numerical simulations of 2Θ -parameter-retrieval for 10,000 random sets of inter-station group-velocity residuals per period (grey violin plots) and how they compare to the measured parameters (black dots). Each violin plot represents the normalized distribution of the results for all sets for a given period. Available inter-station azimuths for each period after applying quality criteria (see Fig. C.1) were used for the simulations. On random data, our procedure introduces a slight bias in the retrieved fast directions for some periods around 0° and 90° (top) due to available inter-station paths (see Fig. 4.2), the azimuth-binning, and very low amplitudes. The consistent fast directions with period we observe and their significantly higher amplitudes than random group-velocity residuals would yield, however, confirm that the group-velocity residuals do still contain information about the structure of the Earth. While the measured azimuthal anisotropy is weak ($A < 2\%$), the measurements are exceedingly unlikely to be explained by chance, especially considering the consistency of fast directions and amplitudes over the available period range.

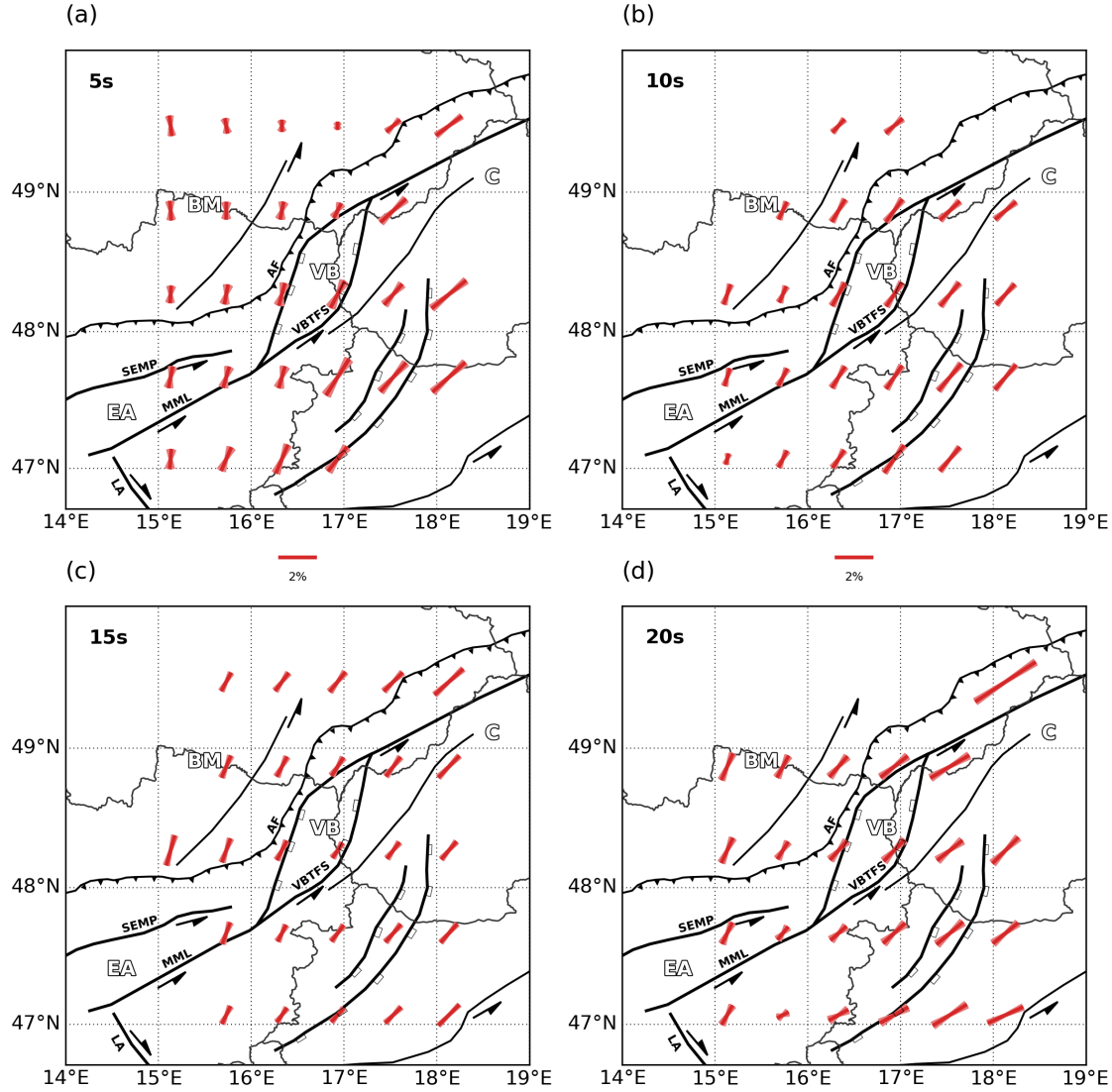


Figure C.4: Regionalized azimuthal anisotropy of Rayleigh waves for the available period range (5s - 20s). The shown periods have their maximum sensitivity to shear-velocity at depths of $\sim 2\text{km}$ (5s, a), $\sim 7\text{km}$ (10s, b), $\sim 11\text{km}$ (15s, c), $\sim 15\text{km}$ (20s, d), and are sensitive to a broad range of depths (see Fig. 4.7, main text). Rotation of fast directions towards East with increasing period. This represents a gradual shift from sensitivity to the shallow stress field at shorter periods (5s) to sensitivity to mid-crustal deformation at longer periods (20s), which results in different fast orientations.

References

- Abercrombie, R. E., 1996. The magnitude-frequency distribution of earthquakes recorded with deep seismometers at Cajon Pass, southern California, *Tectonophysics*, **261**, 1–7.
- Abercrombie, R. E., Bannister, S., Pancha, A., Webb, T. H., & Mori, J. J., 2001. Determination of fault planes in a complex aftershock sequence using two-dimensional slip inversion, *Geophysical Journal International*, **146**, 134–142.
- AEC, 2016. Austrian Earthquake Catalogue. ZAMG, Central Institute for Meteorology and Geodynamics.
- Aki, K., 1957. Space and time spectra of stationary stochastic waves, with special reference to microtremors, *Bulletin of the Earthquake Research Institute*, **35**, 415–457.
- Allmann, B. P. & Shearer, P. M., 2009. Global variations of stress drop for moderate to large earthquakes, *Journal of Geophysical Research: Solid Earth*, **114**(B1), 24,015–22.
- AlpArray Seismic Network, 2015. Temporary component, AlpArray Working Group, Other/Seismic Network. Datacite Link: http://data.datacite.org/10.12686/alparray/z3_2015. doi:10.12686/alparray/z3_2015.
- An, M., 2012. A simple method for determining the spatial resolution of a general inverse problem, *Geophysical Journal International*, **191**(2), 849–864.
- Angelier, J., 2002. Inversion of earthquake focal mechanisms to obtain the seismotectonic stress IV-a new method free of choice among nodal planes, *Geophysical Journal International*, **150**(3), 588–609.
- Apoloner, M.-T., Tary, J.-B., & Bokelmann, G., 2015. Ebreichsdorf 2013 earthquake series: Relative location, *Austrian Journal of Earth Sciences*, **108**(2), 1–10.
- April 2019 ZAMG Seismicity Report, 2019. ZAMG, Central Institute for Meteorology and Geodynamics. <http://www.zamg.ac.at/geophysik/Reports/Monatsberichte/K19-04.pdf>.
- Aschk, K., 2005. IGME 5000: 1 : 5 Million International Geological Map of Europe and Adjacent Areas. BGR (Hannover).
- Austrian Seismic Network, 1987. ZAMG, Central Institute for Meteorology and Geodynamics.
- Bada, G., Cloetingh, S., Gerner, P., & Horváth, F., 1998. Sources of recent tectonic stress in the Pannonian region: inferences from finite element modelling, *Geophysical Journal International*, **134**(1), 87–101.
- Bada, G., Horváth, F., Dövényi, P., Szafián, P., Windhoffer, G., & Cloetingh, S., 2007. Present-day stress field and tectonic inversion in the Pannonian basin, *Global and Planetary Change*, **58**(1-4), 165–180.
- Barmin, M. P., Ritzwoller, M. H., & Levshin, a. L., 2001. A Fast and Reliable Method for Surface Wave Tomography , *Pure and Applied Geophysics*, **158**, 1351–1375.

- Barruol, G. & Kern, H., 1996. Seismic anisotropy and shear-wave splitting in lower-crustal and upper-mantle rocks from the Ivrea Zone - experimental and calculated data, pp. 175–194.
- Basili, R., Kastelic, V., Demircioğlu, M. B., García Moreno, D., Nemser, E. S., Petricca, P., Sboras, S. P., Besana-Ostman, G. M., Cabral, J., Camelbeeck, T., Caputo, R., Danciu, L., Domac, H., Fonseca, J., García-Mayordomo, J., Giardini, D., Glavatovic, B., Gulen, L., Ince, Y., Pavlides, S., Sesetyan, K., Tarabusi, G., Tiberti, M. M., Utkucu, M., Valensise, G., Vanneste, K., Vilanova, S., & Wössner, J., 2013. The European Database of Seismogenic Faults (EDSF) compiled in the framework of the Project SHARE.
- Behm, M., Brückl, E., Chwatal, W., & Thybo, H., 2007. Application of stacking and inversion techniques to three-dimensional wide-angle reflection and refraction seismic data of the Eastern Alps, *Geophysical Journal International*, **170**(1), 275–298.
- Behm, M., Nakata, N., & Bokelmann, G., 2016. Regional Ambient Noise Tomography in the Eastern Alps of Europe, *Pure and Applied Geophysics*, **173**(8), 2813–2840.
- Ben-Zion, Y., Vernon, F. L., Ozakin, Y., Zigone, D., Ross, Z. E., Meng, H., White, M., Reyes, J., Hollis, D., & Barklage, M., 2015. Basic data features and results from a spatially dense seismic array on the San Jacinto fault zone, *Geophysical Journal International*, **202**(1), 370–380.
- Bensen, G. D., Ritzwoller, M. H., Barmin, M. P., Levshin, a. L., Lin, F. C., Moschetti, M. P., Shapiro, N. M., & Yang, Y., 2007. Processing seismic ambient noise data to obtain reliable broad-band surface wave dispersion measurements, *Geophysical Journal International*, **169**(3), 1239–1260.
- Berka, R., 2015. Zur Geologie der großen Beckengebiete des Ostalpenraumes , in *Abhandlungen der geologischen Bundesanstalt, Band*, pp. 71–141, ed. Schubert, G.
- Beyreuther, M., Barsch, R., Krischer, L., Megies, T., Behr, Y., & Wassermann, J., 2010. Obspy: A python toolbox for seismology, *Seismological Research Letters*, **81**(3), 530.
- Bleibinhaus, F. & Brückl, E., 2006. Wide-angle observations of ALP 2002 shots on the TRANSALP profile: Linking the two DSS projects, *Tectonophysics*, **414**(1), 71–78.
- Boness, N. L. & Zoback, M. D., 2006. Mapping stress and structurally controlled crustal shear velocity anisotropy in California, *Geology*, **34**(10), 825–828.
- Bonvalot, S., Balmino, G., Briais, A., Kuhn, M., Peyrefitte, A., N., V., Biancale, R., Gabalda, G., Requin, F., & Sarraih, M., 2012. World Gravity Map. Commission for the Geological Map of the World. Eds. BGI-CGMW-CNES-IRD, Paris.
- Boué, P., Roux, P., Campillo, M., & Brand, X., 2014. Phase velocity tomography of surface waves using ambient noise cross-correlation and array processing, *Journal of Geophysical Research: Solid Earth*, **119**, 519–529.
- Brandmayr, M., Dallmeyer, R. D., Handler, R., & Wallbrecher, E., 1995. Conjugate shear zones in the Southern Bohemian Massif (Austria)" implications for Variscan and Alpine tectonothermal activity, *Tectonophysics*, **248**, 97–116.
- Brenguier, F., Campillo, M., Takeda, T., Aoki, Y., Shapiro, N. M., Briand, X., Emoto, K., & Miyake, H., 2014. Mapping pressurized volcanic fluids from induced crustal seismic velocity drops, *Science*, **345**(6192), 80–82.

- Brix, F. & Schultz, O., 1993. *Erdöl und Erdgas in Österreich*, Naturhistorisches Museum Wien and F. Berger, Horn, Wien.
- Brückl, E., Bodoky, T., Hegedüs, E., Hrbcová, P., Gosar, A., Grad, M., Guterch, A., Hajnal, Z., Keller, G. R., Špičák, A., Sumanovac, F., Thybo, H., & Weber, F., 2003. ALP 2002 Seismic Experiment, *Studia Geophysica et Geodaetica*, **47**(3), 671–679.
- Brückl, E., Behm, M., Decker, K., Grad, M., Guterch, A., Keller, G. R., & Thybo, H., 2010. Crustal structure and active tectonics in the Eastern Alps, *Tectonics*, **29**(2).
- Brückl, E., Mitterbauer, U., & Behm, M., 2011. Shape and origin of the East-Alpine slab constrained by the ALPASS teleseismic model, *Tectonophysics*, **510**(1-2), 195–206.
- Brückl, E., Weber, R., Apoloner, M.-T., Brückl, J., Loderer, W., Maras, J., Mertl, S., Moeller, G., Schurr, B., Weginger, S., & Umnig, E., 2014. ALPAACT - Seismological and Geodetic Monitoring of Alpine-PAnnonian Active Tectonics Final Report 2008 – 2013, Tech. rep.
- Brudy, M., Zoback, M. D., Fuchs, K., Rummel, F., & Baumgärtner, J., 1997. Estimation of the complete stress tensor to 8 km depth in the KTB scientific drill holes: Implications for crustal strength, *Journal of Geophysical Research: Solid Earth*, **102**(B8), 18453–18475.
- Bulut, F., Bohnhoff, M., Aktar, M., & Dresen, G., 2007. Characterization of aftershock-fault plane orientations of the 1999 Izmit (Turkey) earthquake using high-resolution aftershock locations, *Geophysical Research Letters*, **34**(20), 521–4.
- Caffagni, E., Eaton, D. W., Jones, J. P., & van der Baan, M., 2016. Detection and analysis of micro-seismic events using a Matched Filtering Algorithm (MFA), *Geophysical Journal International*, p. ggw168.
- Campillo, M. & Paul, A., 2003. Long-range correlations in the diffuse seismic coda., *Science*, **299**(5606), 547–549.
- Campillo, M. & Roux, P., 2015. Crust and Lithospheric Structure - Seismic Imaging and Monitoring with Ambient Noise Correlations, in *Treatise on Geophysics*, pp. 391–417, Elsevier, Oxford.
- Crotwell, H. P., Owens, T. J., & Ritsema, J., 1999. The TauPToolkit: Flexible Seismic Travel-time and Ray-path Utilities, *Seismological Research Letters*, **70**(2), 154–160.
- Cupillard, P., Stehly, L., & Romanowicz, B., 2011. The one-bit noise correlation: a theory based on the concepts of coherent and incoherent noise, *Geophysical Journal International*, **184**(3), 1397–1414.
- Czech Regional Seismic Network, 1973. Institute of Geophysics, Academy of Sciences of the Czech Republic, International Federation of Digital Seismograph Networks, doi:10.7914/SN/CZ.
- Dando, B. D. E., 2011. *Seismological structure of the Carpathian-Pannonian region of central Europe*, Ph.D. thesis, University of Leeds.
- Decker, K., PERESSON, H., & Hinsch, R., 2005. Active tectonics and Quaternary basin formation along the Vienna Basin Transform fault, *Quaternary Science Reviews*, **24**(3-4), 305–320.

- Decker, K., Gangl, G., & Kandler, M., 2006. The earthquake of Carnuntum in the fourth century a.d. – archaeological results, seismologic scenario and seismotectonic implications for the Vienna Basin fault, Austria, *Journal of Seismology*, **10**(4), 479–495.
- Diehl, T., Husen, S., Kissling, E., & Deichmann, N., 2009. High-resolution 3-D P-wave model of the Alpine crust, *Geophysical Journal International*, **179**(2), 1133–1147.
- Duputel, Z., Rivera, L., Kanamori, H., & Hayes, G., 2012. W phase source inversion for moderate to large earthquakes (1990–2010), *Geophysical Journal International*, **189**(2), 1125–1147.
- Dvorak, V., Dvorakova, L., Ibrmajer, I., Mayerova, M., Mitrenga, P., Naklaalova, Z., Novotny, M., Slavik, R., Tomek, Č., & Wohlgemuth, J., 1990. Vysledky hlubinného vyzkumu kry v Západních Karpatech a na JV svazích Českého masívu, *MS Geofyzika a.s.*.
- Dziewonski, A., Bloch, S., & Landisman, M., 1969. A Technique for the Analysis of Transient Seismic Signals, *Bulletin of the Seismological Society of America*, **59**, 427–444.
- Eshelby, J. D., 1957. The Determination of the Elastic Field of an Ellipsoidal Inclusion, and Related Problems, *Proceedings of the Royal Society A: Mathematical, Physical and Engineering Sciences*, **241**(1226), 376–396.
- Fojtíková, L., Vavryčuk, V., Cipciar, A., & Madarás, J., 2010. Focal mechanisms of micro-earthquakes in the Dobrá Voda seismoactive area in the Malé Karpaty Mts. (Little Carpathians), Slovakia, *Tectonophysics*, **492**(1-4), 213–229.
- Frank, C., Nagel, D., & Rabeder, G., 1997. Chronologie des österreichischen Plio-Pleistozäns, in *Pliozäne und pleistozäne Faunen Österreichs. Mitteilungen der Kommission für Quartärforschung der österreichischen Akademie der Wissenschaften*, vol. 10, eds Döppes, D. & Rabeder, G., Österr. Akad. Wiss., Wien.
- Froment, B., Campillo, M., Roux, P., Gouédard, P., Verdel, A., & Weaver, R. L., 2010. Estimation of the effect of nonisotropically distributed energy on the apparent arrival time in correlations, *GEOPHYSICS*, **75**(5), SA85–SA93.
- Fuchs, F., Kolínský, P., Gröschl, G., Apoloner, M. T., Qorbani, E., Schneider, F., & Bokelmann, G., 2015. Site selection for a countrywide temporary network in Austria: noise analysis and preliminary performance, *Advances in Geosciences*, **41**, 25–33.
- Fuchs, F., Lenhardt, W., Bokelmann, G., & the AlpArray Working Group, 2018. Seismic detection of rockslides at regional scale: examples from the Eastern Alps and feasibility of kurtosis-based event location, *Earth Surface Dynamics*, **6**(4), 955–970.
- Gephart, J. W. & Forsyth, D. W., 1984. An improved method for determining the regional stress tensor using earthquake focal mechanism data: Application to the San Fernando Earthquake Sequence, *Journal of Geophysical Research*, **89**(B11), 9305–9320.
- Gerner, P., Bada, G., Dövényi, P., Müller, B., Oncescu, M. C., Cloetingh, S., & Horváth, F., 1999. Recent tectonic stress and crustal deformation in and around the Pannonian Basin: data and models, *(156)*, 269–294.

- Godey, S., Bossu, R., Guibert, J., & Mazet-Roux, G., 2006. The Euro-Mediterranean Bulletin: A Comprehensive Seismological Bulletin at Regional Scale, *Seismological Research Letters*, **77**(4), 460–474.
- Gribovszki, K., Kovács, K., Mónus, P., Bokelmann, G., Konecny, P., Lednická, M., Moseley, G., Spötl, C., Edwards, R. L., Bednárik, M., Brimich, L., & Tóth, L., 2017. Estimating the upper limit of prehistoric peak ground acceleration using an in situ, intact and vulnerable stalagmite from Plavecká priepest cave (Detrekői-zsomboly), Little Carpathians, Slovakia—first results, *Journal of Seismology*, **21**(5), 1–20.
- Gutdeutsch, R. & Aric, K., 1988. Seismicity and neotectonics of the East Alpine-Carpathian and Pannonian Area, in *The Pannonian Basin: A Study in Basin Evolution/Book and Maps (Aapg Memoir)*, pp. 183–194, ed. Royden, L. H.
- Gutdeutsch, R., Hammerl, C., Mayer, I., & Vocelka, K., 1987. *Erdbeben als historisches Ereignis: Die Rekonstruktion des Bebens von 1590 in Niederösterreich*, images-na.ssl-images-amazon.com.
- Guterch, A., Grad, M., Keller, G. R., Posgay, K., Vozár, J., Špičák, A., Brückl, E., Hajnal, Z., Thybo, H., Selvi, O., & Team, C. E., 2003. CELEBRATION 2000 seismic experiment, *Studia Geophysica et Geodaetica*, **47**, 659–669.
- Hammerl, C., 2017. Historical earthquake research in Austria, *Geoscience Letters*, **4**(7), 1–13.
- Hammerl, C. & Lenhardt, W., 2013. Das Erdbeben von 1590 im Tullner Feld, in *Arbeitstagung der Geologischen Bundesanstalt*, pp. 93–100.
- Hanks, T. C. & Kanamori, H., 1979. A moment magnitude scale, *Journal of Geophysical Research*, **84**(B5), 2348–2350.
- Hansen, P. C. & O’Leary, D. P., 1993. The Use of the L-Curve in the Regularization of Discrete Ill-Posed Problems, *SIAM Journal on Scientific Computing*, **14**(6), 1487–1503.
- Harris, D. B., 2006. Subspace Detectors: Theory, Tech. rep.
- Hasselmann, K., 1963. A Statistical Analysis of the Generation of Microseisms, *Reviews of Geophysics*, **1**(2), 177–210.
- Heidbach, O., Custodio, S., Kingdon, A., Mariucci, M. T., Montone, P., Müller, B., Pierdominici, S., Rajabi, M., Reinecker, J., Reiter, K., Tingay, M., Williams, J., & Ziegler, M., 2016. Stress Map of the Mediterranean and Central Europe 2016, GFZ Data Service.
- Heidbach, O., Rajabi, M., Cui, X., Fuchs, K., Müller, B., Reinecker, J., Reiter, K., Tingay, M., Wenzel, F., Xie, F., Ziegler, M. O., Zoback, M.-L., & Zoback, M., 2018. The World Stress Map database release 2016: Crustal stress pattern across scales, *Tectonophysics*, **744**, 484–498.
- Herrmann, R. B., 2013. Computer Programs in Seismology: An Evolving Tool for Instruction and Research, *Seismological Research Letters*, **84**(6), 1081–1088.

- Hetényi, G., Molinari, I., Clinton, J., Bokelmann, G., Bondár, I., Crawford, W. C., Dessa, J.-X., Doubre, C., Friederich, W., Fuchs, F., Giardini, D., Grácer, Z., Handy, M. R., Herak, M., Jia, Y., Kissling, E., Kopp, H., Korn, M., Margheriti, L., Meier, T., Mucciarelli, M., Paul, A., Pesaresi, D., Piromallo, C., Plenefisch, T., Plomerová, J., Ritter, J., Rümpker, G., Šipka, V., Spallarossa, D., Thomas, C., Tilman, F., Wassermann, J., Weber, M., Wéber, Z., Wesztergom, V., Živčić, M., Abreu, R., Allegretti, I., Apoloner, M.-T., Aubert, C., Besançon, S., de Berc, M. B., Brunel, D., Capello, M., Čarman, M., Cavaliere, A., Chèze, J., Chiarabba, C., Cougoulat, G., Cristiano, L., Czifra, T., D'Alema, E., Danesi, S., Daniel, R., Dannowski, A., Dasović, I., Deschamps, A., Egendorf, S., Fiket, T., Fischer, K., Funke, S., Govoni, A., Gröschl, G., Heimers, S., Heit, B., Herak, D., Huber, J., Jarić, D., Jedlička, P., Jund, H., Klingen, S., Klotz, B., Kolínský, P., Kotek, J., Kühne, L., Kuk, K., Lange, D., Loos, J., Lovati, S., Malengros, D., Maron, C., Martin, X., Massa, M., Mazzarini, F., Métral, L., Moretti, M., Munzarová, H., Nardi, A., Pahor, J., Péquegnat, C., Petersen, F., Piccinini, D., Pondrelli, S., Prevolnik, S., Racine, R., Régnier, M., Reiss, M., Salimbeni, S., Santulin, M., Scherer, W., Schippkus, S., Schulte-Kortnack, D., Solarino, S., Spieker, K., Stipčević, J., Strollo, A., Süle, B., Szanyi, G., Szűcs, E., Thorwart, M., Ueding, S., Vallocchia, M., Vecsey, L., Voigt, R., Weidle, C., Weyland, G., Wiemer, S., Wolf, F., Wolyniec, D., & Zieke, T., 2018a. The AlpArray Seismic Network: A Large-Scale European Experiment to Image the Alpine Orogen, *Surveys in Geophysics*, **39**(5), 1–25.
- Hetényi, G., Plomerová, J., Bianchi, I., Exnerová, H. K., Bokelmann, G., Handy, M. R., Babuška, V., & Group, A.-E. W., 2018b. From mountain summits to roots: Crustal structure of the Eastern Alps and Bohemian Massif along longitude 13.3E, *Tectonophysics*, **744**, 239–255.
- Hintersberger, E., Decker, K., Lomax, J., & Lüthgens, C., 2018. Implications from palaeoseismological investigations at the Markgrafneusiedl Fault (Vienna Basin, Austria) for seismic hazard assessment, *NHESS*, **18**(2), 531–553.
- Hölzel, M., Decker, K., Zámolyi, A., Strauss, P., & Wagreich, M., 2010. Lower Miocene structural evolution of the central Vienna Basin (Austria), *Marine and Petroleum Geology*, **27**(3), 666–681.
- Hrubcová, P. & Šroda, P., 2015. Complex local Moho topography in the Western Carpathians: Indication of the ALCAPA and the European Plate contact, *Tectonophysics*, **638**(C), 63–81.
- Hrubcová, P., Šroda, P., Špičák, A., Guterch, A., Grad, M., Keller, G. R., Brueckl, E., & Thybo, H., 2005. Crustal and uppermost mantle structure of the Bohemian Massif based on CELEBRATION 2000 data, *Journal of Geophysical Research: Solid Earth*, **110**(B11), 292–21.
- Hua, Y., Zhao, D., & Xu, Y., 2017. Pwave anisotropic tomography of the Alps, *Journal of Geophysical Research: Solid Earth*, **122**(6), 4509–4528.
- Hungarian National Seismological Network, 1992. Kövesligethy Radó Seismological Observatory, Deutsches GeoForschungsZentrum GFZ, doi:10.14470/uh028726.
- Jaxybulatov, K., Shapiro, N. M., Koulakov, I., Mordret, A., Landès, M., & Sens-Schönfelder, C., 2014. A large magmatic sill complex beneath the Toba caldera, *Science*, **346**(6209), 617–619.
- Jolivet, L., Faccenna, C., Goffé, B., Burov, E., & Agard, P., 2003. SUBDUCTION TECTONICS AND EXHUMATION OF HIGH-PRESSURE METAMORPHIC ROCKS IN THE MEDITERRANEAN OROGEN , *American Journal of Science*, **303**, 353–409.

- Juretzek, C. & Hadzioannou, C., 2016. Where do ocean microseisms come from? A study of Love-to-Rayleigh wave ratios, *Journal of Geophysical Research: Solid Earth*, **121**(9), 6741–6756.
- Kalmár, D., Süle, B., & Bondár, I., 2018. Preliminary Moho depth determination from receiver function analysis using AlpArray stations in Hungary, *Acta Geodaetica et Geophysica*, **53**(2), 309–321.
- Kästle, E. D., El-Sharkawy, A., Boschi, L., Meier, T., Rosenberg, C., Bellahsen, N., Cristiano, L., & Weidle, C., 2018. Surface Wave Tomography of the Alps Using Ambient-Noise and Earthquake Phase Velocity Measurements, *Journal of Geophysical Research: Solid Earth*, **123**(2), 1770–1792.
- Kennet, B. L. N., 1991. IASPEI 1991 SEISMOLOGICAL TABLES, *Terra Nova*, **3**(2), 122–122.
- Kern, H., 1990. Laboratory seismic measurements: an aid in the interpretation of seismic field data, *Terra Nova*, **2**(6), 617–628.
- Kissling, E., 1988. Geotomography with local earthquake data, *Reviews of Geophysics*, **26**(4), 659–698.
- Kolínský, P., Bokelmann, G., & the AlpArray Working Group, 2019. Arrival angles of teleseismic fundamental mode Rayleigh waves across the AlpArray, *Geophysical Journal International*, **218**(1), 115–144.
- Krischer, L., Megies, T., Barsch, R., Beyreuther, M., Lecocq, T., Caudron, C., & Wassermann, J., 2015. ObsPy: a bridge for seismology into the scientific Python ecosystem, *Computational Science & Discovery*, **8**(014003).
- Lee, E. Y. & Wagreich, M., 2016. Polyphase tectonic subsidence evolution of the Vienna Basin inferred from quantitative subsidence analysis of the northern and central parts, *International Journal of Earth Sciences*, **106**(2), 687–705.
- Lentas, K., Di Giacomo, D., Harris, J., & Storchak, D. A., 2019. The ISC Bulletin as a comprehensive source of earthquake source mechanisms , *Earth System Science Data*, **11**, 565–578.
- Lin, F. C., Ritzwoller, M. H., & Snieder, R., 2009. Eikonal tomography: surface wave tomography by phase front tracking across a regional broad-band seismic array, *Geophysical Journal International*, **177**(3), 1091–1110.
- Lin, F. C., Tsai, V. C., & Ritzwoller, M. H., 2012. The local amplification of surface waves: A new observable to constrain elastic velocities, density, and anelastic attenuation, *Journal of Geophysical Research: Solid Earth*, **117**(B6), n/a–n/a.
- Lin, F. C., Li, D., Clayton, R. W., & Hollis, D., 2013. High-resolution 3D shallow crustal structure in Long Beach, California: Application of ambient noise tomography on a dense seismic array, *GEOPHYSICS*, **78**(4), Q45–Q56.
- Lippitsch, R., Kissling, E., & Ansorge, J., 2003. Upper mantle structure beneath the Alpine orogen from high-resolution teleseismic tomography, *Journal of Geophysical Research*, **108**(B8), 2376–15.

- Lomax, A., Virieux, J., Volant, P., & Berge-Thierry, C., 2000. Probabilistic Earthquake Location in 3D and Layered Models, in *Advances in Seismic Event Location. Modern Approaches in Geophysics*, vol. 18, eds Thurber, C. & Rabinowitz, N., Springer, Dordrecht.
- Longuet-Higgins, M. S., 1950. A theory of the origin of microseisms, *Philosophical Transactions of the Royal Society of London A Mathematical, Physical and Engineering Sciences*, **243**(857), 1–35.
- Lu, Y., Stehly, L., Paul, A., & AlpArray Working Group, 2018. High-resolution surface wave tomography of the European crust and uppermost mantle from ambient seismic noise, *Geophysical Journal International*, **214**(2), 1136–1150.
- Malusà, M. G., Faccenna, C., Baldwin, S. L., Fitzgerald, P. G., Rossetti, F., Balestrieri, M. L., Danišík, M., Ellero, A., Ottria, G., & Piromallo, C., 2015. Contrasting styles of (U)HP rock exhumation along the Cenozoic Adria-Europe plate boundary (Western Alps, Calabria, Corsica), *Geochemistry, Geophysics, Geosystems*, **16**(6), 1786–1824.
- Malzer, O., RÖGL, F., Seifert, P., Wagner, L., Wessely, G., & Brix, F., 1993. Die Molasse- zone und deren Untergrund, in *Erdöl und Erdgas in Österreich*, eds Brix, F. & Schultz, O., Verlag Naturhistorisches Museum Wien und F. Berger, Horn.
- Marsch, F., Wessely, G., & Sackmaier, W., 1990. Borehole breakouts as geological indications of crustal tension in the Vienna Basin, in *Mechanics of Joined and Faulted Rock*, pp. 113–120, ed. Rossmanith, P., Rotterdam.
- Mendoza, C. & Hartzell, S., 1988. Aftershock patterns and main shock faulting, *Bulletin of the Seismological Society of America*, **78**(4), 1438–1449.
- Meurers, B. & Ruess, D., 2009. A new Bouguer gravity map of Austria, *Austrian Journal of Earth Sciences*, **102**(1), 62–70.
- Mitterbauer, U., Behm, M., Brückl, E., Lippitsch, R., Guterch, A., Keller, G. R., Koslovskaya, E., Rumpfhuber, E.-M., & Šumanovac, F., 2011. Shape and origin of the East-Alpine slab constrained by the ALPASS teleseismic model, *Tectonophysics*, **510**(1-2), 195–206.
- Molinari, I. & Morelli, A., 2011. EPcrust: a reference crustal model for the European Plate, *Geophysical Journal International*, **185**(1), 352–364.
- Molinari, I., Verbeke, J., Boschi, L., Kissling, E., & Morelli, A., 2015. Italian and Alpine three-dimensional crustal structure imaged by ambient-noise surface-wave dispersion, *Geochemistry, Geophysics, Geosystems*, **16**(12), 4405–4421.
- Mordret, A., Landès, M., Shapiro, N. M., Singh, S. C., Roux, P., & Barkved, O. I., 2013a. Near-surface study at the Valhall oil field from ambient noise surface wave tomography, *Geophysical Journal International*, **193**(3), 1627–1643.
- Mordret, A., Shapiro, N. M., Singh, S., Roux, P., Montagner, J.-P., & Barkved, O. I., 2013b. Azimuthal anisotropy at Valhall: The Helmholtz equation approach, *Geophysical Research Letters*, **40**(11), 2636–2641.

- Mordret, A. D. R. M. L. e. & Shapiro, N. M., 2015. 3-D shear-velocity anisotropic model of Piton de la Fournaise volcano (La Réunion Island) from ambient seismic noise, pp. 1–22.
- Nakata, N., Boué, P., Brenguier, F., Roux, P., Ferrazzini, V., & Campillo, M., 2016. Body and surface wave reconstruction from seismic noise correlations between arrays at Piton de la Fournaise volcano, *Geophysical Research Letters*, **43**(3), 1047–1054.
- eds Nakata, N., Gaultier, L., & Fichtner, A., 2019. *Seismic Ambient Noise*, Cambridge University Press, Cambridge.
- National Network of Seismic Stations of Slovakia, 2004. ESI SAS, Deutsches GeoForschungsZentrum GFZ, doi:10.14470/uh028726.
- Nishida, K., Montagner, J. P., & Kawakatsu, H., 2009. Global Surface Wave Tomography Using Seismic Hum, *Science*, **326**(5949), 112–112.
- Nur, A., 1971. Effects of stress on velocity anisotropy in rocks with cracks, *Journal of Geophysical Research*, **76**(8), 2022–2034.
- Nur, A. & Simmons, G., 1969. Stress-induced velocity anisotropy in rock: An experimental study, *Journal of Geophysical Research*, **74**(27), 6667–6674.
- Omori, F., 1894. On the Aftershocks of Earthquakes, *Journal of the College of Science, Imperial University of Tokyo*, **7**, 111–120.
- Paul, A., Cattaneo, M., Thouvenot, F., Spallarossa, D., Béthoux, N., & Fréchet, J., 2001. A three-dimensional crustal velocity model of the southwestern Alps from local earthquake tomography, *Journal of Geophysical Research: Solid Earth*, **106**(B9), 19367–19389.
- Pedersen, H. A., 2017. Body waves from noise correlations: spurious arrivals from the north Pacific Ocean, in *EGU General Assembly*.
- Peresson, H. & Decker, K., 1997. The Tertiary dynamics of the northern Eastern Alps (Austria): changing palaeostresses in a collisional plate boundary, *Tectonophysics*, **272**(2-4), 125–157.
- Pfiffner, O. A., 2014. *Geology of the Alps*, Wiley Blackwell.
- Podvin, P. & Lecomte, I., 1991. Finite difference computation of traveltimes in very contrasted velocity models: a massively parallel approach and its associated tools, *Geophysical Journal International*, **105**(1), 271–284.
- Poli, P., Pedersen, H. A., Campillo, M., & the POLENET/LAPNET Working Group, 2011. Emergence of body waves from cross-correlation of short period seismic noise, *Geophysical Journal International*, **188**(2), 549–558.
- Prejean, S., Ellsworth, W., Zoback, M., & Waldhauser, F., 2002. Fault structure and kinematics of the Long Valley Caldera region, California, revealed by high-accuracy earthquake hypocenters and focal mechanism stress inversions, *Journal of Geophysical Research: Solid Earth*, **107**(B12), ESE 9–1–ESE 9–19.
- Qorbani, E. C., 2015. *Upper Mantle Anisotropy Under the Eastern Alps and the Pannonian basin*, Ph.D. thesis, Vienna.

- Ratschbacher, L., Frisch, W., Linzer, H.-G., & Merle, O., 1991a. Lateral extrusion in the eastern Alps, Part 2: Structure Analysis, *Tectonics*, **10**(2), 257–271.
- Ratschbacher, L., Merle, O., Davy, P., & Cobbold, P., 1991b. Lateral extrusion in the eastern Alps, Part 1: Boundary conditions and experiments scaled for gravity, *Tectonics*, **10**(2), 245–256.
- Reinecker, J. & Lenhardt, W. A., 1999. Present-day stress field and deformation in eastern Austria, *International Journal of Earth Sciences*, **88**(3), 532–550.
- Reinecker, J., Tingay, M., Müller, B., & Heidbach, O., 2010. Present-day stress orientation in the Molasse Basin, *Tectonophysics*, **482**(1-4), 129–138.
- Ren, Y., Stuart, G. W., Houseman, G. A., Dando, B., Ionescu, C., Hegedüs, E., Radovanović, S., & Shen, Y., 2012. Upper mantle structures beneath the Carpathian–Pannonian region: Implications for the geodynamics of continental collision, *Earth and Planetary Science Letters*, **349-350**, 139–152.
- Ren, Y., Grecu, B., Stuart, G., Houseman, G., Hegedüs, E., & South Carpathian Project Working Group, 2013. Crustal structure of the Carpathian-Pannonian region from ambient noise tomography, *Geophysical Journal International*, **195**(2), 1351–1369.
- Roux, P., Kuperman, W. A., & the NPAL Group, 2004. Extracting coherent wave fronts from acoustic ambient noise in the ocean, *The Journal of the Acoustical Society of America*, **116**(4), 1995–2003.
- Roux, P., Sabra, K. G., Kuperman, W. A., & Roux, A., 2005. Ambient noise cross correlation in free space: theoretical approach., *The Journal of the Acoustical Society of America*, **117**(1), 79–84.
- Roux, P., Moreau, L., Lecointre, A., Hillers, G., Campillo, M., Ben-Zion, Y., Zigone, D., & Vernon, F., 2016. A methodological approach towards high-resolution surface wave imaging of the San Jacinto Fault Zone using ambient-noise recordings at a spatially dense array, *Geophysical Journal International*, **206**(2), 980–992.
- Royden, L. H., 1985. The Vienna Basin: A Thin-Skinned Pull-Apart Basin, *Strike-Slip Deformation, Basin Formation, and Sedimentation*, **37**, 0.
- Rubin, A. M., Gillard, D., & Got, J.-L., 1999. Streaks of microearthquakes along creeping faults, *Nature*, **400**(6745), 635–641.
- Saint Louis University, 2016. Moment Tensor Solution for the 25.04.2016 Alland earthquake , Tech. rep.
- Schaff, D. P., Bokelmann, G. H. R., Beroza, G. C., Waldhauser, F., & Ellsworth, W. L., 2002. High-resolution image of Calaveras Fault seismicity, *Journal of Geophysical Research: Solid Earth*, **107**(B9), ESE 5–1–ESE 5–16.
- Schippkus, S., Zigone, D., Bokelmann, G., & the AlpArray Working Group, 2018. Ambient-noise tomography of the wider Vienna Basin region, *Geophysical Journal International*, **215**(1), 102–117.
- Schmid, S. M., F genschuh, B., Kissling, E., & Schuster, R., 2004. Tectonic map and overall architecture of the Alpine orogen, *Eclogae Geologicae Helvetiae*, **97**(1), 93–117.

- Schneider, F. M., Fuchs, F., Kolínský, P., Caffagni, E., Serafin, S., Dorninger, M., Bokelmann, G., & Group, A. W., 2018. Seismo-acoustic signals of the Baumgarten (Austria) gas explosion detected by the AlpArray seismic network, *Earth and Planetary Science Letters*, **502**, 104–114.
- Seats, K. J., Lawrence, J. F., & Prieto, G. A., 2011. Improved ambient noise correlation functions using Welch's method, *Geophysical Journal International*, **188**(2), 513–523.
- Seismic Network of the Republic of Slovenia, 2004. Slovenian Environment Agency, 10.7914/SN/SL.
- Shapiro, N. M. & Campillo, M., 2004. Emergence of broadband Rayleigh waves from correlations of the ambient seismic noise, *Geophysical Research Letters*, **31**(7).
- Shapiro, N. M., Campillo, M., Stehly, L., & Ritzwoller, M. H., 2005. High-resolution surface-wave tomography from ambient seismic noise., *Science*, **307**(5715), 1615–1618.
- Shearer, P. M., 2009. *Introduction to Seismology*, Cambridge University Press, Cambridge, 2nd edn.
- Smith, M. L. & Dahlen, F. A., 1973. The azimuthal dependence of Love and Rayleigh wave propagation in a slightly anisotropic medium, *Journal of Geophysical Research*, **78**(17), 3321–3333.
- Spica, Z., Perton, M., Calò, M., Legrand, D., Córdoba-Montiel, F., & Iglesias, A., 2016. 3-D shear wave velocity model of Mexico and South US: bridging seismic networks with ambient noise cross-correlations (C1) and correlation of coda of correlations (C3), *Geophysical Journal International*, **206**(3), 1795–1813.
- Stehly, L., Campillo, M., & Shapiro, N. M., 2006. A study of the seismic noise from its long-range correlation properties, *Journal of Geophysical Research*, **111**(B10), B10306.
- Stehly, L., Campillo, M., Froment, B., & Weaver, R. L., 2008. Reconstructing Green's function by correlation of the coda of the correlation (C3) of ambient seismic noise, *Journal of Geophysical Research*, **113**(B11).
- Stehly, L., Fry, B., Campillo, M., Shapiro, N. M., Guilbert, J., Boschi, L., & Giardini, D., 2009. Tomography of the Alpine region from observations of seismic ambient noise, *Geophysical Journal International*, **178**(1), 338–350.
- Stein, S. & Wysession, M., 2003. *An Introduction to Seismology, Earthquakes and Earth Structure*, Blackwell Publishing.
- Strasser, M., Anselmetti, F. S., Fäh, D., Giardini, D., & Schnellmann, M., 2006. Magnitudes and source areas of large prehistoric northern Alpine earthquakes revealed by slope failures in lakes, *Geology*, **34**(12), 1005–1008.
- Suess, E., 1901. *Das Antlitz der Erde*, William Johnson Sollas.
- Sun, W., Zhao, L., Malusà, M. G., Guillot, S., & Fu, L.-Y., 2019. 3-D Pn tomography reveals continental subduction at the boundaries of the Adriatic microplate in the absence of a precursor oceanic slab, *Earth and Planetary Science Letters*, **510**, 131–141.

- Taylor, G., Rost, S., Houseman, G. A., & Hillers, G., 2019. Near-surface structure of the North Anatolian Fault zone from Rayleigh and Love wave tomography using ambient seismic noise, *Solid Earth*, **10**(2), 363–378.
- Tesauro, M., Kaban, M. K., & Cloetingh, S. A. P. L., 2008. EuCRUST-07: A new reference model for the European crust, *Geophysical Research Letters*, **35**(5), 245–5.
- Tomek, v. & Hall, J., 1993. Subducted continental margin imaged in the carpathians of czechoslovakia, *Geology*, **21**(6), 535.
- Tsai, V. C., 2009. On establishing the accuracy of noise tomography travel-time measurements in a realistic medium, *Geophysical Journal International*, **178**(3), 1555–1564.
- Tsai, V. C., 2011. Understanding the amplitudes of noise correlation measurements, *Journal of Geophysical Research*, **116**(B9), B09311–16.
- Verbeke, J., Boschi, L., Stehly, L., Kissling, E., & Michelini, A., 2012. High-resolution Rayleigh-wave velocity maps of central Europe from a dense ambient-noise data set, *Geophysical Journal International*, **188**(3), 1173–1187.
- Wagner, M., Kissling, E., & Husen, S., 2012. Combining controlled-source seismology and local earthquake tomography to derive a 3-D crustal model of the western Alpine region, *Geophysical Journal International*, **191**(2), 789–802.
- Waldhauser, F., 2001. hypoDD – A Program to Compute Double-Difference Hypocenter Locations, Tech. rep., USGS.
- Waldhauser, F. & Ellsworth, W. L., 2000. A Double-difference Earthquake location algorithm: Method and application to the Northern Hayward Fault, California, *Bulletin of the Seismological Society of America*, **90**(6), 1353–1368.
- Waldhauser, F. & Schaff, D. P., 2008. Large-scale relocation of two decades of Northern California seismicity using cross-correlation and double-difference methods, *Journal of Geophysical Research: Solid Earth*, **113**(B8), 501–15.
- Wessely, G., 2000. Sedimente des Wiener Beckens und seiner alpinen und subalpinen Unterlagerung - Exkursionsführer Sediment 2000, *Mitteilungen der Gesellschaft der Geologie- und Bergbaustudenten in Wien*, **44**, 191–214.
- Wessely, G., 2006. *Geologie der Österreichischen Bundesländer: Niederösterreich*, Geologische Bundesanstalt, Wien.
- Wölfler, A., Kurz, W., Fritz, H., & Stüwe, K., 2011. Lateral extrusion in the Eastern Alps revisited: Refining the model by thermochronological, sedimentary, and seismic data, *Tectonics*, **30**(4).
- Yang, Y. & Ritzwoller, M. H., 2008. Characteristics of ambient seismic noise as a source for surface wave tomography, *Geochemistry, Geophysics, Geosystems*, **9**(2).
- Yang, Y., Ritzwoller, M. H., Levshin, A. L., & Shapiro, N. M., 2007. Ambient noise Rayleigh wave tomography across Europe, *Geophysical Journal International*, **168**(1), 259–274.

- Zedník, J. & Pazdírková, J., 2010. Seismic activity in the Czech Republic in 2008, *Studia Geophysica et Geodaetica*, **54**(2), 333–338.
- Zhao, L.-S. & Helmberger, D. V., 1994. Source Estimation from Broadband Regional Seismograms, *Bulletin of the Seismological Society of America*, **84**(1), 91–104.
- Zhu, L. & Helmberger, D. V., 1996. Advancement in source estimation techniques using broadband regional seismograms, *Bulletin of the Seismological Society of America*, **86**(5), 1634–1641.
- Zigone, D., Ben-Zion, Y., Campillo, M., & Roux, P., 2015. Seismic Tomography of the Southern California Plate Boundary Region from Noise-Based Rayleigh and Love Waves, *Pure and Applied Geophysics*, **172**(5), 1007–1032.
- Zinke, J. C. & Zoback, M. D., 2000. Structure-Related and Stress-Induced Shear-Wave Velocity Anisotropy: Observations from Microearthquakes near the Calaveras Fault in Central California, *Bulletin of the Seismological Society of America*, **90**(5), 1305–1312.
- Zoback, M. D., 2010. *Reservoir Geomechanics*, Cambridge University Press.